

MAGNETOQUASISTATIC SENSORS FOR RAPID IMAGING OF STEEL
PIPELINE PROPERTIES

BY

SCOTT A. DENENBERG

DISSERTATION

Submitted in partial fulfillment of the requirements
for the degree of Doctor of Philosophy in Electrical and Computer Engineering
in the Graduate College of the
University of Illinois at Urbana-Champaign, 2014

Urbana, Illinois

Doctoral Committee:

Professor Andreas Cangelaris, Chair
Professor Jennifer Bernhard
Professor Jianming Jin
Professor Farzad Kamalabadi

ABSTRACT

The purpose of this research effort is to advance the capabilities of existing model-based spatially periodic magnetoquasistatic-field sensors in order to provide a solution for imaging the metallic properties of pipelines. The target problem addressed is rapidly imaging pipeline steel thickness through thick insulation and weatherjacketing materials in order to detect areas of corrosion. The following bullet points outline the advancements in sensor design, sensor electronics and electromagnetic models necessary to develop a corrosion under insulation (CUI) inspection tool.

1. *Development of sensor and sensor electronics with sufficient sensitivity for steel thickness imaging.* A fundamental problem with rapidly imaging steel thickness through thick coatings is achieving a sufficient signal to noise ratio (SNR). SNR is a function of sensor design and sensor electronics. Many possible sensing approaches are evaluated theoretically, leading to the development of magnetoresistive sense elements in a quasi-periodic drive structure.
2. *Development and validation of cylindrical geometry models for inductive sensors.* The existing models for inductive spatially periodic magnetoquasistatic-field sensors assume a planar layered medium geometry. Work has been done to extend this to a circularly symmetric planar layered medium, but the problem of a cylindrically layered medium, as seen in pipelines, has not been approached. Validation will show the needed improvement in agreement between the models and measurements taken with magnetoresistive sensors wrapped around cylindrical specimens. Models are developed and implemented for low-frequency

applications, such as the detection of steel thickness, for sensors with the main drive legs aligned circumferentially around the pipe as well as for sensors with the main drive legs aligned axially.

3. *Modeling of sensor interaction with local material deviations.* The models developed for magnetoquasistatic-field sensors assume a uniformly layered medium. This assumption breaks down in the presence of local defects such as corrosion pitting and weatherjacket overlaps. A model is developed to better understand the footprint of the sensor as the magnetic fields diffuse through material layers. This model provides insight leading to a more effective design of magnetoquasistatic-field sensors with reduced unmodeled effects and increased scanning resolution.
4. *Model-based correction for flawed regions to improve flaw sizing.* For flaws smaller than the sensor footprint and for flaws with sharp edges, there is a deviation from the uniform-layered medium model. The same footprint model used to design a sensor with enhanced resolution can be further used to provide a more accurate assessment of flaw depth.

This dissertation details the research completed in the process of designing a CUI inspection tool. The methodology used has proved successful in meeting the target requirements.

To my family, for their love and support.

To JENTEK and my coworkers, for their assistance and patience.

ACKNOWLEDGMENTS

This research effort was sponsored by JENTEK Sensors, Inc. I would like to thank Dr. Neil Goldfine, president of JENTEK, for believing in me enough to provide financial sponsorship through my graduate studies. Dr. Goldfine was there to provide encouragement and helpful suggestions during every stage of the research. Without his guidance, none of this work would have been possible.

I would like to thank my advisor, Professor Andreas Cangellaris, for his encouragement, guidance and technical direction during the thesis process. I would also like to thank the other members of my thesis committee, Professor Jennifer Bernhard, Professor Jianming Jin and Professor Farzad Kamalabadi, for helpful suggestions and insightful comments during the preliminary and final examinations.

Thanks also to the many members of the JENTEK team who helped answer questions, gather information and take measurements during this project. Special thanks to Dr. Yanko Sheiretov for always being there to help, no matter the hour, to Paula Gentile for her graphic design expertise, and to Todd Dunford for his mechanical design support.

Special thanks go to my family and friends for their support through this long process. Thank you to my mom and dad for encouraging me, serving as role models, and helping to edit this dissertation. And finally, thank you to the Illinois tennis family for taking me in and making the University of Illinois feel like home from the moment I stepped on campus.

TABLE OF CONTENTS

CHAPTER 1	INTRODUCTION	1
1.1	Significance of the Opportunity: Corrosion Under Insulation (CUI)	2
1.2	State of the Art in CUI Inspection Technologies	5
1.3	The Meandering Winding Magnetometer	9
1.4	MWM-Arrays	11
1.5	Grid Methods	11
1.6	Research Goals	14
CHAPTER 2	SENSOR AND SENSOR ELECTRONICS DESIGN	17
2.1	Determining the Frequency of Excitation	17
2.2	Noise Analysis for JENTEK Instrumentation	22
2.3	Sensor Design Analysis	23
2.4	Feedback Configuration for the Magneto-resistive Sense Element	34
2.5	Prototype Magneto-resistive MWM-Array	38
CHAPTER 3	MODELING OF THE MWM IN CYLINDRICAL COORDINATES	42
3.1	Motivation for the Cylindrical MWM Model	43
3.2	MWM Forward Model in Cylindrical Coordinates: Drive Aligned with ϕ -Axis	45
3.3	MWM Forward Model in Cylindrical Coordinates: Drive Aligned with z -Axis	62
CHAPTER 4	SENSOR FOOTPRINT ANALYSIS	75
4.1	1-D Perfect Electrical Conductor (PEC) Footprint Model	78
4.2	2-D PEC Footprint Model	82
4.3	Cylindrical Coordinate Footprint Model Incorporating Diffusion Effects	85
4.4	Sensor Design Optimization	87
CHAPTER 5	FLAW SIZING	93
5.1	Proposed Lattice Approach for Flaw Sizing	93
5.2	Lattice Generation and Orthogonality	95
5.3	Finite Element Method (FEM) and Measurement Validation of Sizing Approach	98

CHAPTER 6	SUMMARY, CONCLUSIONS AND SUGGESTED FUTURE	
	WORK	104
6.1	Summary and Conclusions	104
6.2	Suggested Future Work	106
REFERENCES	111

CHAPTER 1

INTRODUCTION

The goal of the research presented in this dissertation is to advance the capabilities of existing spatially-periodic magnetoquasistatic (MQS) sensors in order to provide a solution for imaging the metallic properties of pipelines. This type of sensor has found widespread use in the non-destructive evaluation (NDE) of materials because of its effectiveness in measuring the general electrical, magnetic and geometric properties of a material under test (MUT), such as electrical conductivity, magnetic permeability, layer thickness and proximity or lift-off [1]. A brief overview of the existing MQS sensor technology is provided in Section 1.3.

Until recently, MQS sensors have been used almost exclusively in the aerospace and defense industries for the detection of flaws such as cracks, voids, and inclusions in metal components of aircraft and other structures. In fact, eddy current sensors in general have had limited success in the oil and gas field as compared to competing techniques including ultrasound, radiography, and magnetic flux leakage (MFL) [2]. Typical limitations have included a lack of tolerance for large distances to the MUT, limited coverage area, slow scan speeds, and a lack of sensitivity to defects on the far side of a material. However, these issues are not fundamental limitations of the MQS method and have been overcome through this research effort while maintaining the method's strengths, which include non-contact operation, insensitivity to non-conductive materials (such as insulation and coatings), and the ability to measure multiple material properties simultaneously using a model-based method.

1.1 Significance of the Opportunity: Corrosion Under Insulation (CUI)

Pipelines that are used for oil, gas, and chemical transportation, or those that are part of a refinery or processing facility, may be covered by non-magnetic, non-conductive coating that can be over four inches thick. The purpose of these coatings may be to provide thermal insulation in the case of a large thermal gradient between the pipeline's contents and the surroundings, decrease pipeline buoyancy in the case of underwater pipelines, or protect the pipeline from mechanical damage. In addition, to protect the pipeline and the insulation from the weather, specifically moisture due to humidity and precipitation, aluminum or stainless steel weather protection (also called "weatherjacket") may be secured over the insulation and held in place by metal straps along the length of the pipe.

Figure 1.1 shows the cross-section of a typical pipeline geometry. The relative dimensions of the pipe insulation and weather protection are illustrated. Dimensions of interest include the pipe's outer diameter, inner diameter, wall thickness, insulation thickness and weatherjacket thickness. Actual pipelines may have a wide range of dimensions. For example, typical insulation thicknesses may range from 1 to 4", depending on the material being transported within the pipeline.

Over time, pipelines can corrode, reducing the integrity of the pipeline and increasing the risk of a catastrophic failure. For the purposes of this document, "corrosion-under-insulation" (CUI) will be used to refer to both internal and external corrosion; in the oil and gas industry, the term "CUI" is used to refer to external corrosion only.

CUI can result from a variety of mechanisms, the most common being exposure to moisture that penetrates the weatherjacketing and insulation. The mechanism of corrosion determines whether the corrosion is on the internal or external surface of the pipe and whether the corrosion will present itself as pitting, localized reduction in the wall thickness of the pipe or general wall loss over large areas. The factors

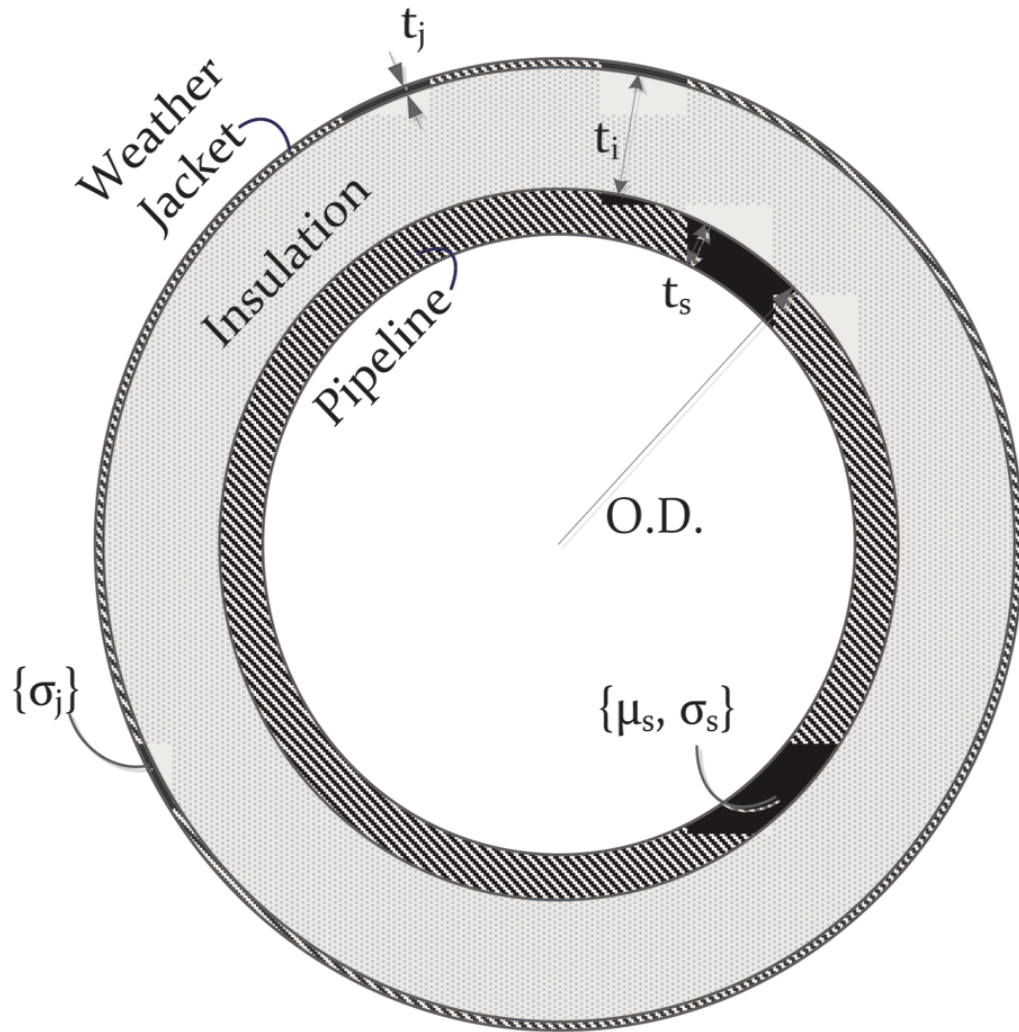


Figure 1.1: Cross-section of a typical pipeline geometry.

affecting CUI include, but are not limited to, the amount of moisture, availability of oxygen, metal surface temperature, type and design of insulation, and presence of deleterious contaminants, e.g., chlorides. CUI can be quite aggressive, with corrosion rates anywhere from 1mm/year (40 mils/year) to 8 mm/year (300+ mils/year) [3].

In fact, corrosion is one of the leading causes of failure in onshore transmission pipelines (both gas and hazardous liquids) in the United States. Over the years from 1988-2008, there was an average of 52 significant corrosion incidents per year. These significant incidents resulted in 30 fatalities, 100 injuries, and \$551 million in property damage [4]. These costs are compounded by the lost revenue due to the shutdowns caused by these failures. Factors that affect the likelihood of failure include pipeline age, construction materials, and operator practices in managing the integrity of its pipeline system. Therefore, as the pipeline infrastructure continues to age, inspection methods need to improve so that local replacement of pipe sections can be performed preemptively in order to avoid pipeline failure [5].

Inspection techniques can be grouped into two distinct categories: those that are performed from the interior of the pipeline and those that are performed from the exterior of the pipeline. Internal pipeline inspection is performed using a pipe inspection gauge (PIG) which is inserted into the pipe. As the PIG passes down the pipe, inspection data is recorded which can then be used to identify sections of the pipe requiring maintenance. Wall thickness measurements are made using inspection techniques such as magnetic flux leakage (MFL) and ultrasound and are supplemented by eddy current proximity measurements [6].

The use of the PIG is only appropriate when the pipeline is sufficiently large and the pipeline has been constructed with appropriate launching and receiving ports. This is often not practical, especially in refineries where there are thousands of short sections of pipe with multiple bends that are not well-suited for PIGs. In these cases it is necessary to perform the inspection from the exterior of the pipeline.

Conventional exterior inspection techniques require that the weather protection and insulation be removed from the pipe so that visual, ultrasonic, or another inspection method can be performed [6]. Since the insulation must be removed and then replaced, these inspections can be very time consuming and expensive. These costs are greatly increased if the pipeline is very hot and the removal of the insulation requires flow to be shut off.

Given the aging of the worldwide pipeline infrastructure and the available inspection techniques, there is a clear need for an exterior pipe inspection method that does not require the removal or subsequent replacement of the pipe’s insulation and weather jacket. Deep penetrating MQS arrays can fill that need. Magnetic field-based eddy current sensor arrays are seeing increasing interest as an inspection technique that can deliver reliable and low-cost solutions for high resolution imaging of damage in pipelines. Eddy current methods are insensitive to non-conducting insulation, and, with an effective model, a multiple frequency approach can provide correction for a conducting weatherjacket layer. Therefore, the MQS approach can allow for the insulation to be left in place during the inspection, greatly reducing inspection cost.

This research builds on JENTEKs Meandering Winding Magnetometer (MWM-Array[®]) eddy current technologies [1]. The developed MR-MWM-Array[®] technology uses eddy-current sensor arrays with magnetoresistive sense elements and model-based inverse methods (using precomputed databases called hyperlattices) to determine properties of a pipeline and its insulating materials.

1.2 State of the Art in CUI Inspection Technologies

There are a few established methods for scanning pipelines for corrosion through insulation and weatherjacketing. The advantages and disadvantages of these methodologies are discussed in the following sections. The industry opinion of each method

and specific implementations are summarized in the document “Evaluation of the effectiveness of non-destructive testing screening methods for in-service inspection,” which was prepared by the third-party Doosan Babcock Energy Limited for the Health and Safety Executive in 2009 [7].

1.2.1 Pulsed Eddy-Current

Pulsed eddy-current is an NDT inspection method that uses a square-wave drive excitation as opposed to the continuous-wave sinusoidal drive excitation of other standard-eddy current methods. One potential advantage of the square-wave drive excitation is that it allows for all of the odd-harmonics of the base frequency to be excited simultaneously as the Fourier series expansion of a square wave, $S(x)$, can be expressed as

$$S(x) = \frac{4}{\pi} \sum_{n=1,3,5,\dots}^{\infty} \frac{1}{n} \sin\left(\frac{n\pi x}{L}\right) \quad (1.1)$$

where L is the period of the square-wave excitation. More often than not (if not always), pulsed-eddy current technologies excite a single square wave pulse and then “listen” on the secondary for the response decay as seen in Figure 1.2.

As an overall method for CUI inspection, pulsed-eddy current is viewed as a very slow inspection method with point measurements taking from 2 to 10 seconds depending on which system is being used. Incotest, the RTD implementation of pulsed-eddy current for CUI inspection, advertises the ability to take 1000 measurements per day [8].

In addition to being a slow, non-scanning measurement approach, pulsed-eddy current uses a large secondary coil and therefore averages over a very large measurement footprint. As such, it is limited in its detection of local corrosion. A more detailed discussion of sensor footprints, especially as applied to the linear-array MQS sensors, will be the subject of Chapter 4.

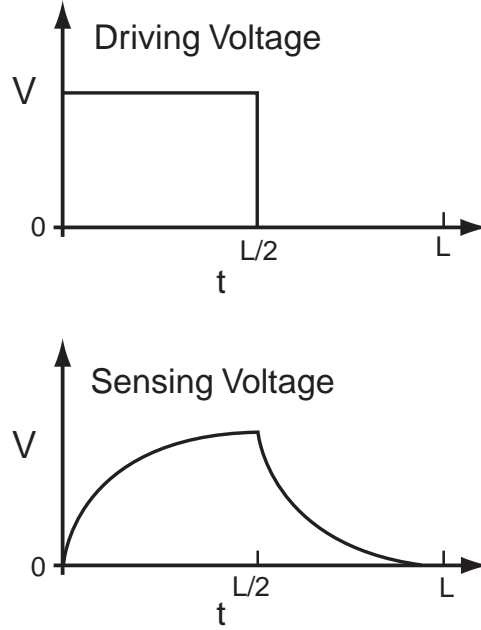


Figure 1.2: Excitation pulse and secondary decay response for a pulsed-eddy current sensor.

Finally, since the standard pulsed-eddy current practice uses a reference standard calibration, the thickness estimates are very sensitive to changes in insulation thickness, pipeline properties, and weatherjacket properties. The importance of correcting for these factors will be discussed in more detail in Chapter 3.

1.2.2 Guided-Wave Ultrasonics

Guided wave ultrasonic testing (GWUT), also commonly referred to long range ultrasonic testing (LRUT), is a pipeline inspection method that has garnered a lot of support in the last decade. GWUT uses an array of low-frequency ultrasonic transducers that are mounted around the circumference of the pipeline, such that the transducers are in direct contact with the pipeline metal. The transducers generate torsional, longitudinal and flexural waves that propagate down the pipe. The transducers are then switched from pulse mode to echo mode where they listen for reflections caused by changes in pipe cross-sectional area due to flanges, circum-

ferential welds, branches and defects in the wall [9].

There are many successful implementations of GWUT on the market including, but not limited to, the Wavemaker[®] G3 Pipe Screening System from Guided Ultrasonics Ltd [10] and the Teletest Focus[®] manufactured by Plant Integrity [11]. The general success of the GWUT is due to the fact that low-frequency guided waves propagate a long way in pipelines with relatively small losses. This is due to the low absorption factor of pipeline steel, the large acoustic impedance mismatch between pipeline steel and air, and the intelligent selection of wave-modes with a low dispersion coefficient [9].

There are significant drawbacks and limitations to GWUT, however. While their inspections can cover a long range, the systems are not well-suited for short sections of pipeline. There is an uninspectable area on the order of meters long around where the transducers are mounted. Furthermore, direct access to the pipeline is required for mounting of the transducers. Since the reflection signal is dependent on the change in cross-sectional area of the pipeline, it is limited in the detection of localized corrosion, and internal-external corrosion discrimination is not available. Teletest, for example, indicates that a 9% cross-sectional area change can be detected. This means that a 2" defect, regardless of depth, is undetectable on an 8" diameter pipeline [11].

1.2.3 Radiography

Radiography is a third alternative for CUI inspection which utilizes a single or linear array of solid state detectors to measure wall thickness based on the transmission of x-rays or gamma-rays. Two popular radiography methods are the SCAR[®] (Small Controlled Area Radiography) System developed by Oceaneering [12] and the ThruVu[®] System developed by Omega International Technology [13]. While effective at detecting both general and local corrosion through insulation in a scanning mode of almost 1 inch/second, all radiography approaches have the same drawback - the safety

concerns regarding radiation exposure to operators and the surrounding environment. These concerns are addressed by using lower-power radiation sources. However, this limits the thickness of inspectable steel and the measurement resolution. Also, as the radiation source and detector must be mounted on either side of the pipeline, access to the entire circumference of the pipe is necessary. This is often not practical.

1.3 The Meandering Winding Magnetometer

The Meandering Winding Magnetometer (MWM[®]) is an example of a spatially periodic MQS sensor that was developed at the Laboratory of Electromagnetics and Electronic Systems (LEES) at MIT. The MWM, originally called the Inter-Meander Magnetometer, was invented by Professor James R. Melcher. It is well-suited for property measurements of single-layer and multiple-layer magnetic and/or conducting media, making its sensor structure appropriate for tackling the CUI problem [1]. Potentially measured properties for each layer are conductivity, complex magnetic permeability, and thickness. The sensor structure of a standard MWM can be seen in Figure 1.3.

The MWM has magnetometer windings that are laid out in a planar, spatially periodic pattern such that the sensor has one-sided contact with the MUT. The imposed spatial period (wavelength) determines the frequency independent rate of decay of the fields away from the sensor and is chosen to achieve the desired depth of sensitivity. The periodic nature of the magnetic fields produced by the primary windings allows for the use of Fourier series methods in the semi-analytical models.

The MWM has several advantages over other standard eddy-current sensing technologies:

1. The simple sensor structure allows for semi-analytic models with excellent agreement between measured and simulated responses. This eliminates the need for

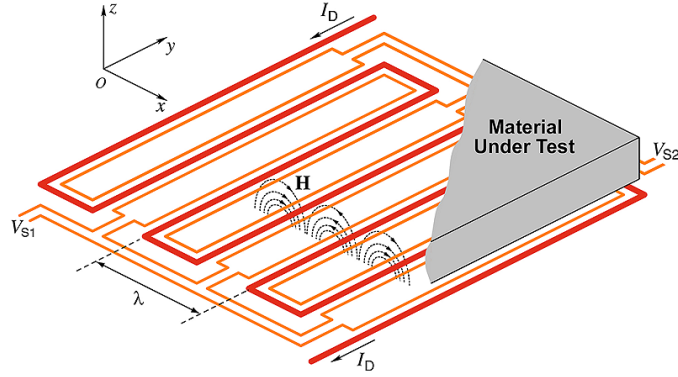


Figure 1.3: Sensor structure of a standard MWM. The drive current, I_D , in the primary winding (the bolder trace) generates a spatially periodic magnetic field \mathbf{H} . This magnetic field couples through the MUT and induces voltages (V_{S1} and V_{S2}) at the terminals of the secondary windings (the finer traces). These terminals are generally attached in series such that the total induced voltage is $V_S = V_{S1} + V_{S2}$. The measured complex transimpedance $Z_S = V_S/I_D$ is a function of the properties of the MUT and the sensor geometry.

complicated calibration standards and procedures: a calibration in air is often sufficient. The sensor models will be discussed in more detail in Chapter 3.

2. Control over the spatial period and frequency of excitation makes it possible to measure depth profiles of materials by combining information from multiple wavelengths and/or frequencies.
3. Sensor arrays can be created by placing elements in a row along a single drive winding. As long as the winding is sufficiently long there is good matching from one element to the next. Arrays will be discussed more in the following section.
4. The sensor substrate can be flexible allowing for measurement over curved surfaces, such as cylindrical pipelines.

After being conceived at MIT, the MWM was further developed at JENTEK and has been successfully applied to a variety of practical applications [14]-[31] including coating characterization, crack detection in metal components, measurement of stress in ferromagnetic materials, quality control for shotpeened and coldworked materials,

and early-stage fatigue monitoring.

1.4 MWM-Arrays

The MWM-Array was conceived to overcome some of the shortcomings of the MWM sensor. The MWM, seen in Figure 1.3, has excellent agreement with the semi-analytic models and therefore produces accurate and robust measurements. However, its large single-channel design is not useful for high-resolution imaging over large areas. For these applications, the MWM-Array was designed with multiple, smaller sense elements placed next to a linear and compact drive winding, as shown in Figure 1.4 [32, 33]. This simple, patented construct allows both deep penetration and relatively high-resolution imaging compared to other eddy current methods. Furthermore, as long as the drive winding extends significantly on either side of the edge sense elements, all of the sense elements will behave similarly and agree with the same model.

1.5 Grid Methods

The multiple frequency impedance response of an MWM and MWM-Array is converted into material properties of the MUT using measurement grids [34]. A measurement grid is a 2-dimensional database of sensor responses at a given frequency created by representing the MUT as a uniform-layered media model, as shown in Figure 1.5 for a sensor above a piece of steel. The semi-analytic forward model of the sensor, discussed more in Chapter 3, is used to generate the database of impedance responses for the sensors over the range of material properties of interest. A proprietary, non-linear search and interpolation algorithm uses the sensor response to determine the material properties of interest. Figure 1.6 shows a visual representation of a conductivity/lift-off grid with data from one channel of an MWM-Array overlaid. The data contains scans at four different insulating coating thicknesses which changes

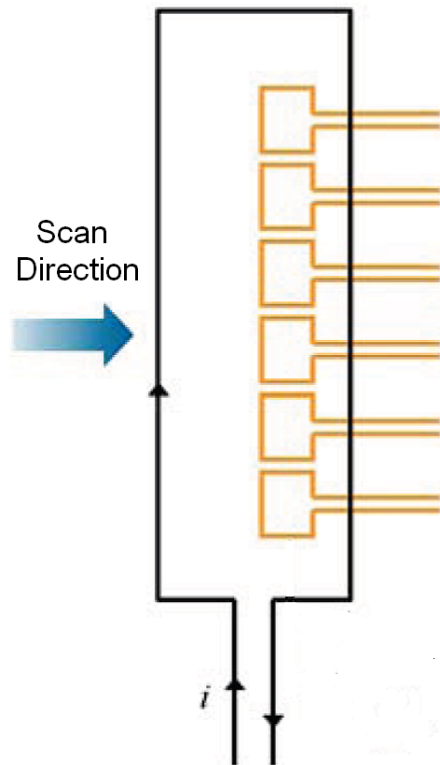


Figure 1.4: Schematic of an MWM-Array with a single linear drive winding and multiple sense elements.

the resulting lift-off. This figure illustrates how the conductivity and lift-off can be independently measured by comparing the sensor response to the database of pre-computed sensor responses [35].

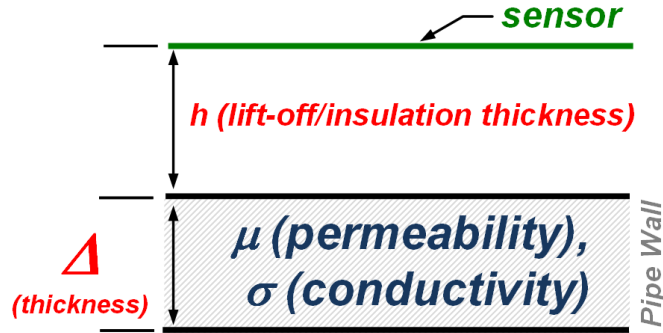


Figure 1.5: Simple layered media model for the inspection of a steel plate.

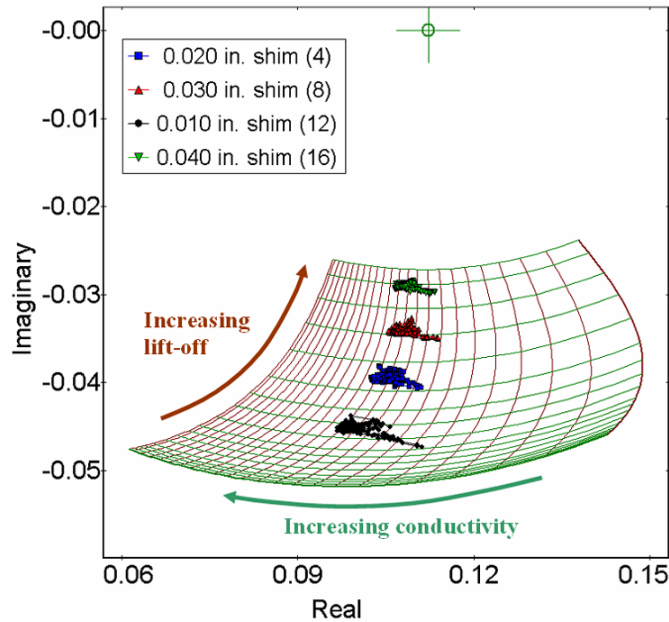


Figure 1.6: Representative conductivity/lift-off measurement grid with data from one channel of an MWM-Array. The data contains scans at four different insulating coating thicknesses which change the resulting lift-off.

When there are more than two unknown material properties, a higher-order dimensional database (called a lattice for 3 unknowns and a hyperlattice for 4 or more unknowns) is needed spanning more than one frequency. Each frequency provides two

degrees of freedom (the real and imaginary components of the impedance response). Therefore, for n frequencies, as many as $2n$ material properties can be estimated simultaneously. Figure 1.7 illustrates slices of a hyperlattice at a single frequency for measuring the thickness and permeability of a steel plate while accounting for a variable sensor liftoff.

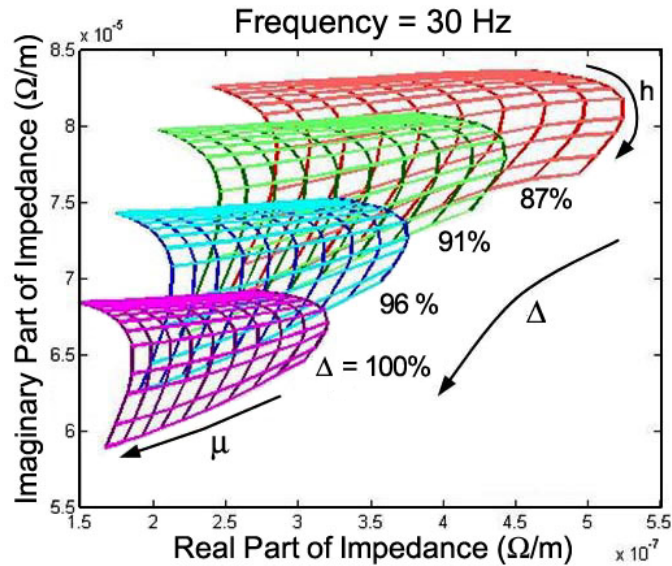


Figure 1.7: Representation of a 3-parameter lattice for the sensor lift-off, permeability of the steel plate and thickness of the steel plate.

1.6 Research Goals

The goal of this research effort is to develop an MWM-Array-based corrosion under insulation tool that satisfies current industry needs. These industry needs were established through discussions with potential customers of the proposed technology. This requires developing a sensor that can image through at least 0.5” of steel, covered in 2” of insulation and weatherjacket. In order to outperform any competitive method, a target flaw 0.05” deep over a 2” diameter area must be detected. As with other MWM applications, no reference standard should be required because a calibration in

air should be sufficient. General wall thickness estimates away from local deviations should be accurate within 0.005". The inspection must be in a scanning mode covering 1-2" of pipeline per second.

The objectives of this research effort can be summarized as follows.

1. Design of the sensor and sensor electronics to achieve required sensitivity.
 - (a) Establish sensitivity requirements through sensor models.
 - (b) Theoretically evaluate multiple sensor design concepts for feasibility.
 - (c) Build prototype sensor and sensor electronics to demonstrate achieved capability.
2. Develop sensor models to accurately describe sensor interaction with cylindrically layered media.
 - (a) Demonstrate that a model is required and that existing models are inadequate.
 - (b) Develop a model for an MWM sensor in cylindrical coordinates with the drive aligned circumferentially.
 - (c) Develop a model for an MWM sensor in cylindrical coordinates with the drive aligned axially.
 - (d) Demonstrate necessary accuracy of models to calibrate in air and measure pipeline properties.
3. Develop a model to describe sensor interaction with local perturbations.
 - (a) Demonstrate that different sensor geometries have very different sensitivities to local perturbations.
 - (b) Develop a model to describe these differences and to evaluate different sensor constructs.

(c) Build an improved sensor construct and demonstrate improved sensitivity.

4. Improve flaw sizing algorithms.

(a) Demonstrate the inadequacy of uniform layer estimates for local defects.

(b) Incorporate footprint models into property estimation.

(c) Take measurements on a set of representative pipelines with defects to demonstrate successful implementation.

CHAPTER 2

SENSOR AND SENSOR ELECTRONICS DESIGN

The first step to designing a successful MWM-based CUI inspection tool is to determine what combination of frequency excitation and noise level is required to achieve the necessary sensitivity to steel thickness. This chapter quantifies the signal-to-noise ratio (SNR) needed to match the established system requirements (see Section 1.6), identifies a sensor design that can meet the required benchmarks, and then presents preliminary measurements taken with a prototype sensor and sensor electronics that achieve the required sensitivity. For simplicity, only a flat plate material stack-up is considered in this chapter. The cylindrical coordinate geometry problem of measuring on a pipeline is approached in Chapter 3.

2.1 Determining the Frequency of Excitation

In order to achieve sensitivity through 0.5" of steel using a magnetic field sensor, a low frequency must be excited. Using the Cartesian-coordinate models developed and implemented in [36]-[38], measurement grids may be generated that quantify a sensor's sensitivity to material properties. Figure 2.1 shows grids at 5 Hz, 20 Hz and 80 Hz for varying lift-offs and thicknesses of a steel plate given typical electrical and magnetic properties of pipeline steel (a relative permeability of 80 and a conductivity of 5.7×10^6 S/m) for a sensor structure with a sufficiently large wavelength (this will be defined in the following discussion). All grids are normalized so that the "air point", the point in impedance space that represents the sensor's response in air, is at $(1+0j)$.

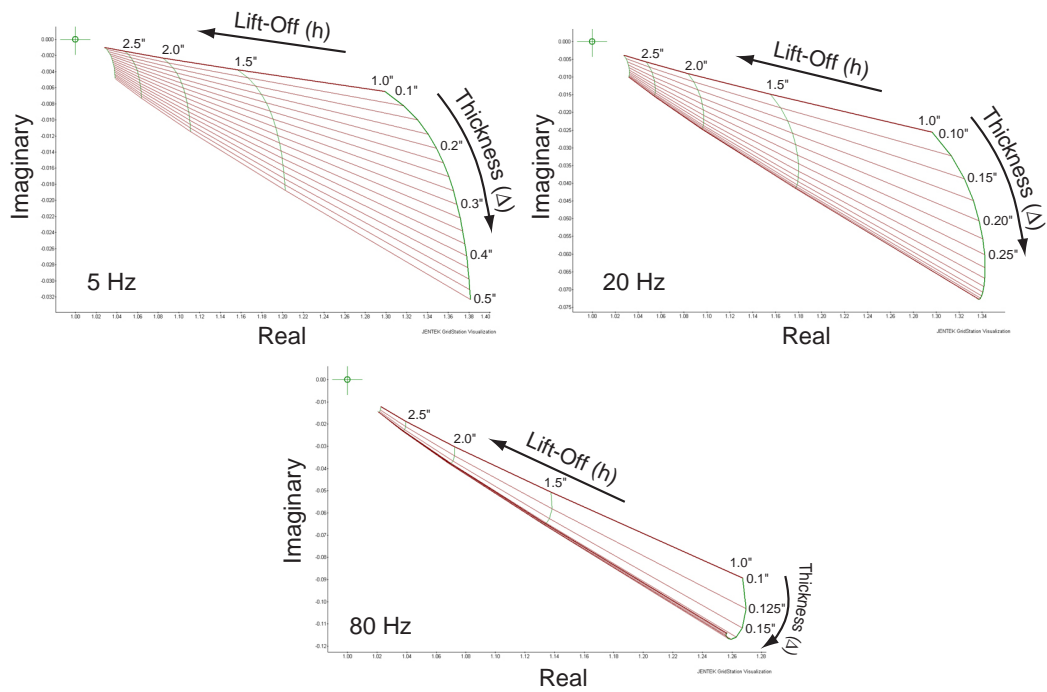


Figure 2.1: 5 Hz, 20 Hz and 80 Hz grids for varying lift-offs and thicknesses of a steel plate given typical steel properties (a relative permeability of 80 and a conductivity of $5.7e6$ S/m) for a sensor structure with a sufficiently large wavelength. All of the grids are normalized so that the “air point”, the point in impedance space that represents the sensor’s response in air, is at $(1 + 0j)$.

It is clear from these grids that varying the frequency has the effect of changing the sensor's response to steel thickness. This is due to two competing factors. First, as the frequency is lowered, an MWM's overall response to steel decreases because of $\frac{dB}{dt}$. This is demonstrated by the relative y-axis scales of Figure 2.1. Secondly, as you lower the frequency, the skin-depth of the sensor

$$\delta = \sqrt{\frac{2}{\omega\mu\sigma}} \quad (2.1)$$

increases, indicating more magnetic field penetration into the steel and, therefore, increased sensitivity to the steel thickness. In this equation ω is the angular excitation frequency in rad/sec, μ is the magnetic permeability of the MUT, and σ is the conductivity of the MUT. The skin-depth is defined as the distance into the material where the magnetic field intensity has dropped by a factor of $1/e$. This is only true, however, when the characteristic wavelength of the sensor is significantly larger than the distance away from the MUT, which is the case for these grids.

If our goal is to choose a frequency that maximizes sensitivity through 0.5" of steel at 2" of lift-off, we can plot the sensor's magnitude response to a change of thickness from 0.450" to 0.5" at different frequencies and see where the response is maximized. Figure 2.2 shows these results for a variety of conditions. For all conditions, it is clear that the lower the frequency of excitation, the higher the sensitivity through the steel. However, the benefits do decrease as the frequency is further reduced, eventually plateauing. On the left of Fig 2.2, we show that the shape of the sensitivity vs. frequency curve is independent of lift-off. In the center we show that the presence of the weatherjacket, while causing a very large shift in the nominal phase of the sensor's response, as seen in Figure 2.3, has very little impact on the sensitivity vs frequency curve. And on the right of Fig 2.2, as is obvious when looking at the skin depth formula, we see that as the $\mu\sigma$ product increases, it is necessary to go to lower

frequencies to cross the inflection point where reducing the frequency has reduced sensitivity benefit.

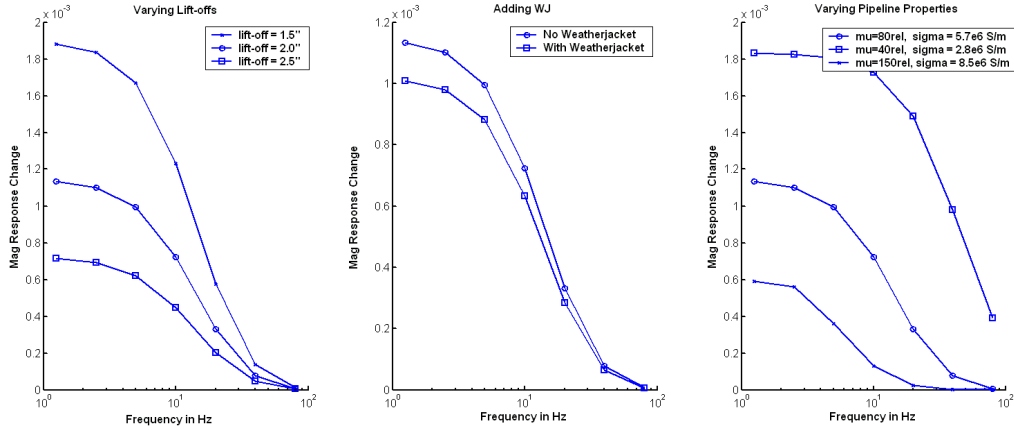


Figure 2.2: Plots summarizing the relationship between the frequency of excitation and the sensitivity through 0.5” of steel. The y-axis represents the magnitude of the change of the sensor response due to a change in steel thickness from 0.45” to 0.5”. On the left are curves for varying sensor lift-off. In the center are curves for the presence of and absence of the weatherjacket. On the right are curves for varying pipeline properties.

Based on the curves of Figure 2.2, and all else being equal, it would seem that the application would be best suited with the lowest frequency possible, maximizing sensitivity through the steel. However, lowering the frequency of excitation does not come without its drawbacks. First of all, when talking about an inductive sensing approach, lowering the frequency equates to less signal which equates to a higher noise floor. This will be discussed more in the following section. More importantly, if the goal for the application is to scan at 1-2” per second while maintaining resolution, data-rate becomes very important. Since the maximum data rate is equal to the lowest frequency of excitation (this will be discussed further in the following section as well), and a target resolution of 5 measurements per inch is reasonable, then the lowest excitation frequency possible is 5-10 Hz. 10 Hz is right on the inflection point of the frequency sensitivity curve for typical pipeline properties. Therefore, 10 Hz makes sense as the lowest frequency of excitation and will be used in the following

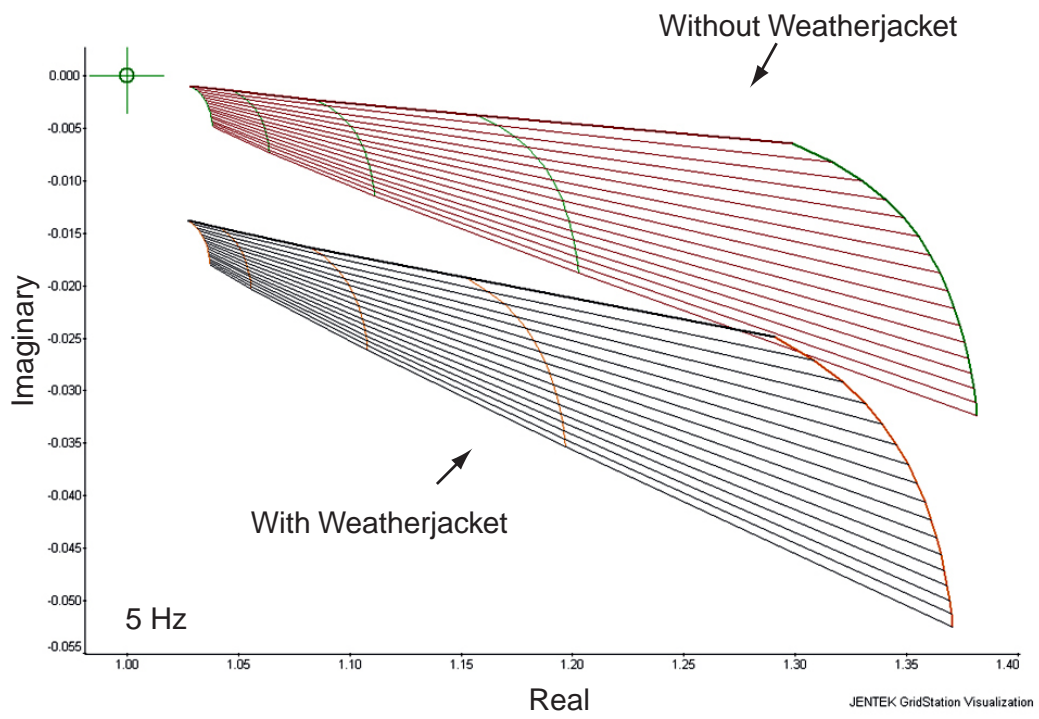


Figure 2.3: Thickness-lift-off grid with and without a weatherjacket layer. The introduction of the weatherjacket causes a large phase shift in the sensor response but does not greatly affect the sensor's sensitivity through the steel.

analysis. For higher $\mu\sigma$ products, it may be necessary to drop the excitation frequency to 5 Hz.

2.2 Noise Analysis for JENTEK Instrumentation

JENTEK has recently fully redesigned their proprietary instrumentation since the instrumentation presented in [38]. The redesign was largely motivated by the instrumentation requirements presented by the CUI problem and can be summarized by the flowchart seen in Figure 2.4. Based on Figure 2.2, a change in steel thickness from 0.45” to 0.5” can reliably cause a change in signal of $5e-4$ at 10Hz based on an air point of magnitude 1.0. Therefore, in order to be able to measure thickness to greater than a 0.005” accuracy, impedance must be measured to greater than a $5e-5$ precision. This can be accomplished by the 16-bit accurate JENTEK instrumentation which can resolve signal magnitude changes down to $1.5e-5$.

Given that the instrumentation can achieve the required accuracy, the question that remains is: How noisy can the sensor’s conditioned signal be once it reaches the analog-to-digital converter (ADC) and digital signal processing (DSP) module? From there, we can work back to the required signal level from the sensor.

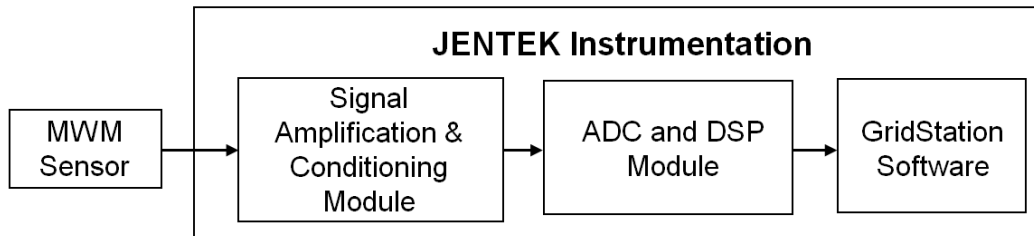


Figure 2.4: Flowchart summarizing the structure of JENTEK proprietary instrumentation.

Although complicated in its efficient implementation, the DSP module effectively performs a Fourier transform with an 80 MHz sample rate to determine the magnitude

and phase components of the incoming signal. Assuming a noisy 1 V peak, 10 Hz signal at the input of an infinitely precise analog to digital converter with an 80 MHz sampling rate, we can relate input signal noise to measured impedance noise. Then, by running this impedance data through the grid, we can relate the input noise to thickness measurement noise.

As long as the gain of the first stage of the signal amplification and conditioning module is large enough, the sensor output noise and input noise on the first stage will be the dominant sources. With intelligent amplifier design, the effect of thermal noise and input current noise can be minimized so that the dominant noise source is the voltage noise present at the input to the first stage. Since these noise sources are specified by their amplitude spectral density (ASD) in $\text{nV}/\sqrt{\text{Hz}}$ it would be most convenient to correlate the ASD of the noise at the ADC to the noise in thickness measurements. The spectral density of the noise source is assumed to be flat and band-limited to half the sampling frequency because there is an anti-aliasing analog filter. The analysis is performed using a Monte Carlo simulation approach in Matlab.

Figure 2.5 summarizes the results of this analysis. The x-axis represents the ASD of the input signal in $\text{nV}/\sqrt{\text{Hz}}$ and the y-axis represents the resulting standard deviation (std) of the thickness measurement based around an operating point of 0.5” thick steel at 2” of lift-off. As expected, the relationship is very linear. Since the goal is to have absolute thickness measurements within 0.005”, it is reasonable to require a thickness measurement standard deviation of less than $0.005/3 = 0.0017$ ”. This is exceeded with a $480\text{nV}/\sqrt{\text{Hz}}$ input noise ASD.

2.3 Sensor Design Analysis

As long as the gain of the first stage of the signal amplification and conditioning module is large enough, the sensor’s output noise and the first amplifier stage’s input

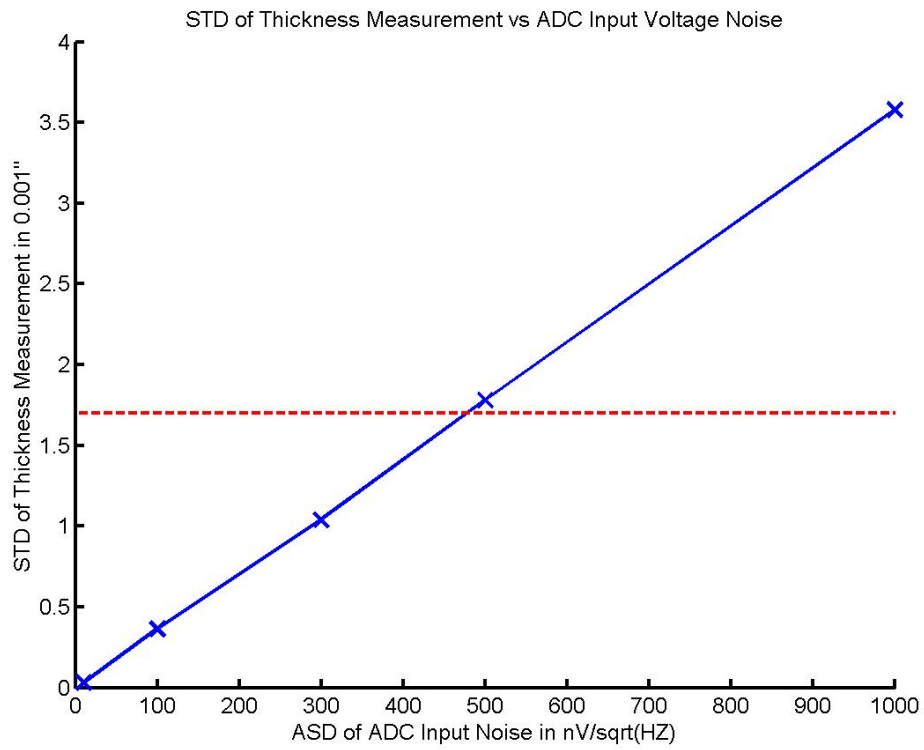


Figure 2.5: STD of steel thickness measurement vs ASD of ADC input noise. This is based around a measurement of 0.5” thick steel at 2” of lift-off. The target thickness measurement standard deviation of 0.0017” is exceeded with an input noise ASD of $480\text{nV}/\sqrt{\text{Hz}}$.

noise will be the dominant noise sources. Therefore, we can analyze various sense element types for output signal level vs. noise and see whether they satisfy the requirement established in the previous section.

2.3.1 Inductive Sense Element

The most common MWM sensor structure has an inductive element which is a loop or coil of wire. The difficulty with an inductive element is that its output voltage signal scales with frequency. Therefore, at low frequencies the output signal of an inductive signal is at very low levels. The advantages of an inductive element are that it has virtually no output noise as long as measurements are made in an electromagnetically quiet environment or with sufficient shielding and that the signal level can be ramped up without limit by increasing the current in the primary winding and the number of windings in the secondary coil. The question is whether it is practical to construct an array of such inductive elements given typical input noise levels of front-end stages.

A state-of-the-art low-noise instrumentation amplifier, such as Analog Devices' AD8429, has a $1 \text{ nV}/\sqrt{\text{Hz}}$ input voltage noise number. Careful front-end design can allow this input noise number to be achieved without input current noise and resistive noise significantly contributing, but achieving a significantly lower noise number is not practical. Theoretically, N instrumentation amplifiers can be placed in parallel, each with their gain reduced by a factor of N , and with their outputs summed to achieve a \sqrt{N} noise improvement [39], but this is a very electronically expensive way to achieve noise reduction. Therefore a maximum gain of 480 (see Figure 2.5) can be used in the signal amplification module before the signal reaching the ADC would be too noisy to achieve a 0.005" accurate thickness estimate.

We need to choose a representative sensor structure to analyze the voltage levels expected at the output of an inductive sensor suitable for CUI. For this purpose, a single rectangular drive of width 3" will work. For this analysis, the length of the

rectangular drive will be large enough that it can be approximated as infinite. From experience, this is about as small a drive construct as can be used to reasonably expect sensitivity through 0.5” of steel and 2” of lift-off since depth of sensitivity decreases with decreasing sensor size. The sense element is a 0.5” square loop, which is the largest sense element that will reasonably provide the measurement resolution needed (measurement resolution is discussed further in Chapter 4).

The magnetic flux through the sense element, Φ_B , is defined as the surface integral of the magnetic field over the area of the element:

$$\Phi_B = \iint_A \mathbf{B}(\mathbf{r}, t) \cdot d\mathbf{A} \quad (2.2)$$

The induced voltage, V_I , on a single loop element is given by the rate of change of the magnetic flux:

$$V_I = -\frac{d\Phi_B}{dt} \quad (2.3)$$

Since we know that the magnetic field a distance r away from an infinitely long current carrying wire in air is

$$B(t) = \frac{\mu_0 I(t)}{2\pi r} \quad (2.4)$$

we can calculate that the induced voltage on a single-loop element due to a 1 A peak 10 Hz sinusoid in the long rectangular drive will have an amplitude of 107.4 nV. Therefore, since our instrumentation gain is limited to 480, we need another factor of nearly 20,000 to achieve the required 1 V peak signal at the ADC. This can be achieved with a 20-turn sense element, 100-turn drive and 10 A of drive current.

Some quick, back of the envelope calculations will show that this is not a practical sense element construction. First of all, a 20-turn sense element is difficult, but not impossible to construct. This could be done using a multiple layered flexible circuit-board with a few turns on each layer. The drive is the real problem. If the drive is

at least 18" long and 3" wide (these dimensions will be discussed in more detail in following chapters) then 100 turns is 350 ft of wire. With a 50 V drive source, the wire can only have a resistance of 0.0143 Ω /ft. This can be achieved with 21 AWG wire and would weigh approximately 1 lb. However, the maximum current that an unbundled strand of 21 AWG wire can carry is less than 10 A [40]. To avoid a temperature rise of less than 20°C, our 100 turn drive would have to be constructed out of 16 AWG wire and would weigh over 2 lbs. While this is still conceivable, the drive would not be flexible, which makes it impractical for use in measuring on pipelines.

In addition to not being flexible, it would be very difficult to create a drive signal of 10 A at 50 V without introducing significant noise into the measurement. Higher voltage, higher power amplifiers tend to have poorer noise characteristics. Placing many lower power amplifiers in parallel and summing their outputs results in their output noise to sum as the square root of their squares. So, even if the drive could be made flexible, there would be practical difficulties with constructing a low-noise, high-power amplifier.

Probably the most significant issue is that this analysis ignores the $1/f$ low frequency characteristic of the input voltage noise of all op amps. Therefore, while at higher frequencies 1 nV/ $\sqrt{\text{Hz}}$ is an achievable input noise ASD, in practice the effective input noise will be significantly higher.

2.3.2 DC Field Saturation

Since inductive sensing is not practical at these low frequencies, one strategy would be to try to saturate the pipeline steel, dropping its relative magnetic permeability to 1. This would allow higher frequencies to have sensitivity through the steel which would, in turn, provide more signal and allow the target SNR to be achieved. The question is whether or not saturation of the pipe steel is achievable under reasonable conditions.

As an example, consider an electromagnet with a ferromagnetic yoke as a means of applying a high DC magnetic field. Using Ampere's law and taking the line integral of the magnetic field intensity around a path through the center of the yoke and MUT (see Figure 2.6), we end up with Equation 2.5.

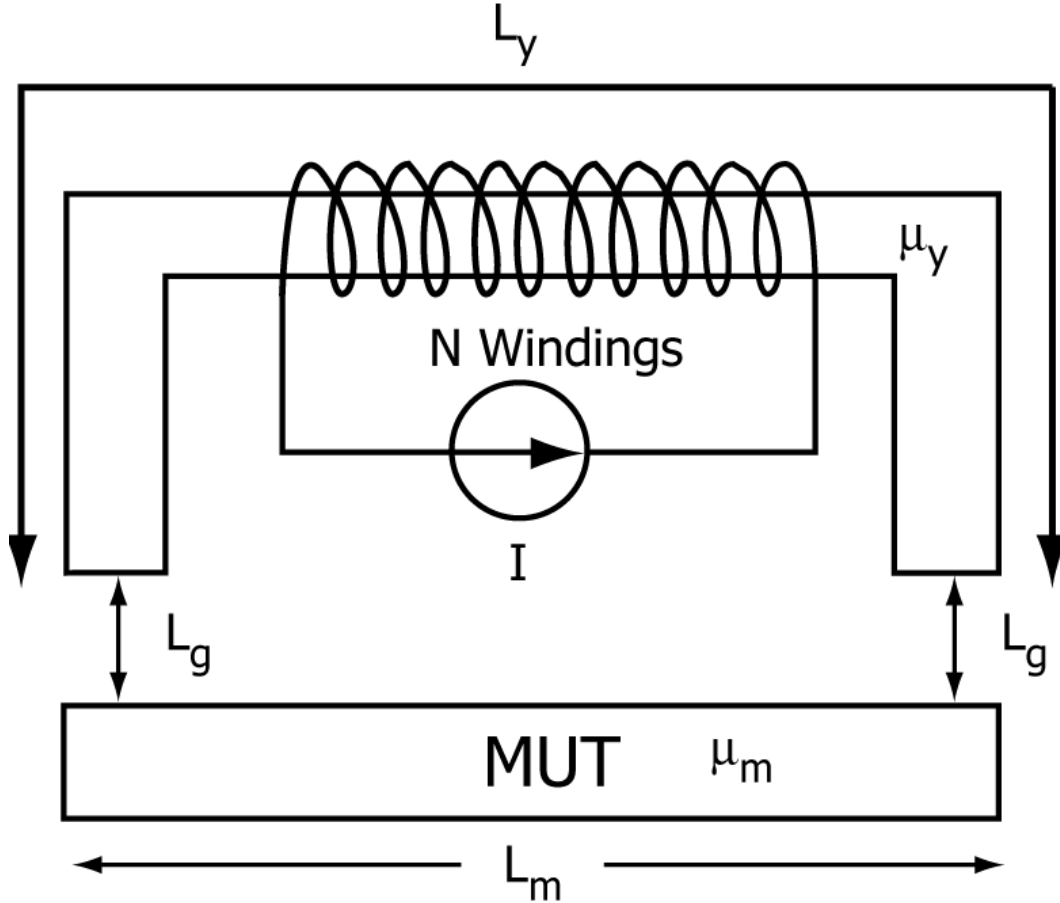


Figure 2.6: Diagram of the magnetic circuit when trying to saturate steel through insulation using a magnetic yoke. The subscript g refers to the air-gap, the subscript m refers to the MUT and the subscript y refers to the yoke.

$$\oint \mathbf{H} \cdot d\mathbf{l} = NI = H_y L_y + 2H_g L_g + H_m L_m \quad (2.5)$$

The subscript g refers to the air-gap, the subscript m refers to the MUT and the subscript y refers to the yoke. N is the number of windings, and I is the current

driven through them. This magnetic circuit assumes no losses to fringing effects which will increase with an increased air gap. We also know from boundary conditions that the normal component of \mathbf{B} must be continuous. Therefore:

$$\mu_0\mu_y H_y = \mu_0 H_g = \mu_0\mu_m H_m \quad (2.6)$$

where μ_y and μ_m are the relative magnetic permeabilities of the yoke and steel respectively. Combining these two equations we get:

$$NI = 2\mu_m H_m L_g + H_m L_m + \frac{\mu_m}{\mu_y} H_m L_y \quad (2.7)$$

Based on Figure 2.7, a magnetic field intensity of at least 10,000 A/m is needed within the MUT in order to lower its permeability at all. For a permeability 80 rel., an air gap of 2 inches and a MUT length of 12 inches, over 84,000 Amp-turns are needed. Furthermore, to significantly lower the MUT's permeability, an order of magnitude more Amp-turns would be needed. No combination of number of turns and current makes this feasible. This result ignores any losses due to fringing effects and the difficulties in creating a yoke with high permeability that would not begin to saturate in the presence of these high field intensities.

2.3.3 Active Sense Elements

While inductive sensing is not practical based on the previous analysis, another approach is to use an active sense element in place of the inductive coil. The advantage of active elements such as SQUID magnetometers, Hall-effect devices and magnetoresistive elements is that they are directly sensitive to magnetic fields as opposed to the rate of change of the magnetic field. Therefore, equal sensitivity is achieved at all frequencies (within a certain bandwidth). Figure 2.8 summarizes the

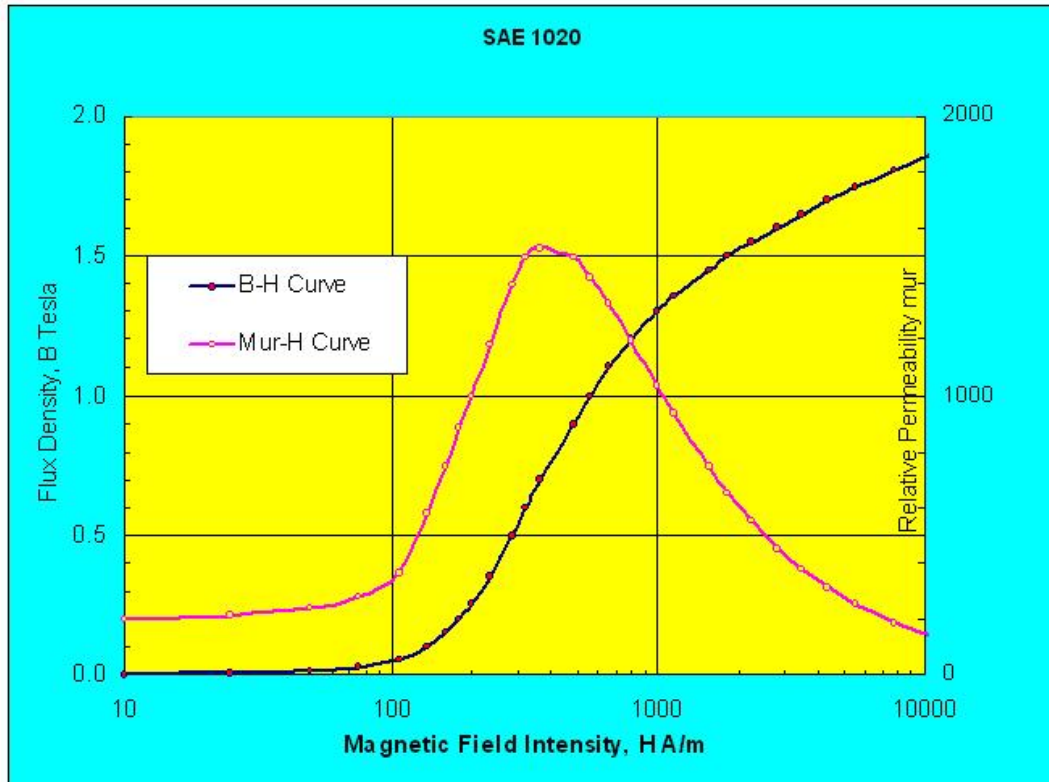


Figure 2.7: B-H curve for a steel with a carbon content comparable to pipe steel. In order to lower the steel permeability slightly, over 10,000 A/m magnetic field intensity is needed within the MUT. To saturate, even higher field intensities are needed [41].

relative sensitivities of different sensing approaches. It should be noted that one of the more sensitive methods according to the table, the search-coil, is just another way of referring to inductive sensing. Figure 2.8 does not capture the low-frequency drawbacks for this method.

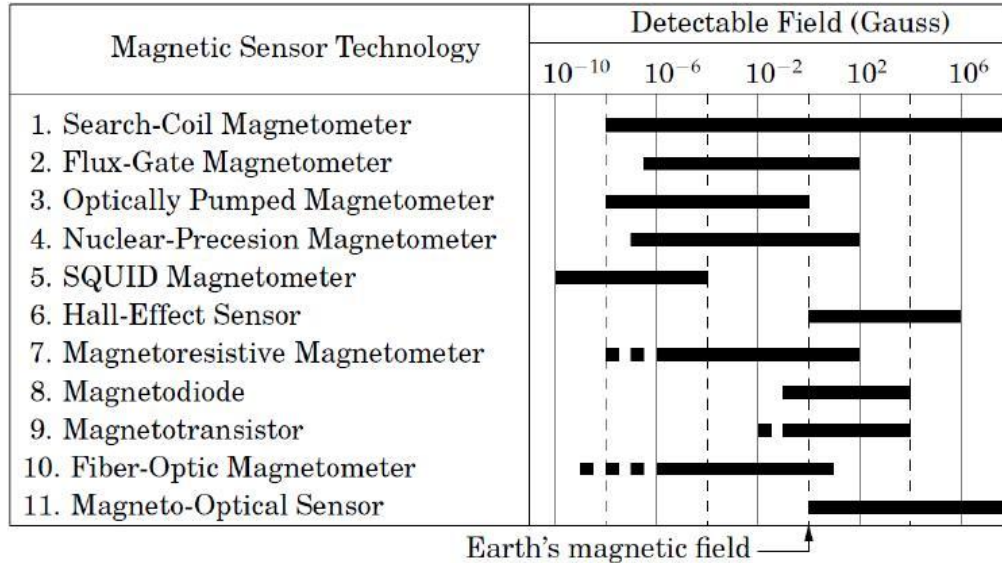


Figure 2.8: Comparison of the achievable sensitivity of different magnetic sensor technologies [42].

According to Figure 2.8, the SQUID (Superconducting Quantum Interference Device) must be considered due to its extreme sensitivity to magnetic field. A SQUID's output voltage is a periodic function of applied magnetic flux with the periodicity of one flux quantum ($\Phi_0 = h/2e = 2.07e43Wb$) resulting in a sensitivity on the order of less than one flux quantum in the proper configuration [43]. SQUID based measurement systems can be relatively wide-bandwidth (DC to 100 kHz) and operate over a relatively wide dynamic range (greater than 100dB). Much research in the field of NDE has been dedicated to SQUID technologies [44] - they have been used for a variety of applications including the detection of flaws in steel plates [45]. The main issue with SQUID sensors is that they operate below the superconducting transition temperature (T_C) of the materials used for the fabrication of the device.

Even high- T_C devices which operate at liquid-nitrogen temperatures [46] would result in a device that would be impractical to use outside of a lab setting.

A more practical active sense element would be a Hall-effect probe which operates on the Hall-effect principle. When current is flowing in a semiconductor in the presence of a magnetic field, a force is applied to the charge carriers of the semiconductor perpendicular to the direction of the applied magnetic field and the flow of current. This causes a voltage to be induced across the semiconductor edges. Unfortunately, Hall-effect devices are at the other end of the spectrum from SQUID devices: while commercially available and easy to implement practically, they lack the sensitivity to low-level magnetic field changes needed for CUI. This deficiency is demonstrated in Figure 2.8.

A reasonable compromise between the sensitivity of SQUID devices and the practicality of Hall-effect devices are magnetoresistive (MR) elements. Anisotropic magnetoresistive elements (AMR) and giant-magnetoresistive (GMR) elements are both commercially available and provide high sensitivity to magnetic field changes by taking advantage of changes in the magnetoresistance of thin films of ferromagnetic metals and alloys in the case of AMR and of metallic magnetic superlattices in the case of GMR. The details of the physics of magnetoresistance are complicated and unnecessary for the following analysis. What is needed are the typical characteristics of commercially available sense elements.

2.3.4 Giant Magnetoresistive Sense Elements

Due to their previous use in a distributed drive magnetometer in [37] and their high sensitivity to magnetic fields (in general, the GMR effect is quoted to have a 4x maximum sensitivity as compared to the AMR effect [47]), it makes sense to first consider a GMR element for use in CUI. After a review of suitable commercially available sensors, the majority of which are produced by NVE Corporation, the best

SNR would provide an output voltage sensitivity of 30 mV/Gauss at a 10 V power supply with an output noise level of approximately 10 nV/ $\sqrt{\text{Hz}}$ [48]. The output noise level is dominated by the thermal noise of the effective output resistance of the sensor. This output resistance varies from 5 k Ω to 30 k Ω depending on the dynamic operating range of the sensor. Given the sensor construct analyzed in Section 2.3.1, a 1 A peak 10 Hz sinusoid in the long 3" rectangular drive will have a field strength of 0.0525 Gauss. Therefore, an output voltage of 1.58 mV would result. With an allowable maximum gain of 48 due to the output noise of the GMR sense element, only 14 drive turns would be needed to satisfy the signal level requirements.

It needs to be noted here that the GMR chip specification quotes its sensitivity in units of mV/Oe as opposed to mV/Gauss, which seems to imply that its sensitivity is actually dependent on its internal permeability. Since this does not make sense, the assumption was made that it was a units misprint. If this is incorrect, then the sensitivity of the GMR would decrease by a factor of its internal permeability.

One drawback to GMR sense elements is that they require DC field biasing in order to be in their linear regime. Furthermore, the commercially available sensors do not have built-in secondary windings (which will be discussed further in Section 2.4). Therefore, it makes sense to investigate whether AMR elements would be more suitable.

2.3.5 Anisotropic Magnetoresistive Sense Elements

Commercially available AMR sense elements from Honeywell have excellent performance characteristics. A suitable sensor has a considerably lower output noise floor than that of its GMR counterpart at 4 nV/ $\sqrt{\text{Hz}}$, and at a 10 V power supply its output voltage sensitivity is 50 mV/Gauss [49]. Therefore, the SNR requirements for CUI can easily be satisfied. Since AMR elements do not require biasing to be in their linear region and they provide offset straps which can be used as secondary windings,

AMR elements are the clear choice for approaching the CUI problem.

For the purpose of the rest of this document, AMR sense elements will simply be referred to as MR sense elements.

2.4 Feedback Configuration for the Magnetoresistive Sense Element

Even though an MR sense element's combination of high magnetic sensitivity and relatively low output noise level makes it possible to achieve the required SNR based on the analysis from 2.3, implementing a successful MR sense element has other practical challenges. Magnetoresistive sense elements suffer from hysteresis, non-linearity and temperature dependence. A single MR chip with a localized drive, as pictured in Figure 2.9, was constructed in order to quantify these effects. Measurements demonstrated that the drift due to temperature was the most significant noise source. Figure 2.10 summarizes the results of the temperature test. According to the specification sheet of the MR chip, with a supply voltage of 8V the output signal should have a temperature dependence of $-0.30\ \%/^{\circ}\text{C}$ when supplied with a constant voltage source and a temperature dependence of $-0.06\ \%/^{\circ}\text{C}$ when supplied with a constant current source. In practice, it was closer to $-0.50\ \%/^{\circ}\text{C}$ and $-0.20\ \%/^{\circ}\text{C}$ respectively. After trying to control the temperature of the MR elements with active cooling, it became clear that this was not practical given the measurement accuracy required. Even with consistent airflow over the elements, it would be difficult to maintain the chip's temperature within 1°C . With a constant current power source, a single degree of temperature related drift alone would account for a change in thickness measurement of $0.005''$ - $0.100''$ depending on the measurement conditions.

There is an elegant solution to this temperature dependence that also addresses any potential problems presented by an MR's hysteresis or non-linearity. In [37], it was

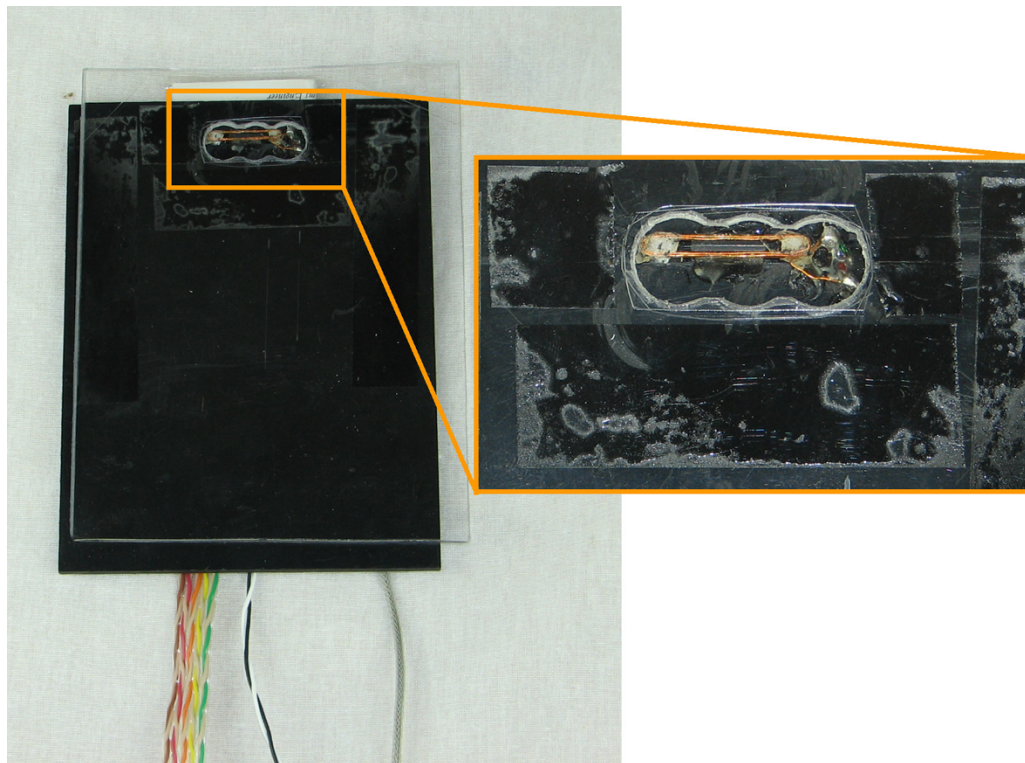


Figure 2.9: Single MR sense element with small wavelength drive constructed to quantify MR sense element noise sources.

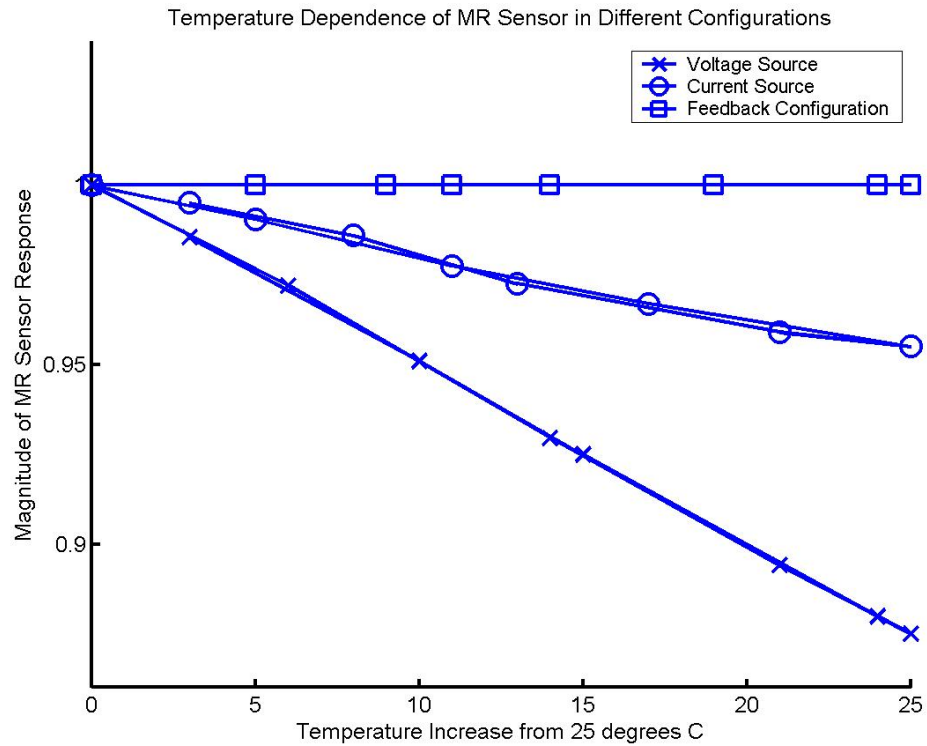


Figure 2.10: Results of the MR temperature test showing that the MR element has an output signal temperature dependence of $-0.50\ \%/^{\circ}\text{C}$ when supplied with a constant voltage source and a temperature dependence of $-0.20\ \%/^{\circ}\text{C}$ when supplied with a constant current source. This effect is eliminated when the sensor is placed in a feedback configuration.

necessary to place a giant-magneto-resistive sense element in a feedback configuration in order to widen the dynamic range of the sensor. With an MR element, dynamic range is not as much of a concern: typical MR dynamic ranges include field strengths up to ± 6 Gauss. A similar structure, shown in Figure 2.11, which has a secondary winding wrapped around the MR element, can still be used advantageously for the CUI application. Instead of sensing the bridge voltage of the MR sensor, the current in the secondary loop required to null the MR element, I_N , is measured. This removes the MR sense element transfer function, along with its temperature dependence, hysteresis and nonlinearity, from consideration.

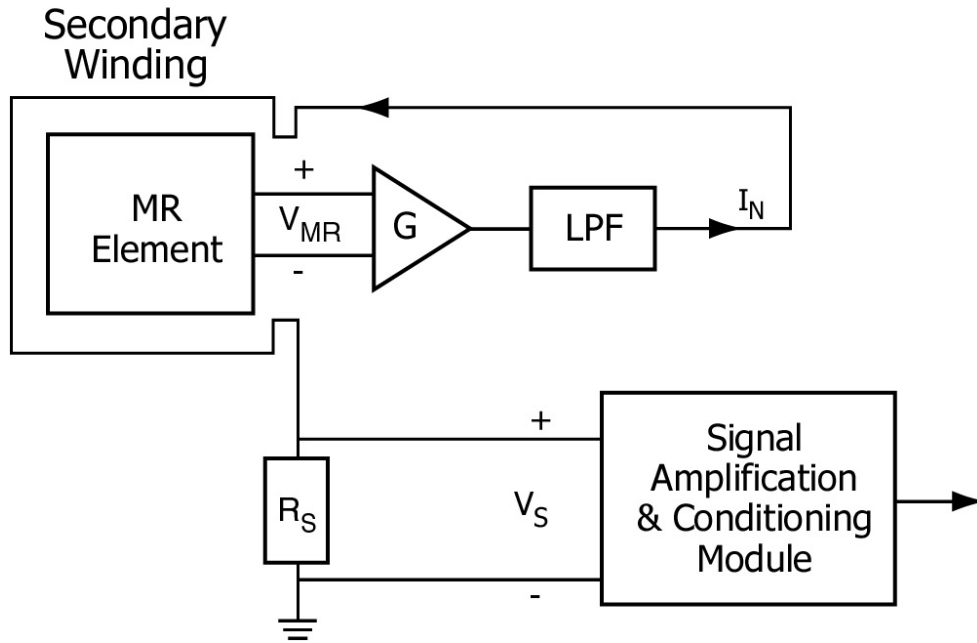


Figure 2.11: MR sense element in a feedback configuration with a secondary winding. Instead of sensing the bridge voltage of the MR sensor, the current in the secondary loop required to null the MR element, I_N , is measured. This removes the MR sense element transfer function, along with its temperature dependence, hysteresis and nonlinearity, from consideration.

The major drawback of this configuration is the need to bandwidth limit the feedback loop for stability, especially when cabling is part of the loop. This is not

an issue for the CUI application as only frequencies under 1 kHz are required and, even with long cables, a bandwidth limitation of 10 kHz is sufficient. If this sensor structure were to be needed for higher frequencies (a typical MR element in open-loop has a bandwidth of 1 MHz), then either the sensor would have to be operated in open loop or the effects of the cabling would have to be minimized.

Conveniently, many MR sense elements have built-in offset straps which can be used as the secondary winding. Since these offset straps are so close to the sensitive area of the chip, very little current is required to offset large magnetic fields. Figure 2.10 also shows measurements taken with the MR sensor in the closed loop configuration: the measurements were insensitive to temperature.

2.5 Prototype Magnetoresistive MWM-Array

Based on the analysis of Section 2.3, a prototype Magnetoresistive MWM-Array, or MR-MWM-Array, was developed and is pictured in Figure 2.12. The prototype MR-MWM-Array has magnetoresistive sense elements spaced 0.5” apart mounted on flexible FR4, which is suitable for wrapping around curved surfaces. Strain relief boards are in-line with the MR chips and decoupling capacitors to allow for achieving a 2” curvature radius without damaging the electronics. The MR-MWM-Array is mounted onto a wound drive with 80 turns of 26 gauge rectangular wire. The rectangular wire was chosen so that the placement of each conductor could be controlled in the winding process with each conductor stacked against the next. This has important implications when modeling the sensor and will be discussed in Chapter 3. Since the bundled 26 gauge rectangular wire can handle 2 A RMS with a temperature rise of less than 30°C [40], achieving the required magnetic field intensity to achieve the necessary noise levels is possible.

Figure 2.13 summarizes the results of the successful proof-of-concept measure-

ments. Only the results of a single channel are plotted, but all channels had similar results. Measurements were made at 4 different locations on each of three steel plates with respective thicknesses of 0.250", 0.375" and 0.5". Measurements were made at nominally 1.8" of lift-off, although no great effort was made to control the lift-off explicitly. The steel thicknesses estimated were accurate to within 0.005" of the micrometer-measured thickness at each location. The 0.5" steel plate was slightly warped and therefore had a little more thickness variation from location to location. Furthermore, the variation from measurement to measurement was under ± 0.001 ". As expected, the magnetic permeability of the steel varies significantly from plate to plate and from location to location within a given plate (the variation observed was from 108-145 rel permeability). Also, the lift-off measured varied significantly from location to location by over 0.1". The grid methods were able to correct for these variations using the Cartesian-geometry forward-model of the MWM. The implications of not being able to correct for these variations will be discussed more in the following chapter.



Figure 2.12: Magneto-resistive sense elements spaced 0.5" apart mounted on flexible FR4, which is suitable for wrapping around curved surfaces. Strain relief boards are in-line with the MR chips and decoupling capacitors to allow for achieving a 2" curvature radius without damaging the electronics. The MR-MWM-Array is mounted onto a wound drive with 80 turns of 26 gage rectangular wire.

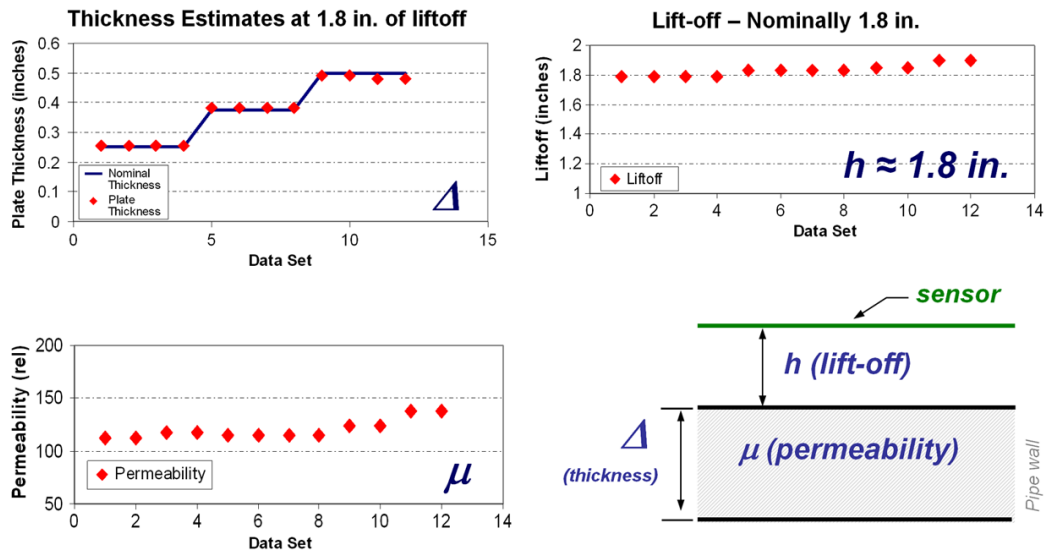


Figure 2.13: Preliminary measurements demonstrating the ability to accurately estimate steel thickness. Only the results of a single channel are plotted, but all channels had similar results. Measurements were made at 4 different locations on each of three steel plates with respective thicknesses of 0.250”, 0.375” and 0.5”. Measurements were made at nominally 1.8” of lift-off, although no great effort was made to control the lift-off explicitly. The steel thicknesses estimated were accurate to within 0.005” of the micrometer-measured thickness at each location. The 0.5” steel plate was slightly warped and therefore had a little more thickness variation from location to location.

CHAPTER 3

MODELING OF THE MWM IN CYLINDRICAL COORDINATES

The following sections describe an extension into cylindrical coordinates of the forward model of the MWM. Structurally similar to the Cartesian geometry MWM forward model found in [36]-[38] and based on the transfer relations developed by Professor Melcher [50], the cylindrical coordinate derivation is necessary for accurately modeling the MWM interaction when wrapped around a cylindrically shaped MUT. Furthermore, since this model will be used in many applications where the material transport time interval determined by the characteristic length of the MWM sensor divided by the scanning speed is comparable to the period of the sensor's current excitation, it will be important to incorporate the convective effect into the model [50].

The MWM is analyzed in the magnetoquasistatic (MQS) regime, which ignores the term due to displacement current in Ampère's law and assumes that the MUT is comprised of very good conductors and very good insulators (see the end of Section 3.2.1). This assumes that the spatial period of the electromagnetic wave at the operating frequency is much greater than all other characteristic lengths including the spatial wavelength of the winding construct. Therefore, the electrodynamic contribution is negligible. Since the MWM is traditionally operated between DC and 40 MHz, and the period of the winding construct is generally on the order of a few inches or smaller, this assumption is always satisfied by at least 2-3 orders of magnitude. If the frequency is raised much above 40 MHz, capacitive effects need to be considered [36].

The MWM is also analyzed in the sinusoidal steady state with angular frequency ω . Therefore, time dependent quantities can always be written in the following form in the frequency domain:

$$\mathbf{F}(\vec{r}, t) = \Re\{\hat{\mathbf{F}}(\vec{r})e^{j\omega t}\} \quad (3.1)$$

where \hat{F} is a complex amplitude function only of spatial coordinates \vec{r} . Therefore, derivatives in the time domain can be transformed into multiplications by $j\omega$ in the frequency domain.

The analysis of the MWM can be greatly simplified if the current density in each drive winding can be considered uniform. This assumption provides a known current density whose spatial Fourier modes can be analyzed separately. The final magnetic field is simply the superposition of the individual solutions. The assumption is valid if the dimensions of the individual conductors are much smaller than the imposed spatial wavelength, the distance between the drive conductors and the secondary conductors, and the distance between the sensor conductors and the MUT. This is the case for the sensors developed for CUI. These models can be extended into the regime where these assumptions are invalid by using a collocation point method [37].

3.1 Motivation for the Cylindrical MWM Model

Most standard eddy-current methods use a reference calibration method when determining material properties or inspecting for flaws. They use a set of known standards and then empirically fit the resulting measurement to the known standard dataset. This often requires the assumption that properties other than the one of interest are constant. In the case of CUI this would be a terrible assumption - variations in insulation thickness can be dramatic from location to location. Simply moving from the top of the pipeline to the bottom can result in insulation changes on the order of inches due to sagging caused by the weight of the insulation itself.

Figure 3.1 shows the relative impedance changes due to a 10% change in each material property. All perturbations were around a nominal 0.5” thick steel plate with 2 inches of insulation, a 0.02” aluminum weatherjacket and a sensor lift-off of 0.5”. The data is normalized so that the sensor response in air corresponds to $1+0j$. It is clear by inspection that, unless there is good correction for any variation in pipeline material properties, small changes in thickness measurement will get swamped out by the material variation. Unfortunately, the property of interest is the property to which the sensor is the least sensitive. Since these material property variations are inevitable, a reference calibration method is not practical and the MWM approach of calibrating in air and simultaneously estimating all properties using a multiple frequency inversion method, as overviewed in Section 1.5, is a justifiable approach.

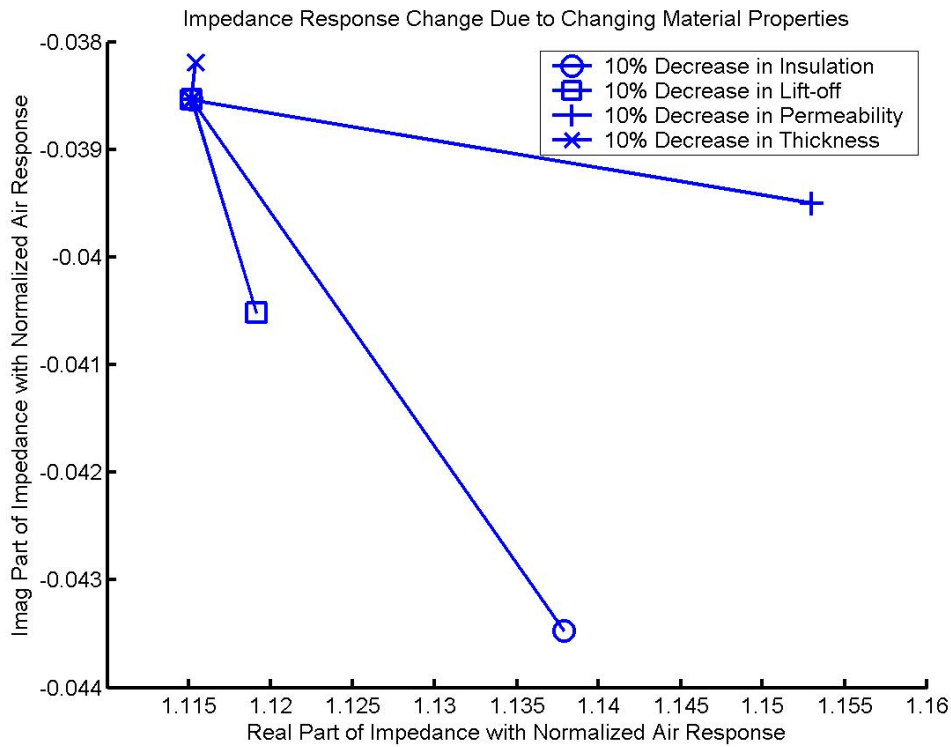


Figure 3.1: A plot of the impedance response change due to a 10% change in each material property. All perturbations were around a nominal 0.5” thick steel plate with 2 inches of insulation, a 0.02” aluminum weatherjacket and a sensor lift-off of 0.5”. The data is normalized so that the sensor response in air corresponds to $1+0j$.

Furthermore, the MWM models must be extended into cylindrical coordinates for the CUI application as the Cartesian-coordinate assumption is not valid when wrapping an MWM around a pipeline. The air-point itself can change by as much as 20% from a sensor being flat to being wrapped around a pipeline. Simply trying to normalize this effect out by using an air-point calibration at the correct diameter could result in as much as a 50% error in thickness measurement.

3.2 MWM Forward Model in Cylindrical Coordinates: Drive Aligned with ϕ -Axis

This section contains the equations that predict the response of an MWM when wrapped around a cylindrical material in the typical scan orientation for the CUI application. The model assumes that the main legs of the primary winding are wrapped around the cylinder in the circumferential direction and that the periodicity of the primary winding is in the axial direction. Secondaries are assumed to be on either side of the primary. Material properties are assumed to be independent of z , ϕ and time. Material interfaces are assumed to be at cylindrical surfaces of constant ρ . Figure 3.2 shows the modeled MWM sensor structure.

3.2.1 Maxwell's Equations

In the MQS regime, magnetic fields H in the presence of conducting materials must satisfy the magnetic diffusion equation:

$$\nabla^2 \mathbf{H} - j\omega\sigma\mu\mathbf{H} = 0 \quad (3.2)$$

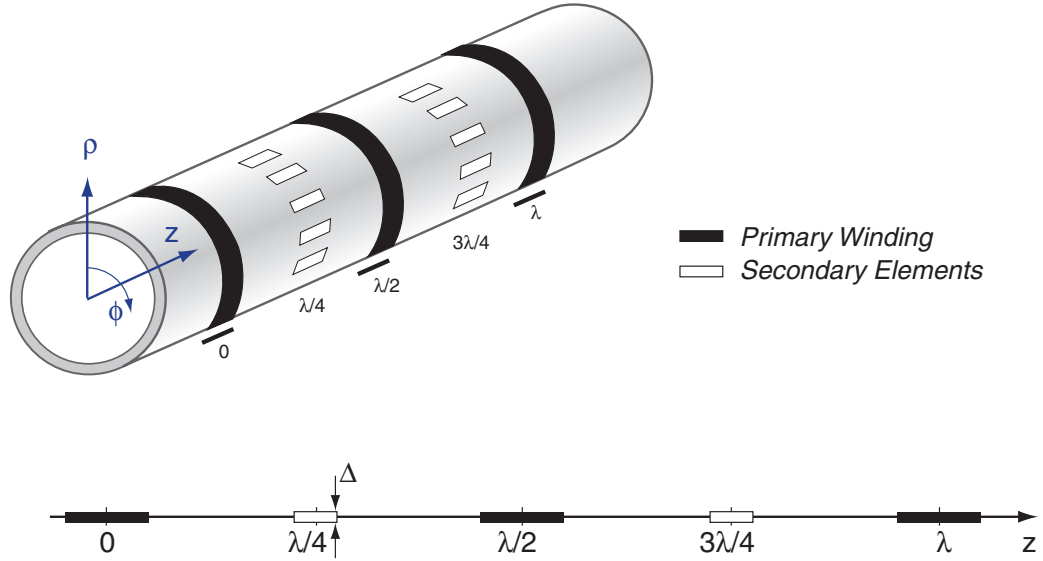


Figure 3.2: MWM geometry when wrapped around a cylindrical material with the drive aligned circumferentially.

When solving the magnetic diffusion equation, it is often easier to formulate the problem in terms of the magnetic vector potential \mathbf{A} , defined as follows:

$$\nabla \times \mathbf{A} = \mathbf{B} \quad (3.3)$$

Combining this definition with Faraday's law:

$$\nabla \times \mathbf{E} = -j\omega\mathbf{B} \quad (3.4)$$

results in the following:

$$\nabla \times \mathbf{E} = \nabla \times (-j\omega\mathbf{A}) \quad (3.5)$$

This states that \mathbf{E} and $-j\omega\mathbf{A}$ are vector fields with equal curl. Therefore, since vector fields with equal curl must be equal within an offset of a gradient of a scalar field, we

can formulate results in the following:

$$\mathbf{E} = (-j\omega\mathbf{A}) - \nabla\Phi \quad (3.6)$$

where Φ is known as the electric scalar potential. Next we take into consideration Ampère's law, neglecting the term due to displacement current since we are in the MQS regime,

$$\nabla \times \mathbf{H} = \mathbf{J} \quad (3.7)$$

We also require Ohm's law, including the term due to the current induced by the Lorentz force on the charge carriers, since the MUT is in motion.

$$\mathbf{J} = \sigma(\mathbf{E} + \mathbf{v} \times \mathbf{B}) \quad (3.8)$$

Remembering $\mathbf{B} = \mu\mathbf{H}$ we can perform the following calculations:

$$\nabla \times \mu^{-1}(\nabla \times \mathbf{A}) = -\sigma(j\omega\mathbf{A} + \nabla\Phi - \mathbf{v} \times \mathbf{B}) \quad (3.9)$$

$$\nabla(\nabla \cdot \mathbf{A}) - \nabla^2\mathbf{A} = -j\omega\mu\sigma\mathbf{A} - \nabla(\mu\sigma\Phi) + \mu\sigma(\mathbf{v} \times \nabla \times \mathbf{A}) \quad (3.10)$$

$$\nabla^2\mathbf{A} - j\omega\mu\sigma\mathbf{A} = \nabla(\nabla \cdot \mathbf{A} + \mu\sigma\Phi) - \mu\sigma(\mathbf{v} \times \nabla \times \mathbf{A}) \quad (3.11)$$

It is important to note that these steps implicitly assume that all layers of the MUT are isotropic. That is, the off-diagonal terms of the conductivity and permeability tensor of each layer of the MUT are zero. This is a good assumption for CUI application: most metals, including steel and aluminum and the materials used for insulating pipelines, satisfy this requirement.

Since Equation 3.3 only defined the magnetic vector potential with respect to its curl, we have the freedom to define the magnetic vector potential's divergence in order to uniquely determine it within a constant of integration. A convenient definition sets

the first term of the RHS of Equation 3.11 to zero by letting

$$\nabla \cdot \mathbf{A} = -\mu\sigma\Phi \quad (3.12)$$

Therefore, we have reduced the problem to determining the magnetic vector potential that satisfies

$$\nabla^2 \mathbf{A} - j\omega\mu\sigma \mathbf{A} = -\mu\sigma(\mathbf{v} \times \nabla \times \mathbf{A}) \quad (3.13)$$

In the limit where $\mathbf{v} = 0$, Equation 3.13 further reduces to:

$$\nabla^2 \mathbf{A} - j\omega\mu\sigma \mathbf{A} = 0 \quad (3.14)$$

Since the drive currents are only in the $\hat{\phi}$ direction and independent of ϕ as shown in Figure 3.2, the magnetic vector potential solution to Equation 3.13 must also only have a $\hat{\phi}$ component and be independent of ϕ . Also, since all quantities are independent of ϕ , the $\hat{\phi}$ component of the velocity can be ignored, and we need only be concerned with the \hat{z} component (i.e. $\mathbf{v} = v_z \hat{z}$). So, Equation 3.13 reduces to:

$$\frac{1}{\rho} \frac{\partial}{\partial \rho} \left(\rho \frac{\partial A_\phi}{\partial \rho} \right) - \frac{A_\phi}{\rho^2} + \frac{\partial^2 A_\phi}{\partial z^2} - j\omega\mu\sigma A_\phi - \mu\sigma v_z \frac{\partial A_\phi}{\partial z} = 0 \quad (3.15)$$

It is important to note that when reducing Equation 3.13 to Equation 3.15, taking the Laplacian of a vector in cylindrical coordinates is not as simple as applying the cylindrical coordinate Laplacian to each component of the vector. Making this mistake will result in a differential equation with solution having an incorrect, non-physical ρ dependence based on a zeroth order Bessel function as opposed to the correct ρ dependence based on a first order Bessel function.

Using a separation of variables approach, we can postulate that \mathbf{A} has the form

$$\mathbf{A} = A_{\phi_\rho}(\rho) A_{\phi_z}(z) \hat{\phi} \quad (3.16)$$

and therefore Equation 3.15 further reduces to

$$A_{\phi_z} \left[\frac{1}{\rho} \frac{\partial}{\partial \rho} \left(\rho \frac{\partial A_{\phi_\rho}}{\partial \rho} \right) - \frac{A_{\phi_\rho}}{\rho^2} - j\omega\mu\sigma A_{\phi_\rho} \right] + A_{\phi_\rho} \left[\frac{\partial^2 A_{\phi_z}}{\partial z^2} - \mu\sigma v_z \frac{\partial A_{\phi_z}}{\partial z} \right] = 0 \quad (3.17)$$

We choose for the z dependency of A_ϕ to have the following form with period λ :

$$A_{\phi_{z_n}}(z) = e^{-jk_n z}, \quad k_n = \frac{2\pi n}{\lambda} \quad (3.18)$$

The Fourier harmonic wavenumbers, k_n , are used here as the periodicity in the \hat{z} direction allows us to represent the magnetic vector potential as the superposition of the Fourier wavenumber modes, where n is any integer. This is discussed further in Section 3.2.3. Also, the sign of the exponent here is arbitrary since positive and negative complex wavenumbers need to be treated separately. This will be discussed later in this section.

Plugging Equation 3.18 into Equation 3.17, we are left with the following differential equation:

$$e^{-jk_n z} \left[\frac{\partial^2 A_{\phi_{\rho n}}}{\partial \rho^2} + \frac{1}{\rho} \frac{\partial A_{\phi_{\rho n}}}{\partial \rho} + \left(-k_n^2 - j\mu\sigma(\omega - v_z k_n) - \frac{1}{\rho^2} \right) A_{\phi_{\rho n}} \right] = 0 \quad (3.19)$$

The above is a differential equation whose form is that of the transformed version of the Bessel differential equation given by [51].

$$\frac{d^2 y}{dx^2} - \frac{2\alpha - 1}{x} \frac{dy}{dx} + \left(\beta^2 r^2 x^{2r-2} + \frac{\alpha^2 - f^2 r^2}{x^2} \right) y = 0 \quad (3.20)$$

whose solution is

$$y = x^\alpha [C_1 J_f(\beta x^r) + C_2 Y_f(\beta x^r)] \quad (3.21)$$

Equation 3.19 fits into this form where $x = \rho$, $y = A_{\phi_\rho}$, $\alpha = 0$, $r = 1$, $f = 1$ and

$\beta = j\gamma_n$, and where the complex wavenumber γ_n is defined as

$$\gamma_n = \sqrt{k_n^2 + j\mu\sigma(\omega - v_z k_n)} \quad (3.22)$$

Therefore, the solutions to Equation 3.19 are linear combinations of $J_1(j\gamma_n\rho)$ and $Y_1(j\gamma_n\rho)$, Bessel functions of the first and second kind of the first order. Alternatively, the solution to Equation 3.19 can be written in terms of linear combinations of $I_1(\gamma_n\rho)$ and $K_1(\gamma_n\rho)$, modified Bessel functions of the first and second kind of the first order. Therefore the full solution for each mode of the magnetic vector potential can be written as

$$\mathbf{A}_n = [a_1 I_1(\gamma_n\rho) + a_2 K_1(\gamma_n\rho)] e^{-jk_n z} \hat{\phi} \quad (3.23)$$

It is interesting to note how velocity enters into the model. If a material is moving at velocity v_z relative to a sensor, then the apparent frequency of excitation ω observed in that material is replaced by $\omega - vk_n$. This causes the presence of a non-zero velocity to break the symmetry around $n = 0$ of the complex wavenumbers, requiring that positive and negative wavenumber modes be treated separately. This will be discussed further in Section 3.2.2.

Before continuing, there are a few internal consistencies and assumptions that need to be explored. First of all, the solutions for \mathbf{A} provided by Equation 3.23 have zero divergence. Therefore, revisiting the gauge condition from Equation 3.12, the scalar potential $\Phi=0$, and Equation 3.6 can be rewritten as

$$\mathbf{E} = -j\omega\mathbf{A} \quad (3.24)$$

Boundary conditions must be satisfied by Equation 3.24 in order for this model to be self consistent. First of all, at interfaces of conducting materials, where the tangential component of the electric field must be continuous, the boundary condition is satisfied

as \mathbf{A} has $\hat{\phi}$ component which is tangential to the interface boundaries. However, this is not necessarily the case at the sensor winding interface and in insulating regions near the sensor winding. Without an \hat{r} component to \mathbf{A} and, therefore, \mathbf{E} it appears that electric field continuity cannot be maintained. However, when the conductivity of a layer is zero, the electric scalar potential Φ is not forced to zero by Equation 3.12. So the inconsistency is resolved by an appropriate solution to $\nabla^2\Phi=0$. Furthermore, the component of the magnetic field contributed by the non-zero electric scalar potential is disregarded in the MQS regime. One important consequence of this is that in order for the boundary condition at the winding surface to be met, the layers immediately adjacent to the winding must be insulating. This was already necessary, however, in order to contain the winding currents within the winding.

Plugging Equation 3.23 into Equation 3.3 we can also make some observations on the functional form of \mathbf{B} .

$$\begin{aligned}\mathbf{B}_n &= -\frac{\partial A_{\phi_n}}{\partial z}\hat{\rho} + \frac{1}{\rho}\frac{\partial(\rho A_{\phi_n})}{\partial\rho}\hat{z} \\ &= jk_n [a_1 I_1(\gamma_n \rho) + a_2 K_1(\gamma_n \rho)] e^{-jk_n z} \hat{\rho} \\ &\quad + \gamma_n [a_1 I_0(\gamma_n \rho) - a_2 K_0(\gamma_n \rho)] e^{-jk_n z} \hat{z}\end{aligned}\tag{3.25}$$

At first glance it would appear that it is necessary to set $a_2 = 0$ in order to prevent both components of both \mathbf{A} and \mathbf{B} from diverging as $\rho \rightarrow 0$. However, doing so would make it impossible to satisfy all of the boundary conditions presented by a layered-material problem. This apparent discrepancy is resolved by noting that the material layers are varying in the $\hat{\rho}$ direction and, therefore, only one layer actually contains $\rho = 0$. Only in that layer is it necessary for $a_2 = 0$. For numerical stability, it may be required to place a constraint on the minimum thickness of the layer surrounding $\rho = 0$.

Furthermore, in order for the above MQS calculations to be valid, the materials must either be good conductors with only a $\hat{\phi}$ component to \mathbf{E} or good insulators with

only a normal component to \mathbf{E} . Another way of formulating this is to say that the magnetic diffusion time, $\tau_m = \mu\sigma l^2$, must be much greater than the charge relaxation time, $\tau_e = \epsilon/\sigma$, for any MUT with a non-zero conductivity. The conductivities for which these two quantities become equal is determined by the following equation:

$$\sigma = \frac{1}{l} \sqrt{\frac{\epsilon}{\mu}} \quad (3.26)$$

where l is a characteristic length scale such as the period of the magnetometer. Given the geometry of typical magnetometers, magnetic diffusion time is equal to charge relaxation time for conductivities on the order of .1 - 1 S/m. Therefore, the MQS approximation is valid for typical metals, which have conductivities in the mega-siemens per meter, or for good insulators with a conductivity of 10^{-12} S/m. For measurements on low conductivity materials, such as sea water, where the MQS approximation is not valid, the full set of Maxwell's equations must be considered.

3.2.2 Symmetry Considerations

To simplify the computational complexity of the semi-analytical solution to the MWM response, it is useful to exploit the symmetry of the sensor geometry. If the origin of our coordinate system is intelligently placed at the center of a primary winding as in Figure 3.2, we can make some useful observations.

First, if motion is neglected, we can note that the symmetry constrains the $\hat{\rho}$ -component of the magnetic flux density to be an odd function of z , and it constrains the \hat{z} -component to be an even function of z . This forces the exponential in the $\hat{\rho}$ term to simplify to a $\sin(k_n z)$ and the exponential in the \hat{z} term to simplify to a $\cos(k_n z)$. In terms of the magnetic vector potential \mathbf{A} , this can be formalized as

$$\left. \frac{\partial A_\phi}{\partial z} \right|_z = - \left. \frac{\partial A_\phi}{\partial z} \right|_{-z}, \quad A_\phi \Big|_z = A_\phi \Big|_{-z} \quad (3.27)$$

In order for this to be satisfied, according to Equation 3.23, \mathbf{A} must be an even function of z . More specifically, its z dependence is governed by $\cos(k_n z)$. Therefore, in a series expansion of \mathbf{A} , only non-negative wavenumber modes need be considered.

While this is convenient to use in the simplified, stationary case, this symmetry breaks down in the presence of convection. When reflected across the $\phi - \rho$ plane, velocity in the \hat{z} -direction reverses and the even symmetry is broken. Therefore, in the presence of convection, positive and negative wavenumber modes must be considered separately.

The other symmetry to note is not broken by the presence of a non-zero velocity: a half period shift in the \hat{z} direction reverses all currents, and, therefore, the sign of the magnetic vector potential. This can be formalized as

$$A_\phi \Big|_z = -A_\phi \Big|_{z+\frac{1}{2}\lambda} \quad (3.28)$$

Since this translational symmetry condition cannot be satisfied by even wavenumber modes, only odd wavenumber modes need be considered.

3.2.3 Fourier Series Expansion

The magnetic field (and, therefore, the magnetic vector potential) can be represented as a superposition of all of the different Fourier wavenumber modes. Equation 3.23 provides the closed form solution for each individual mode. Therefore, the magnetic vector potential can be expressed as

$$A_\phi(\rho, z) = \sum_{n=-\infty, odd}^{\infty} A_n(\rho) e^{-jk_n z} \quad (3.29)$$

As mentioned in the previous section, only odd wavenumber modes are required due to the translational symmetry condition in Equation 3.28.

3.2.4 Sensor Interaction with Material: Normalized Surface Reluctance Density

Now that we have established a functional form for each wavenumber mode n , it is necessary to establish how the MUT interacts with the MWM sensor. All of this information is contained within the normalized surface inductance density, which is defined as:

$$L_n(\rho, z) = k_n \frac{A_{\phi_n}(\rho, z)}{H_{z_n}(\rho, z)} \quad (3.30)$$

In order to stay consistent with implementations of related models [36]-[38] we will use the inverse of the normalized surface inductance density, which has been referred to as the normalized surface reluctance density. Even though this is a slight misnomer (as the inverse of reluctance is permeance, not inductance), there is no better term for the inverse of inductance so it will be used in this document as well. The normalized surface reluctance density is defined as:

$$R_n(\rho, z) = \frac{1}{L_n(\rho, z)} = \frac{1}{k_n} \frac{H_{z_n}(\rho, z)}{A_{\phi_n}(\rho, z)} \quad (3.31)$$

Based on Equation 3.23, we can write

$$A_{\phi_n}(\rho, z) = A_n(\rho)e^{-jk_n z} \quad (3.32)$$

where

$$A_n(\rho) = a_1 I_1(\gamma_n \rho) + a_2 K_1(\gamma_n \rho) \quad (3.33)$$

From Equation 3.25, we can write

$$H_{z_n}(\rho, z) = \frac{1}{\mu\rho} \frac{\partial(\rho A_{\phi_n})}{\partial\rho} = H_n(\rho)e^{-jk_n z} \quad (3.34)$$

where

$$H_n(\rho) = \frac{\gamma_n}{\mu} [a_1 I_0(\gamma_n \rho) - a_2 K_0(\gamma_n \rho)] \quad (3.35)$$

Therefore, plugging Equations 3.32 and 3.34 into Equation 3.31 we can conclude that

$$R_n(\rho, z) = R_n(\rho) = \frac{1}{k_n} \frac{H_n(\rho)}{A_n(\rho)} \quad (3.36)$$

It is useful to first determine how $R_n(\rho)$ behaves at the first and last material interfaces, at $\rho = \rho_0$ and $\rho = \rho_{N-1}$ respectively, as shown in Figure 3.3. In the innermost material layer which contains $\rho = 0$, it is necessary for $a_2 = 0$, as $K(\gamma_n \rho)$ diverges at $\rho = 0$. Therefore, at the innermost material interface

$$R_n(\rho_0) = \frac{\gamma_n}{\mu k_n} \frac{I_0(\gamma_n \rho_0)}{I_1(\gamma_n \rho_0)} \quad (3.37)$$

In the outermost layer which contains $\rho = \infty$, $I(\gamma_n \rho)$ diverges as $\rho \rightarrow \infty$, so we can immediately say that $a_1 = 0$. Therefore, at the outermost material interface

$$R_n(\rho_{N-1}) = -\frac{\gamma_n}{\mu k_n} \frac{K_0(\gamma_n \rho_0)}{K_1(\gamma_n \rho_0)} \quad (3.38)$$

One useful sanity check is that as ρ gets large, the cylindrical case converges to the Cartesian case, which is indeed the case [37].

$$\lim_{\rho \rightarrow \infty} R_n(\rho) = -\frac{\gamma_n}{\mu k_n} \lim_{\rho \rightarrow \infty} \frac{K_0(\rho)}{K_1(\rho)} = -\frac{\gamma_n}{\mu k_n} \quad (3.39)$$

Given a transfer function that relates $R_n(\rho_i)$ at one interface of a layer of thickness t to the interface on the other side of the layer at $R_n(\rho_{i+1}) = R_n(\rho_i + t)$, it is possible to begin at the innermost and outermost layer, apply the transfer function across each layer consecutively, and end up with an expression for the surface reluctance density on either side of the plane of the sensor, $R_n(\rho_s^+)$ and $R_n(\rho_s^-)$. The difference between

these two quantities, defined as R_n , can then be related back to the wavenumber mode of the surface current density in the plane of the windings, K_S , as follows:

$$R_n = R_n(\rho_s^+) - R_n(\rho_s^-) = \frac{1}{k_n} \frac{H_{z_n}(\rho_s^+, z) - H_{z_n}(\rho_s^-, z)}{A_{\phi_n}(\rho_s, z)} = \frac{1}{k_n} \frac{K_{S_n}}{A_n(\rho_s)} \quad (3.40)$$

where

$$K_S(z) = \sum_{n=-\infty}^{\infty} K_{S_n} e^{-jk_n z} \quad (3.41)$$

The desired transfer relation can be derived from Equation 25 in Section 2.16 of [50] which formulates the magnetic vector potential everywhere in a layer in terms of its value at the two interfaces of the layer which are at $\rho = \rho_i$ and $\rho = \rho_i + t$:

$$\begin{aligned} A_n(\rho) = & A_n(\rho_i) \frac{I_1(\gamma_n(\rho_i + t))K_1(\gamma_n\rho) - K_1(\gamma_n(\rho_i + t))I_1(\gamma_n\rho)}{I_1(\gamma_n(\rho_i + t))K_1(\gamma_n\rho_i) - K_1(\gamma_n(\rho_i + t))I_1(\gamma_n\rho_i)} \\ & - A_n(\rho_i + t) \frac{I_1(\gamma_n\rho_i)K_1(\gamma_n\rho) - K_1(\gamma_n\rho_i)I_1(\gamma_n\rho)}{I_1(\gamma_n(\rho_i + t))K_1(\gamma_n\rho_i) - K_1(\gamma_n(\rho_i + t))I_1(\gamma_n\rho_i)} \end{aligned} \quad (3.42)$$

We can see that this equation must be true as both I_1 and K_1 satisfy Equation 3.19 and it is self-consistent at the two interfaces of the layer. Using Equations 3.34, 3.36, and 3.42, we can formulate the following equations for the surface reluctance density at the two interface layers:

$$\begin{aligned} R_n(\rho_i) = & -\frac{\gamma_n}{\mu^* k_n} \frac{I_1(\gamma_n(\rho_i + t))K_0(\gamma_n\rho_i) + K_1(\gamma_n(\rho_i + t))I_0(\gamma_n\rho_i)}{I_1(\gamma_n(\rho_i + t))K_1(\gamma_n\rho_i) - K_1(\gamma_n(\rho_i + t))I_1(\gamma_n\rho_i)} \\ & + \frac{\gamma_n}{\mu^* k_n} \frac{I_1(\gamma_n\rho_i)K_0(\gamma_n\rho_i) + K_1(\gamma_n\rho_i)I_0(\gamma_n\rho_i)}{I_1(\gamma_n(\rho_i + t))K_1(\gamma_n\rho_i) - K_1(\gamma_n(\rho_i + t))I_1(\gamma_n\rho_i)} \frac{A_n(\rho_i + t)}{A_n(\rho_i)} \end{aligned} \quad (3.43)$$

$$\begin{aligned} R_n(\rho_i + t) = & -\frac{\gamma_n}{\mu^* k_n} \frac{I_1(\gamma_n(\rho_i + t))K_0(\gamma_n(\rho_i + t)) + K_1(\gamma_n(\rho_i + t))I_0(\gamma_n(\rho_i + t))}{I_1(\gamma_n(\rho_i + t))K_1(\gamma_n\rho_i) - K_1(\gamma_n(\rho_i + t))I_1(\gamma_n\rho_i)} \frac{A_n(\rho_i)}{A_n(\rho_i + t)} \\ & + \frac{\gamma_n}{\mu^* k_n} \frac{I_1(\gamma_n\rho_i)K_0(\gamma_n(\rho_i + t)) + K_1(\gamma_n\rho_i)I_0(\gamma_n(\rho_i + t))}{I_1(\gamma_n(\rho_i + t))K_1(\gamma_n\rho_i) - K_1(\gamma_n(\rho_i + t))I_1(\gamma_n\rho_i)} \end{aligned} \quad (3.44)$$

Finally, we can combine Equations 3.43 and 3.44, eliminating A_n from the expression,

leaving us with a transfer function that relates the surface reluctance density at one layer interface to the next.

$$R_n(\rho_i + t) = G_n(\rho_i + t) + F_n(\rho_i + t) \frac{G_n(\rho_i)}{R_n(\rho_i) - F_n(\rho_i)} \quad (3.45)$$

where

$$F_n(x) = -\frac{\gamma_n}{\mu^* k_n} \frac{I_1(\gamma_n(\rho_i + t))K_0(\gamma_n x) + K_1(\gamma_n(\rho_i + t))I_0(\gamma_n x)}{I_1(\gamma_n(\rho_i + t))K_1(\gamma_n \rho_i) - K_1(\gamma_n(\rho_i + t))I_1(\gamma_n \rho_i)} \quad (3.46)$$

$$G_n(x) = +\frac{\gamma_n}{\mu^* k_n} \frac{I_1(\gamma_n \rho_i)K_0(\gamma_n x) + K_1(\gamma_n \rho_i)I_0(\gamma_n x)}{I_1(\gamma_n(\rho_i + t))K_1(\gamma_n \rho_i) - K_1(\gamma_n(\rho_i + t))I_1(\gamma_n \rho_i)} \quad (3.47)$$

3.2.5 Implementation and Validation

Since the current densities in the plane of the primary windings can be considered uniform for the CUI application, as discussed in the introduction of this chapter, the magnetic field at the sense element due to a unit current excitation in the presence of the MUT can be determined using the following steps:

1. Define the current density in the primary windings based on knowledge of the sensor geometry and winding position and using the uniform current density assumption. Take the Fourier transform of the current density profile to determine the wavenumber modes of the surface current density.
2. For each wavenumber mode, start at the innermost and outermost material interface and apply the transfer functions defined in Section 3.2.4 to determine the surface reluctance density on either side of the plane of the primary windings.
3. Calculate the magnetic vector potential in the plane of the primary windings for each wavenumber mode using Equation 3.40. Convert this to the magnetic vector potential in the plane of the sense element using Equation 3.42.

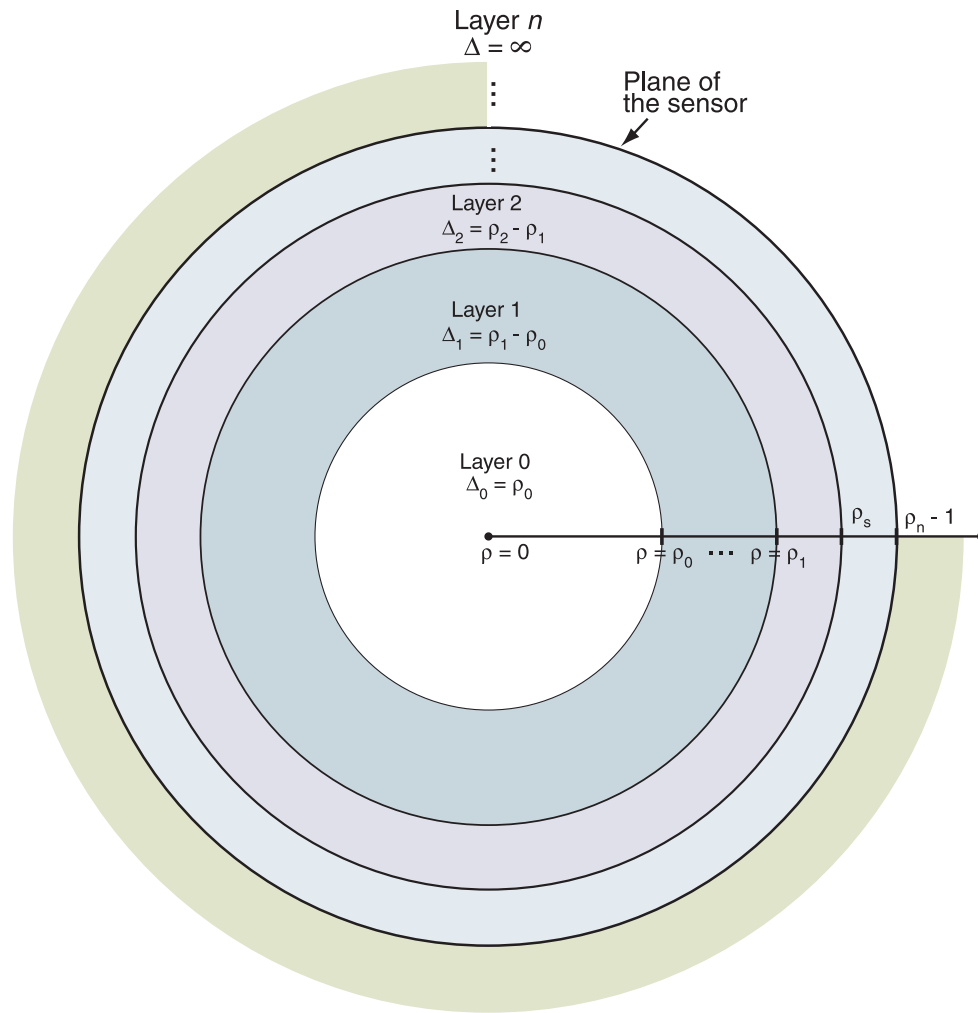


Figure 3.3: MUT cylindrical layer stackup geometry.

4. Calculate the magnetic field for each wavenumber mode at the sense element using Equation 3.25.
5. Determine the total magnetic field at the sense element due to a unit current excitation by summing the individual wavenumber modes.

While the above steps are relatively simple to implement in Matlab, care must be taken to make the simulation efficient. The two most important parameters that can be adjusted to affect the trade-off between simulation time and simulation accuracy are the simulation extent and the sampling interval. Based on the size of the sensor, a simulation extent needs to be chosen such that the model assumption that the sensor is infinitely periodic, when the sensor is actually finite, does not degrade the simulation accuracy. Furthermore, a sampling interval must be chosen that is small enough so that the drive excitation can be accurately represented, and so that high enough wavenumber modes can be calculated. As expected, as the sampling interval decreases, or as the simulation extent increases for a given sampling interval, the simulation time increases. In practice, simulation convergence is accomplished when the simulation extent is 5-10 times the size of the sensor. For the sensor geometries used for the CUI application, a sampling interval of 1 mm is necessary.

Furthermore, Bessel functions are expensive to calculate in Matlab. Much simulation time can be saved by taking into consideration the asymptotic nature of the modified Bessel function as their argument gets large [52]. It is interesting to note that this is the equivalent of using the Cartesian coordinate model for large ρ .

One of the main difficulties in validating the derived model was manufacturing an appropriate sensor. Many iterations were required before a sensor construct was created satisfying the requirements of the model. The two most difficult requirements were creating a many-turn drive winding where the location of each winding was accurately known and maintaining the sense element's position relative to the winding when the sensor is wrapped around a cylinder. Figure 3.4 shows the first sensor that

successfully matched the models. A flat wire with a 2:1 aspect ratio was used for the drive winding so that, when constructing a multiple turn winding, the position of each wire could be more easily controlled because each wire lies vertically next to the last. The flexible printed circuit board with the MR elements is potted with the drive winding such that the elements are on the same bending axis as the drive wire. Therefore, regardless of the radius of curvature, the MR elements are in the same cylindrical surface as the drive.



Figure 3.4: The first MR sensor that matched the cylindrical models. A flat wire with a 2:1 aspect ratio was used for the drive winding so that, when constructing a multiple turn winding, the position of each wire could be more easily controlled because each wire lies vertically next to the last. The flexible printed circuit board with the MR elements is potted with the drive winding such that the elements are on the same bending axis as the drive wire. Therefore, regardless of the radius of curvature, the MR elements are in the same cylindrical surface as the drive.

Figures 3.5 and 3.6 show the results that validated the cylindrical model implementation. Figure 3.5 shows that the model successfully predicts the air responses of the sensor when wrapped around plastic cylinders of varying diameters. The response of the sensor in air when flat was normalized to $1 + 0j$. Only the magnitude of the impedance response is plotted as the phase was always zero. The RMS error of the measured air responses as compared to the model-predicted air responses is under 0.05%. This is well within the tolerances of the experimental setup. Figure 3.6 shows

the results of taking measurements on a 6.625" diameter, 0.25" wall thickness pipe at varying lift-offs plotted on a lift-off / thickness grid. The air point represents the sensor's response in air when at a diameter of 10.625" (6.625" pipe + 2" of insulation). As the lift-off is increased, the data follows the lift-off line up towards the air point. As the lift-off increased from 0.5" to 2.5", the estimated thickness varied only by ± 0.002 ", with estimates ranging from 0.248" to 0.251".

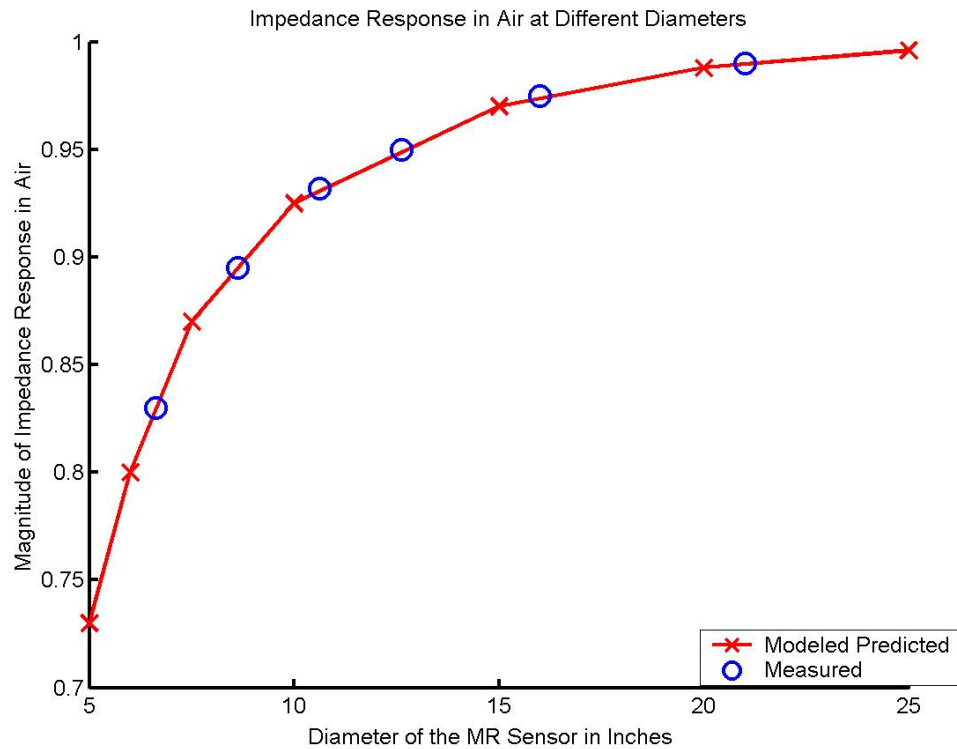


Figure 3.5: A plot of the magnitude response at 10 Hz of the MR-MWM sensor as a function of radius when wrapped around plastic cylinders. The response of the sensor in air when flat was normalized to $1 + 0j$. At all radii, as expected, the phase of the response was zero. Hence, only the magnitude of the impedance response is plotted in this figure. The RMS error of the measured air responses as compared to the model-predicted air responses is under 0.05%. This is well within the tolerances of the experimental setup.

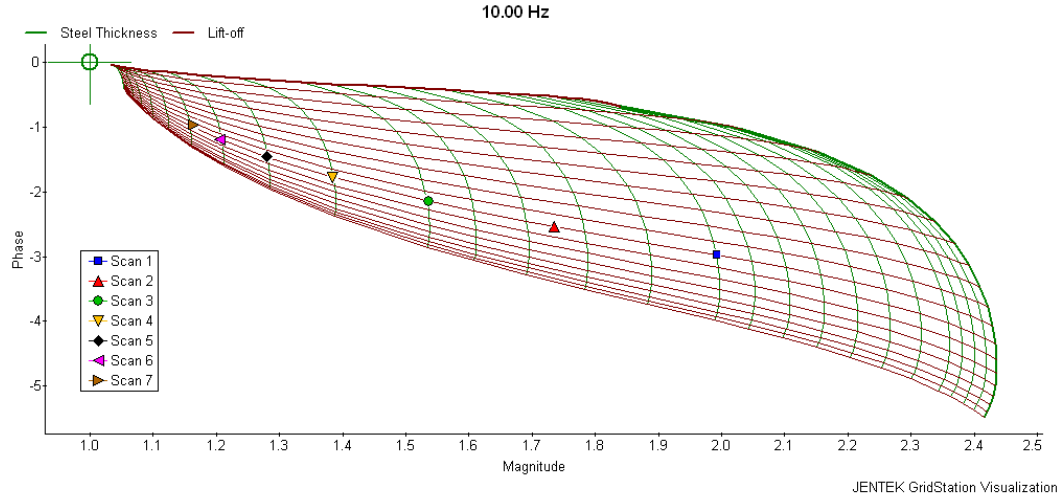


Figure 3.6: Measurement results on a 6” diameter, 0.25” wall thickness pipe at varying liftoffs plotted on a thickness-lift-off grid. As can be seen, as the lift-off is increased, the data follows the lift-off line up towards the air point. The air point represents the sensor’s response in air when at a diameter of 10.625” (6.625” pipe + 2” of insulation). As the lift-off increased from 0.5” to 2.5” the estimated thickness varied only by ± 0.002 ” with results ranging from 0.248” to 0.251”.

3.3 MWM Forward Model in Cylindrical Coordinates: Drive Aligned with z -Axis

Depending on the specifics of an application, it may be necessary to scan a pipeline circumferentially, with the drive aligned along the pipeline’s axis. This section contains the equations that predict the response of an MWM when wrapped around a pipeline in this orientation. The model assumes that the main legs of the primary winding are aligned with the axis of the pipeline and that the periodicity of the primary winding is in the circumferential direction. Secondaries are assumed to be on either side of the primary. Material properties are still assumed to be independent of z , ϕ and time and material interfaces are still assumed to be at cylindrical surfaces of constant ρ . Figure 3.7 shows the modeled MWM sensor structure.

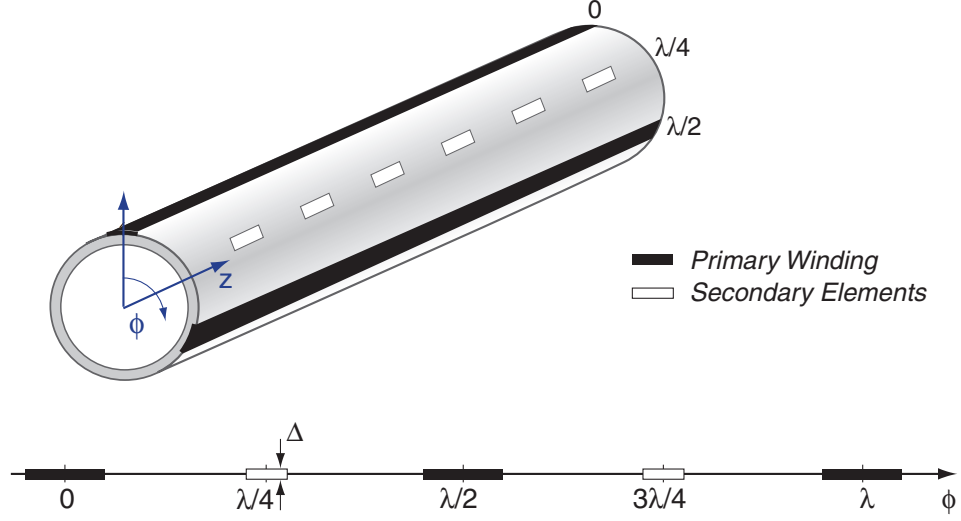


Figure 3.7: MWM geometry when wrapped around a cylindrical material with the drive aligned axially.

3.3.1 Maxwell's Equations

In this formulation, we can begin with Equation 3.13. Assuming that the sensor is periodic in the $\hat{\phi}$ direction with period λ and that the drive currents are only in the \hat{z} direction and independent of z as shown in Figure 3.7, the magnetic vector potential solution to Equation 3.13 must also only have a \hat{z} component and be independent of z . Also, since all quantities are independent of z , the \hat{z} component of the velocity can be ignored, and we need only be concerned with the $\hat{\phi}$ component (i.e. $\mathbf{v} = v_{\phi}\hat{\phi}$). Furthermore, during scanning, the material moves with a common angular velocity (i.e. $\mathbf{v} = \rho\omega_{\phi}\hat{\phi}$). So, Equation 3.13 reduces to:

$$\frac{1}{\rho} \frac{\partial}{\partial \rho} \left(\rho \frac{\partial A_z}{\partial \rho} \right) + \frac{1}{\rho^2} \frac{\partial^2 A_z}{\partial \phi^2} - j\omega\mu\sigma A_z - \mu\sigma\omega_{\phi} \frac{\partial A_z}{\partial \phi} = 0 \quad (3.48)$$

For this geometry, it is important to note that the angular periodicity in the $\hat{\phi}$ direction must be limited to integer divisors of 2π . That is, $\lambda = \frac{2\pi}{n}\rho$ where $n = 1, 2, 3, \dots$

We can use a separation of variables approach and postulate that \mathbf{A} has the form

$$\mathbf{A} = A_{z_\rho}(\rho)A_{z_\phi}(\phi)\hat{z} \quad (3.49)$$

and therefore Equation 3.48 further reduces to

$$A_{z_\phi} \left[\frac{1}{\rho} \frac{\partial}{\partial \rho} \left(\rho \frac{\partial A_{z_\rho}}{\partial \rho} \right) - j\omega\mu\sigma A_{z_\rho} \right] + A_{z_\rho} \left[\frac{1}{\rho^2} \frac{\partial^2 A_{z_\phi}}{\partial \phi^2} - \mu\sigma\omega\phi \frac{\partial A_{z_\phi}}{\partial \phi} \right] = 0 \quad (3.50)$$

Knowing the structure of the sensor's periodicity in the $\hat{\phi}$ -direction, we can say that the ϕ dependency of A_z has the form

$$A_{z_{\phi_n}}(\phi) = e^{-jn\phi} \quad (3.51)$$

Similarly to the previous derivation, the sign of the exponent here is arbitrary since positive and negative complex modes need to be treated separately because of the lack of symmetry due to the velocity term.

Plugging Equation 3.51 into Equation 3.50, we are left with the following differential equation:

$$e^{-jn\phi} \left[\frac{\partial^2 A_{z_{\rho n}}}{\partial \rho^2} + \frac{1}{\rho} \frac{\partial A_{z_{\rho n}}}{\partial \rho} + \left(\frac{-n^2}{\rho^2} - j\mu\sigma(\omega - \omega_\phi n) \right) A_{z_{\rho n}} \right] = 0 \quad (3.52)$$

Equation 3.52 is in the familiar form of the transformed Bessel function equation where $x = \rho$, $y = A_{z_\rho}$, $\alpha = 0$, $r = 1$, $f = n$ and $\beta = j\gamma'_n$, where we define the complex wavenumber, γ'_n , as

$$\gamma'_n = \sqrt{j\mu\sigma(\omega - \omega_\phi n)} \quad (3.53)$$

Therefore, the full solution for the magnetic vector potential for the general case, with drive wires aligned axially, can be written as

$$\mathbf{A}_n = [a_1 I_n(\gamma'_n \rho) + a_2 K_n(\gamma'_n \rho)] e^{-jn\phi} \hat{z} \quad (3.54)$$

The case where $\sigma = 0$ must be considered separately as the arguments of the bessel functions would be equal to zero. In this case the solution to the magnetic vector potential is much simpler

$$\mathbf{A}_n = [a_1 \rho^n + a_2 \rho^{-n}] e^{-jn\phi} \hat{z} \quad (3.55)$$

The angular velocity enters into this model in a similar manner as before. If a material is moving at angular velocity ω_ϕ relative to a sensor, then the apparent frequency of excitation ω observed in that material is replaced by $\omega - \omega_\phi n$. This again causes non-zero velocity to break the symmetry around $n = 0$ of the wavemodes, requiring that positive and negative wavemodes be treated separately. This will be discussed further in the next section.

Plugging Equation 3.54 into Equation 3.3 provides us with a formulation for \mathbf{B} .

$$\begin{aligned} \mathbf{B}_n &= \frac{1}{\rho} \frac{\partial A_{zn}}{\partial \phi} \hat{\rho} - \frac{\partial A_{zn}}{\partial \rho} \hat{\phi} \\ &= -\frac{jn}{\rho} [a_1 I_n(\gamma'_n \rho) + a_2 K_n(\gamma'_n \rho)] e^{-jn\phi} \hat{\rho} \\ &\quad - \gamma'_n [a_1 I'_n(\gamma'_n \rho) - a_2 K'_n(\gamma'_n \rho)] e^{-jn\phi} \hat{\phi} \end{aligned} \quad (3.56)$$

where

$$K'_n(\gamma'_n \rho) = \frac{K_{n-1}(\gamma'_n \rho) + K_{n+1}(\gamma'_n \rho)}{2}, \quad I'_n(\gamma'_n \rho) = \frac{I_{n-1}(\gamma'_n \rho) + I_{n+1}(\gamma'_n \rho)}{2} \quad (3.57)$$

It is necessary to set $a_2 = 0$ in the material layer that contains $\rho = 0$ in order to prevent both components of both \mathbf{A} and \mathbf{B} from diverging as $\rho \rightarrow 0$. For numerical stability, it may be required to place a constraint on the minimum thickness of the layer surrounding $\rho = 0$. For the case where $\sigma = 0$, Equation 3.55 leads to

$$\mathbf{B}_n = \frac{-jn}{\rho} [a_1\rho^n + a_2\rho^{-n}] e^{-jn\phi} \hat{z} - \frac{n}{\rho} [a_1\rho^n + a_2\rho^{-n}] e^{-jn\phi} \hat{\phi} \quad (3.58)$$

3.3.2 Symmetry Considerations

The symmetry conditions in this model that persist in the presence of convection are analogous to the previous model. A half-period shift in the $\hat{\phi}$ direction reverses all currents, and, therefore, the sign of the magnetic vector potential. This can be formalized as

$$A_z \Big|_{\phi} = -A_z \Big|_{\phi+\pi} \quad (3.59)$$

Since this rotational symmetry condition cannot be satisfied by even wavenumber modes, only odd wavenumber modes need be considered.

3.3.3 Fourier Series Expansion

The periodicity of the sensor in the $\hat{\phi}$ direction allows us to represent the magnetic field and the magnetic vector potential as a superposition of the different wavemodes. Equation 3.54 provides the closed form solution for each individual mode. The magnetic vector potential can be expressed as

$$A_z(\rho, \phi) = \sum_{n=-\infty, odd}^{\infty} A_n(\rho) e^{-jn\phi} \quad (3.60)$$

As mentioned in the previous section, only odd wavenumber modes are required due to the translational symmetry condition in Equation 3.59.

3.3.4 Sensor Interaction with Material: Normalized Surface Reluctance Density

The MUT's interaction with the MWM sensor is characterized by the surface reluctance density, now defined as

$$R_n(\rho, \phi) = \frac{1}{L_n(\rho, \phi)} = \frac{1}{k_n} \frac{H_{\phi_n}(\rho, \phi)}{A_{z_n}(\rho, \phi)} = \frac{\rho}{n} \frac{H_{\phi_n}(\rho, \phi)}{A_{z_n}(\rho, \phi)} \quad (3.61)$$

Our formulation follows the same logic as in the previous model. Based on Equation 3.54, we can write

$$A_{z_n}(\rho, \phi) = A_n(\rho)e^{-jn\phi} \quad (3.62)$$

where

$$A_n(\rho) = a_1 I_n(\gamma'_n \rho) + a_2 K_n(\gamma'_n \rho) \quad (3.63)$$

or when $\sigma = 0$,

$$A_n(\rho) = a_1 \rho^n + a_2 \rho^{-n} \quad (3.64)$$

From Equation 3.56, we can write

$$H_{\phi_n}(\rho, \phi) = -\frac{1}{\mu} \frac{\partial A_z}{\partial \rho} = H_n(\rho)e^{-jn\phi} \quad (3.65)$$

where

$$H_n(\rho) = -\frac{\gamma'_n}{\mu} [a_1 I'_n(\gamma'_n \rho) - a_2 K'_n(\gamma'_n \rho)] \quad (3.66)$$

or when $\sigma = 0$,

$$H_n(\rho) = -\frac{n}{\rho} [a_1 \rho^n - a_2 \rho^{-n}] \quad (3.67)$$

Therefore, plugging Equations 3.62 and 3.65 into Equation 3.61 we can conclude that

$$R_n(\rho, \phi) = R_n(\rho) = \frac{\rho}{n} \frac{H_n(\rho)}{A_n(\rho)} \quad (3.68)$$

It is useful to first determine how $R_n(\rho)$ behaves at the first and last material interfaces, at $\rho = \rho_0$ and $\rho = \rho_{N-1}$ respectively, as shown in Figure 3.3. In the innermost material layer which contains $\rho = 0$, it is necessary for $a_2 = 0$, as K diverges at $\rho = 0$. Therefore, at the innermost material interface

$$R_n(\rho_0) = -\frac{\rho\gamma'_n I'_n(\gamma'_n\rho_0)}{\mu n I_n(\gamma'_n\rho_0)} \quad (3.69)$$

or when $\sigma = 0$, simply

$$R_n(\rho_0) = -\frac{1}{\mu} \quad (3.70)$$

Note that in this case, R_n has the opposite sign as compared to the analogous Cartesian and circumferential-drive cylindrical cases. This is because when the roles of ρ and ϕ in the coordinate system are swapped, the right-hand rule requires that the normal component of the magnetic flux points in the opposite direction.

In the outermost layer which contains $\rho = \infty$, I diverges as $\rho \rightarrow \infty$, so we can immediately say that $a_1 = 0$. Therefore, at the outermost material interface

$$R_n(\rho_{N-1}) = \frac{\rho\gamma'_n K'_n(\gamma'_n\rho_0)}{\mu n K_n(\gamma'_n\rho_0)} \quad (3.71)$$

or when $\sigma = 0$, simply

$$R_n(\rho_{N-1}) = \frac{1}{\mu} \quad (3.72)$$

Once again we want a transfer function that relates $R_n(\rho_i)$ at one interface of a layer of thickness t to the interface on the other side of the layer at $R_n(\rho_{i+1}) = R_n(\rho_i + t)$. This would make it possible to begin at the innermost and outermost layer, apply the transfer function across each layer consecutively, and end up with an expression for the surface reluctance density on either side of the plane of the sensor, $R_n(\rho_s^+)$ and $R_n(\rho_s^-)$. The difference between these two quantities, defined as R_n , can then be related back to the wavenumber mode of the surface current density in the

plane of the windings, K_S , as follows:

$$R_n = R_n(\rho_s^+) - R_n(\rho_s^-) = \frac{\rho}{n} \frac{H_{\phi n}(\rho_s^+, \phi) - H_{\phi n}(\rho_s^-, \phi)}{A_{z_n}(\rho_s, \phi)} = \frac{\rho}{n} \frac{K_{S_n}}{A_n(\rho_s)} \quad (3.73)$$

where

$$K_S(\phi) = \sum_{n=-\infty}^{\infty} K_{S_n} e^{-jn\phi} \quad (3.74)$$

This transfer relation can be derived from the analagous equation to Equation 25 in Section 2.16 of [50] which formulates the magnetic vector potential everwhere in a layer in terms of its value at the two interfaces of the layer which are at $\rho = \rho_i$ and $\rho = \rho_i + t$:

$$A_n(\rho) = A_n(\rho_i) \frac{I_n(\gamma'_n(\rho_i + t))K_n(\gamma'_n\rho) - K_n(\gamma'_n(\rho_i + t))I_n(\gamma'_n\rho)}{I_n(\gamma'_n(\rho_i + t))K_n(\gamma'_n\rho_i) - K_n(\gamma'_n(\rho_i + t))I_n(\gamma'_n\rho_i)} - A_n(\rho_i + t) \frac{I_n(\gamma'_n\rho_i)K_n(\gamma'_n\rho) - K_n(\gamma'_n\rho_i)I_n(\gamma'_n\rho)}{I_n(\gamma'_n(\rho_i + t))K_n(\gamma'_n\rho_i) - K_n(\gamma'_n(\rho_i + t))I_n(\gamma'_n\rho_i)} \quad (3.75)$$

We can see that this equation must be true as both $I_n(\gamma'_n\rho)$ and $K_n(\gamma'_n\rho)$ satisfy Equation 3.52 and it is self-consistent at the two interfaces of the layer. Using Equations 3.65, 3.68, and 3.75, we can formulate the following equations for the surface inductance density at the two interface layers:

$$R_n(\rho_i) = \frac{\rho\gamma'_n}{\mu n} \frac{I_n(\gamma'_n(\rho_i + t))K'_n(\gamma'_n\rho_i) + K_n(\gamma'_n(\rho_i + t))I'_n(\gamma'_n\rho_i)}{I_n(\gamma'_n(\rho_i + t))K_n(\gamma'_n\rho_i) - K_n(\gamma'_n(\rho_i + t))I_n(\gamma'_n\rho_i)} - \frac{\rho\gamma'_n}{\mu n} \frac{I_n(\gamma'_n\rho_i)K'_n(\gamma'_n\rho_i) + K_n(\gamma'_n\rho_i)I'_n(\gamma'_n\rho_i)}{I_n(\gamma'_n(\rho_i + t))K_n(\gamma'_n\rho_i) - K_n(\gamma'_n(\rho_i + t))I_n(\gamma'_n\rho_i)} \frac{A_n(\rho_i + t)}{A_n(\rho_i)} \quad (3.76)$$

$$R_n(\rho_i + t) = \frac{\rho\gamma'_n}{\mu n} \frac{I_n(\gamma'_n(\rho_i + t))K'_n(\gamma'_n(\rho_i + t)) + K_n(\gamma'_n(\rho_i + t))I'_n(\gamma'_n(\rho_i + t))}{I_n(\gamma'_n(\rho_i + t))K_n(\gamma'_n\rho_i) - K_n(\gamma'_n(\rho_i + t))I_n(\gamma'_n\rho_i)} \frac{A_n(\rho_i)}{A_n(\rho_i + t)} - \frac{\rho\gamma'_n}{\mu n} \frac{I_n(\gamma'_n\rho_i)K'_n(\gamma'_n(\rho_i + t)) + K_n(\gamma'_n\rho_i)I'_n(\gamma'_n(\rho_i + t))}{I_n(\gamma'_n(\rho_i + t))K_n(\gamma'_n\rho_i) - K_n(\gamma'_n(\rho_i + t))I_n(\gamma'_n\rho_i)} \quad (3.77)$$

Finally, we can combine Equations 3.76 and 3.77, eliminating A_n from the expression,

leaving us with a transfer function that relates the surface reluctance density at one layer's interface to the next.

$$R_n(\rho_i + t) = G_n(\rho_i + t) + F_n(\rho_i + t) \frac{G_n(\rho_i)}{R_n(\rho_i) - F_n(\rho_i)} \quad (3.78)$$

where

$$F_n(x) = \frac{x\gamma'_n I_n(\gamma'_n(\rho_i + t))K'_n(\gamma'_n x) + K_n(\gamma'_n(\rho_i + t))I'_n(\gamma'_n x)}{\mu^* n I_n(\gamma'_n(\rho_i + t))K_n(\gamma'_n \rho_i) - K_n(\gamma'_n(\rho_i + t))I_n(\gamma'_n \rho_i)} \quad (3.79)$$

$$G_n(x) = -\frac{x\gamma'_n I_n(\gamma'_n \rho_i)K'_n(\gamma'_n x) + K_n(\gamma'_n \rho_i)I'_n(\gamma'_n x)}{\mu^* n I_n(\gamma'_n(\rho_i + t))K_n(\gamma'_n \rho_i) - K_n(\gamma'_n(\rho_i + t))I_n(\gamma'_n \rho_i)} \quad (3.80)$$

For the case when $\sigma = 0$,

$$R_n(\rho_i + t) = \frac{1}{\mu} \frac{1 - \mu R_n(\rho_i) F_n(\frac{\rho_i + t}{\rho_i})}{\mu R_n(\rho_i) - F_n(\frac{\rho_i + t}{\rho_i})} \quad (3.81)$$

where

$$F_n(x) = \frac{x^n + x^{-n}}{x^n - x^{-n}} \quad (3.82)$$

3.3.5 Implementation and Validation

The implementation procedure for this model parallels the previous model:

1. Define the current density in the primary windings based on knowledge of the sensor geometry and winding position and using the uniform current density assumption discussed in the introduction of this chapter. Take the Fourier transform of the current density profile to determine the wavenumber modes of the surface current density.
2. For each wavemode, start at the innermost and outermost material interface and apply the transfer functions defined in Section 3.3.4 to determine the surface reluctance density on either side of the plane of the primary windings.

3. Calculate the magnetic vector potential in the plane of the primary windings for each wavenumber mode using Equation 3.73. Convert this to the magnetic vector potential in the plane of the sense element using Equation 3.75.
4. Calculate the magnetic field for each wavemode at the sense element using Equation 3.56.
5. Sum the magnetic fields due to each wavemode to determine the total magnetic field at the sense element due to a unit current excitation.

Since the procedure and equations are similar, the numerical implementation in Matlab has many of the same issues. Because of some of the extra terms in Equations 3.56, 3.75, 3.79 and 3.80, the efficient treatment of the Bessel functions is extra important. Taking into consideration the asymptotic nature of the modified Bessel function as their argument gets large [52] saves much simulation time. This is the equivalent of using the Cartesian coordinate model for large ρ .

The sensor shown in Figure 3.4 was used to validate this model. Because no scanner was available to validate that the required symmetries were maintained after the sensor was wrapped around a pipe in this orientation, much care had to be taken to assure that the sensor's geometry matched the assumptions of the model. Specifically, care had to be taken to make sure that the sense elements remain in the same cylindrical plane as the drive wires when wrapped around the pipe.

A similar measurement procedure was used to validate this model. Figures 3.8 and 3.9 show the results that validated the cylindrical model implementation. Figure 3.8 shows that the model successfully predicts the air responses of the sensor when wrapped around plastic cylinders of varying diameters. The response of the sensor in air when flat (before wrapping around the plastic cylinders) was normalized to $1 + 0j$. Only the magnitude of the impedance response is plotted as the phase was always zero. The RMS error of the measured air responses as compared to the model-predicted air

responses is under 0.14%, which is within the tolerances of the experimental setup. Figure 3.9 shows the results of taking measurements on a 6.625" diameter, 0.25" wall thickness pipe at varying lift-offs plotted on a lift-off / thickness grid. The air point represents the sensor's response in air when at a diameter of 10.625" (6.625" pipe + 2" of insulation). The data follows the lift-off line up towards the air point. As the lift-off increased from 0.5" to 2.5", the estimated thickness varied only by ± 0.004 ", with estimates ranging from 0.247" to 0.254".

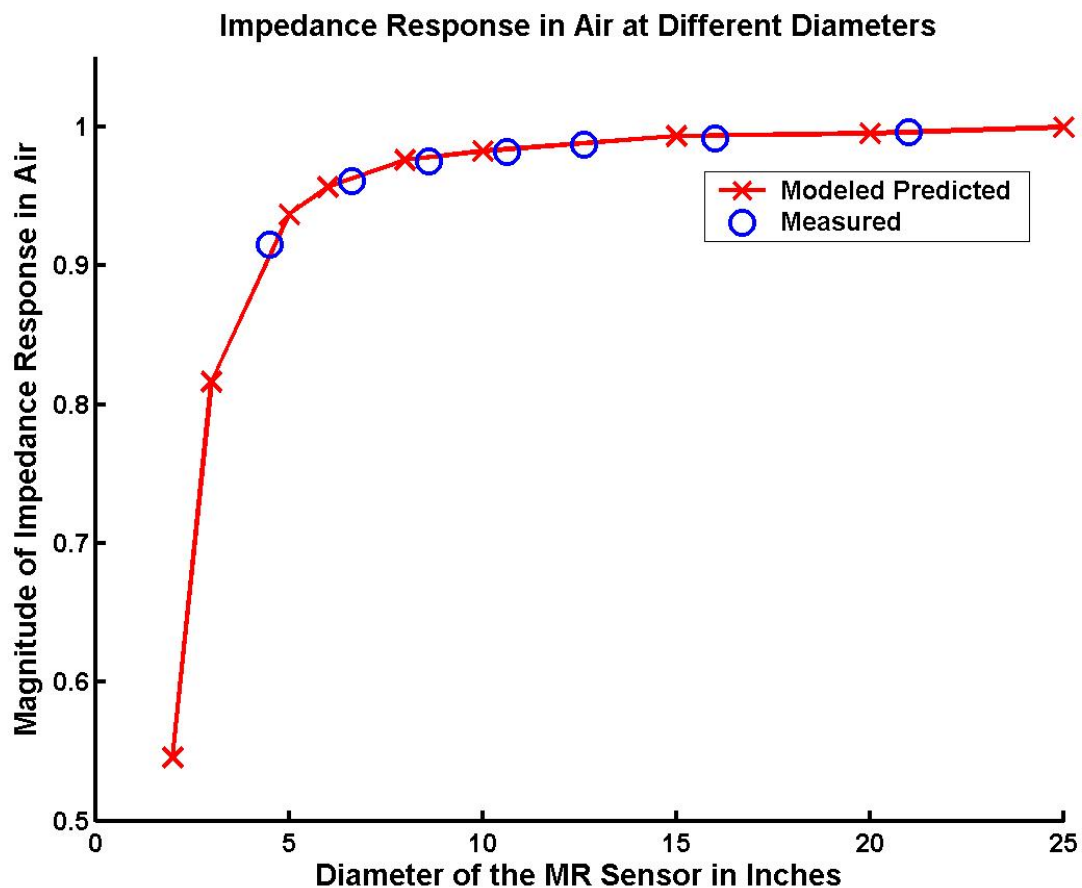


Figure 3.8: A plot of the magnitude response at 10 Hz of the MR-MWM sensor as a function of radius when wrapped around plastic cylinders. The response of the sensor in air when flat (before wrapping around the plastic cylinders) was normalized to $1 + 0j$. At all radii, as expected, the phase of the response was zero. Hence, only the magnitude of the impedance response is plotted in this figure. The RMS error of the measured air responses as compared to the model-predicted air responses is under 0.14%. This is well within the tolerances of the experimental setup.

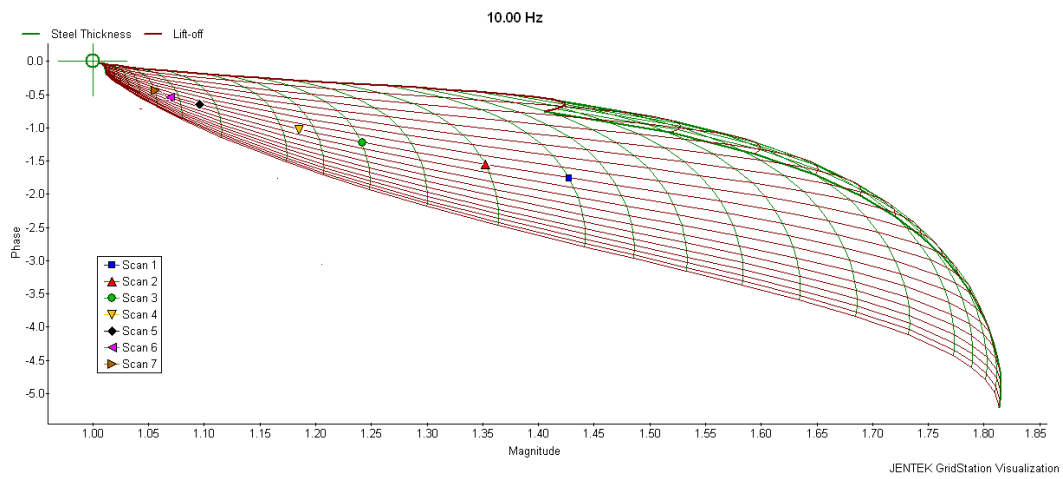


Figure 3.9: Measurement results on a 6” diameter, 0.25” wall thickness pipe at varying liftoffs plotted on a thickness-liftoff grid. As can be seen, as the lift-off is increased, the data follows the lift-off line up towards the air point. The air point represents the sensor’s response in air when at a diameter of 10.625” (6.625” pipe + 2” of insulation). As the lift-off increased from 0.5” to 2.5” the estimated thickness varied only by ± 0.004 ” with results ranging from 0.247” to 0.254”.

CHAPTER 4

SENSOR FOOTPRINT ANALYSIS

With an MR-MWM-Array that achieves the required SNR in order to resolve steel thicknesses up to 0.5", to an accuracy of within 0.005", through 2 inches of insulation, and a model that allows the measurements to be correctly interpreted in a cylindrical coordinate system, it would seem that all of the pieces were in place to solve the target problem. However, the issue of detecting localized defects had not been addressed.

After testing the sensor pictured in Figure 3.4 on flat steel plates with manufactured defects at 2" of lift-off, it became immediately obvious that there was still a large problem to solve. Figure 4.1 displays the result that motivated the following model derivation.

The flat plate that was scanned had a 0.150" deep, 3" diameter defect etched into a 0.250" inch steel plate. The sensor that was used had a single rectangular drive whose conductors were 4.5" apart, center-center. The sense elements were 1.5" away from one of the conductors. This type of drive construct is very common in applications for MWM-Arrays, and it seemed like a reasonable place to start.

The dark circle represents the expected location of the response when the sense element array was centered over the flaw. Instead, the single uniform flaw created two responses, the largest of which was only 0.025" deep, considerably less than the 0.150" flaw depth. Based on the spacing of the two responses, it seems that the two peaks occurred when each of the drive conductors were centered over the flaw. Overall, the result showed that the reported size and depth were not representative

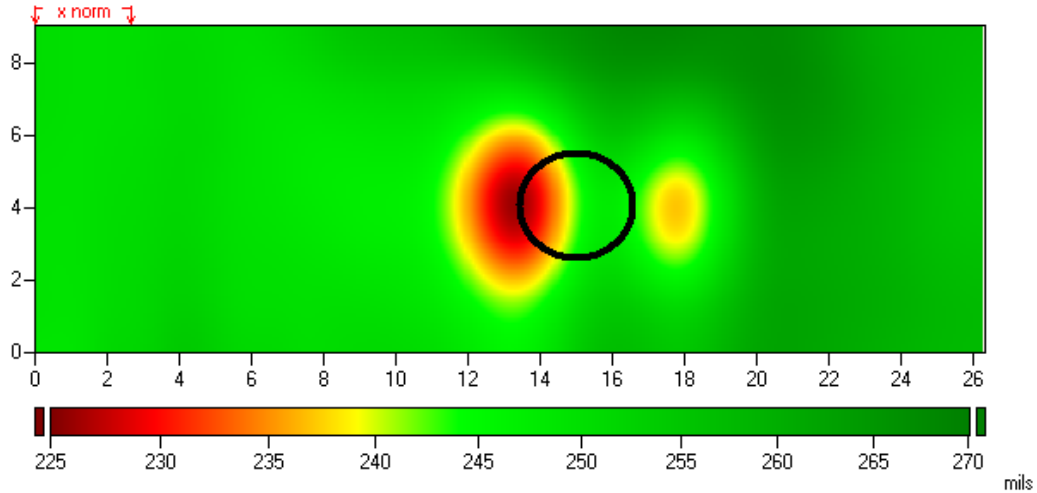


Figure 4.1: Scan over 0.25” flat steel plate with a 0.150” deep, 3” diameter defect at 2” of lift-off using the MR-MWM-Array pictured in Figure 3.4. The dark circle represents the expected location of the response when the sense element array was centered over the flaw. There were two peaks to the response, the largest of which recorded a thickness change of 0.025”.

of the defect, and that general sensitivity to local defects was low.

Conjecturing that the sensor’s flaw response is a function of the volume of a flaw, if this flaw provided a 0.025” response, then we could extrapolate that the desired 0.050” deep, 2” diameter defect would only provide a 0.0037” response. While this may be at the very edge of the sensor’s capability, it was clear that designing a sensor with a larger sensitivity to local defects was required to reliably achieve the required specifications.

Based on this observation, it was hypothesized that the flaw response could be resolved into a single peak with a larger magnitude by using a single drive wire that wrapped around the entire circumference of the pipeline (taking advantage of the cylindrical geometry of the target application). This was a promising idea which turned out to be very difficult to manufacture because of the requirement to solder the 80 individual wires in a specified pattern at the seam. A prototype was built, and it is displayed in Figure 4.2.



Figure 4.2: Initial prototype for a drive construct where the drive is made of a single conductor that wraps around the entire circumference of the pipeline. This design was intended to reduce the footprint demonstrated by the sensor pictured in Figure 3.4, but actually had the opposite effect.

Unfortunately the prototype was a failure. While the response did not display two distinct peaks like the response of initial prototype sensor, it seemed that the response was much wider than expected and of a much lower magnitude. And, it seemed that the sensor was much more sensitive to the ends of the pipe, over a much larger distance. This result makes sense if we think of the sensor as providing an average thickness response over its sensor “footprint.” By moving from the single rectangular sensor with two conductors, to a single conductor wrapped around the circumference of the pipe, we made the sensor footprint much larger. This was the opposite of the desired effect.

Therefore, it was clear that a model was needed to predict the footprint of a sensor given different drive constructs. This chapter describes a few of the implemented models, discusses their relative successes and shortcomings, and shows how the models helped to design a much more effective MR-MWM-Array for the CUI application.

4.1 1-D Perfect Electrical Conductor (PEC) Footprint Model

In order to get some rough intuition of the footprint effect, a very simple 1-D model was developed. The assumptions were as follows:

1. The MUT is a perfect electrical conductor (PEC), with $\sigma = \infty$.
2. The drive conductors are infinitely long and infinitely thin wires parallel to the MUT at a height h from the MUT.
3. The sense element is in the same plane as the drive conductors, also at a height h and considered to be infinitely long in the direction parallel to the drive.

Figure 4.3 (left) shows the analyzed structure for the case of a single drive wire. The advantages of these assumptions are immediately evident. The magnetic fields due to infinitely long wires above a PEC are easily calculated using image theory. And the principle of superposition can be used to calculate the field for each drive wire independently with the entire sensor's response being the sum of the responses for the individual drive wires.

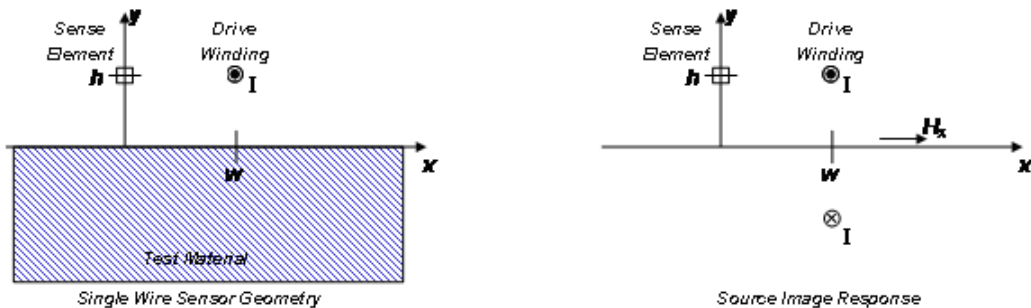


Figure 4.3: . (Left) Model geometry for one wire of the drive winding over the test material. (Right) Image source geometry used to estimate the field at the surface of the test material.

The following analysis provides a first-order approximate representation of the sensor response to the MUT as a function of position on the material. Assuming the

MUT is a PEC ignores magnetic diffusion and frequency related effects; assuming that the drive is constructed of infinitely thin line currents ignores the effect of winding thickness. Furthermore, since everything is considered infinite in the direction of the drive conductors, this formulation only analyzes the footprint in the direction orthogonal to the drive conductors. Despite being so simplified, this model was very predictive of a given sensor-geometry's response to localized defects and was a good first iteration for developing intuition on a given sensor-geometry's measurement footprint.

There are two analysis steps associated with this model. The first step is a calculation of the nominal current distribution flowing along the surface of the test material. The second step is to relate the local surface current density to the field that would be generated in the vicinity of a sense element. This is used to determine the sense element response to a local feature (i.e., material loss that leads to a reduction in the surface current) anywhere in the vicinity of the drive winding and provides the sensor response footprint.

The basic geometry for a single wire is shown in Figure 4.3 (left). It is assumed that the drive winding carries a current I out of the page (in the \hat{z} direction) and is located at an x position of w and a y position of h . The sense element is also located at a height h above the surface of the test material.

Assuming that the test material is a PEC, the test material can be replaced with an image current source (this is equivalent to assuming that the excitation frequency is relatively high compared to the eddy current skin depth in the test material). This allows the magnetic field above the test material to be determined, which, in turn, allows the induced eddy current surface distribution in the test material to be determined. Using the equivalent source geometry of Figure 4.3 (right), the magnetic field intensity just above the surface of the test material can be obtained from the

Biot-Savart law as

$$\mathbf{H}(x) = \frac{I}{\pi} \frac{h}{h^2 + (x - w)^2} \hat{x} \quad (4.1)$$

The current flowing through the surface of the test material is then determined from the boundary condition that requires the tangential component of the field intensity H_x to be zero inside the test material. This surface current density can be expressed as

$$\mathbf{K}(x) = \hat{y} \times H_x \hat{x} = -\frac{I}{\pi} \frac{h}{h^2 + (x - w)^2} \hat{z} \quad (4.2)$$

The second step is to project this local current density back to the location of the sense element so that the field that would be measured by the sense element can be determined. In air, without a test material present, the field intensity in the vicinity of the sense element is

$$\mathbf{H}_{air}(x) = -\frac{I}{2\pi w} \hat{y} \quad (4.3)$$

This field is perturbed from the air response by the presence of the test material. Using the same Biot-Savart law given above, the perturbation in the field around the sense element due to the induced surface current is

$$d\mathbf{H}(x) = \frac{I\Delta x}{2\pi^2} \left[\frac{h}{h^2 + (x - w)^2} \right] \left[\frac{-h\hat{x} + x\hat{y}}{h^2 + x^2} \right] \quad (4.4)$$

where Δx is the incremental spacing in the \hat{x} direction. The first term in brackets comes from the imposed field while the second term comes from the projection of the surface current back to the sense element. This formulation provides both components of the magnetic field at the sense element. In general, the MR-MWM-Array is only sensitive to the normal component (\hat{y} component) of the magnetic field. This is because there is no tangential component of the field when measuring in air, which makes an air calibration of this component impossible.

Calculating the footprints of the single loop drive pictured in Figure 4.2 and the rectangular drive pictured in Figure 3.4 demonstrates the validity of this approach. These footprints are very representative of the measurements taken and are shown in Figure 4.4. The footprints are normalized by the area under the footprint curve to show the relative sensitivity to the material as a function of position. Despite the simplicity of the analysis, the footprint of the rectangular drive predicts the two response peaks at 4.5" apart. Furthermore the footprint model predicts a wider, single peak for the single loop drive.

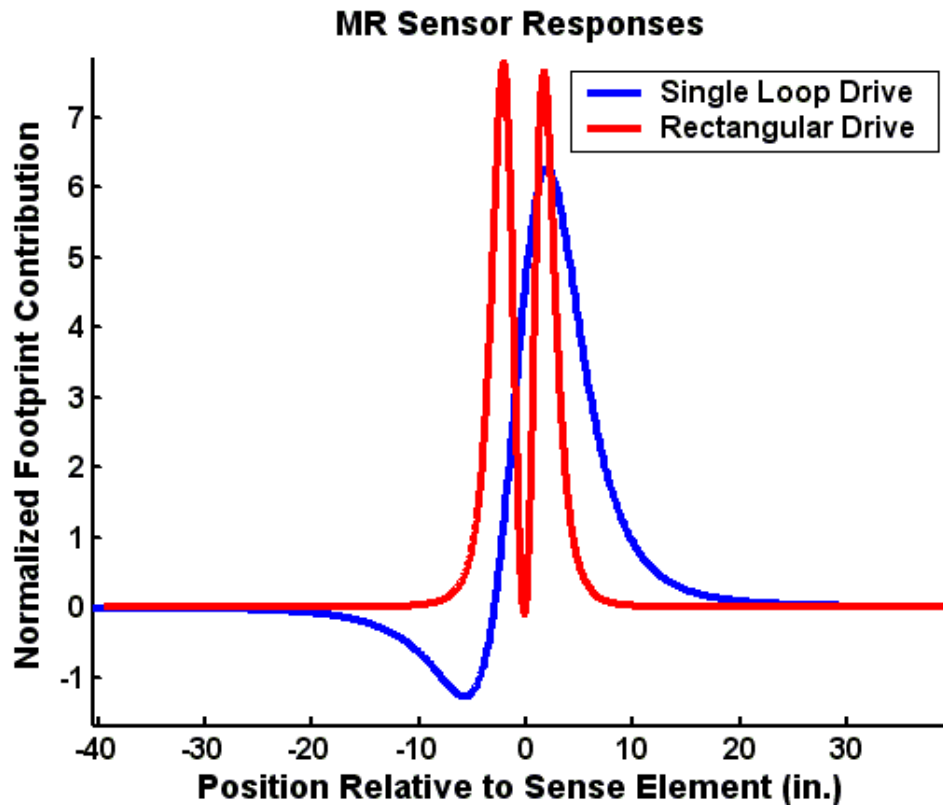


Figure 4.4: The calculated footprints of the single loop drive pictured in Figure 4.2 (blue) and the rectangular drive pictured in Figure 3.4 (red) as predicted by the 1-D PEC footprint model.

Because of the initial success of the 1-D PEC analysis, the model was extended to take into consideration the finite length of the drive and sense elements as well as drive wires of finite thickness. This results in a calculation of a 2-D PEC footprint

which can be used to provide initial predictions in sensor sensitivity. This model is derived in the following section.

4.2 2-D PEC Footprint Model

The basic approach for the 2-D PEC footprint model is the same as the 1-D PEC footprint model: first determine the current density induced on the surface of the PEC and then reflect that back to the magnetic field at the location of the sense element. The main difference is that instead of an infinitely long and thin current wire over the PEC, we have a discrete current volume, representing a finite wire with width and length.

This problem can be formulated conveniently by the “current stick model” [50]. The geometry for this model is shown in Figure 4.5. The model uses the Biot-Savart law to derive:

$$\mathbf{H}(\mathbf{r}) = \frac{j}{4\pi} \frac{\mathbf{c} \times \mathbf{a}}{|\mathbf{c} \times \mathbf{a}|^2} \left(\frac{\mathbf{a} \cdot \mathbf{c}}{|\mathbf{c}|} - \frac{\mathbf{a} \cdot \mathbf{b}}{|\mathbf{c}|} \right) \quad (4.5)$$

The current volume can then be approximated as an integral, or more conveniently implemented in Matlab as a Riemann-Sum, where each sub-volume’s current is considered to be concentrated in a current-stick at the sub-volume’s center. Therefore, as in the 1-D case, we can then use image theory to calculate the induced surface current density on the surface of the PEC and reflect it back to the magnetic field at the sense element. The result is a two-dimensional representation of the sensor footprint.

Figure 4.6 shows the 2-D PEC model footprint for the sensor pictured in Figure 3.4. Figure 4.7 then shows the result when the footprint is convolved with a flaw representative of the one scanned in Figure 4.1. The results are very encouraging. The 2-D footprint model captures the double peak shape of the response as well as the first peak being slightly larger than the second. The relative position of the two

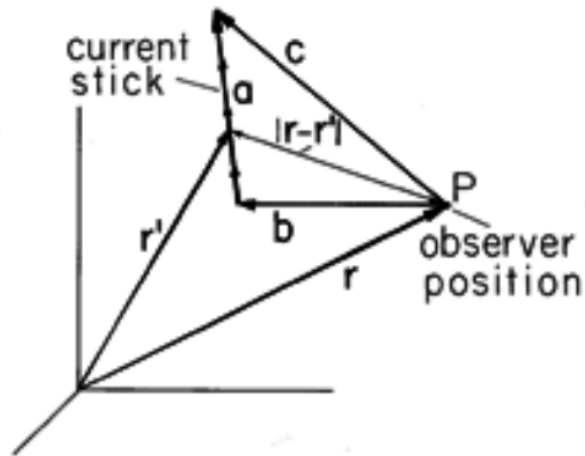


Figure 4.5: Geometry for the “current stick” model, figure taken from Chapter 8, Section 8.2 of [50].

peaks is also accurate: the spacing between them is approximately 4.5”, which is the distance between the center of the two legs of the drive. Also, the larger of the two responses corresponds to when the drive leg that is closer to the sense element passes over the flaw for both the model and the measurements. And finally, the footprint model accurately predicts the large blurring in the direction parallel to the drive.

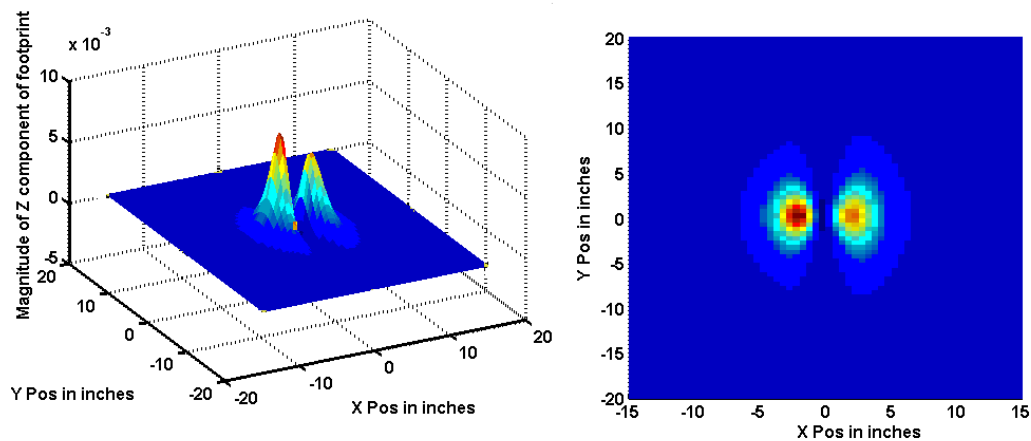


Figure 4.6: Computed footprint based on the 2-D PEC model for the single-rectangular drive sensor pictured in Figure 3.4. The contour plot on the left is equivalent to the c-scan representation on the right.

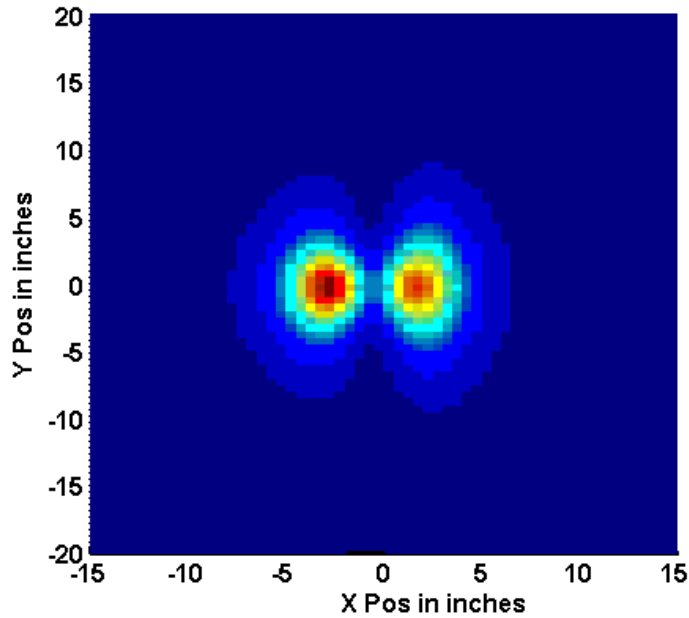


Figure 4.7: Result of the convolution of the 2-D PEC footprint represented in Figure 4.6 with a 3 inch diameter, 0.150" deep defect. The maximum response (dark red) is 0.030" .

There are two shortcomings of the 2-D PEC model. The first problem is that the predicted size of the response is approximately 20% high - the model predicts a maximal sensor response of 0.030", when the sensor response is actually only 0.025". This bias in predicted size holds for other flaw sizes as well.

The second shortcoming is more serious. The PEC footprint model provides only a magnitude response (as there is no phase information from a PEC) and, therefore, expects all perturbations to behave similarly. This assumption is not valid. When looking at a near side flaw, the thickness response and the lift-off response are not equivalent. The thickness response seems to be centered around the location of the drive conductors while the lift-off response seems to be more centered around the location of the sense element.

It is likely that this behavior is not captured because the PEC model ignores diffusion. A footprint model that relaxes the PEC requirement to capture frequency

dependent and material dependent diffusion effects will be discussed in the next section. This model will also be appropriate for cylindrical coordinates.

4.3 Cylindrical Coordinate Footprint Model Incorporating Diffusion Effects

In order to create a footprint model that takes into consideration frequency and material properties and the associated diffusion effects, we need to determine a method for figuring out the current density in the MUT. When the MUT is not a PEC, the method of image currents is not available to us.

This can be accomplished with a clever application of the Love's Field Equivalence Principle [53]. The procedure for calculating the footprint is as follows:

1. Use the cylindrical coordinate model developed in Chapter 3 to determine the magnetic field everywhere in the presence of the MUT.
2. Use the cylindrical coordinate model developed in Chapter 3 to determine the magnetic field everywhere in air (in the absence of a MUT).
3. Subtract the air response from the total response to use the Superposition Principle, and determine the field everywhere due to the induced eddy currents in the material.
4. Use Love's Field Equivalence Principle, described by the geometry in Figure 4.8, to represent the unknown induced eddy currents in the MUT as a surface current around free space.
5. Reflect that surface current back to the sense element to determine the impedance response footprint of the sensor.

There are a few things to discuss about the assumptions of this model. First, while it does handle the layered media model, it only approximates the footprint at

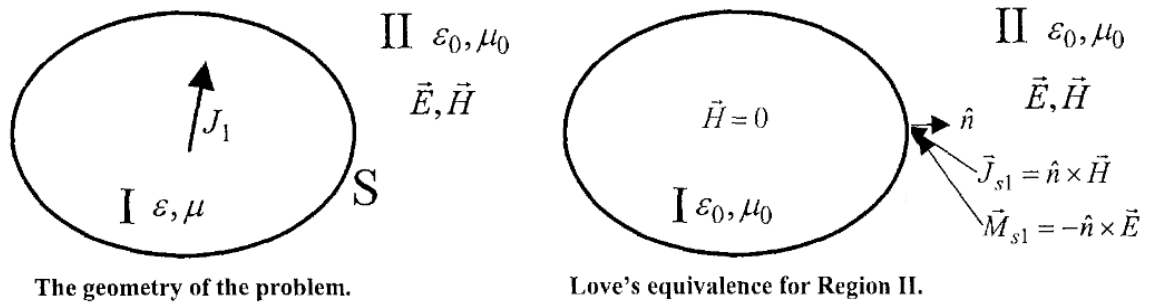


Figure 4.8: Illustration of the application of the Love's Field Equivalence Principle. If the magnetic field is known everywhere in Region II due to current sources in Region I (left), then this can be replaced with a surface current density around an equivalent Region I of free space (right).

the surface of the outermost layer. For the case of CUI, one could argue that this is not appropriate as the outermost layer is the weatherjacket. However, as discussed in Chapter 2, the presence of the weatherjacket only provides a phase shift at the low frequencies that are sensitive to the thickness of steel. The weatherjacket does not change the relative sensitivity level. So, ignoring its presence for the case of the footprint analysis is not a bad assumption.

Secondly, converting the footprint information into an expected flaw response is more complicated than in the PEC model. In the PEC model, since only a magnitude footprint was calculated, this was convolved with a flaw response that was represented as a thickness change. Now, the footprint convolution must be done in impedance space and then converted back into properties of interest. This allows for a separate footprint for each measured property.

The magnitude and phase footprint of the sensor pictured in Figure 3.4 at 10 Hz is shown in Figure 4.9 for the flat plate configuration. The phase footprint is very similar to the footprint calculated by the PEC model, as expected: the thickness response at 10 Hz is mostly in phase, and the PEC model was predictive of the sensor's thickness response. The phase footprint is slightly wider than the PEC calculated footprint causing the predicted thickness response to the flaw scanned in Figure 4.1 to drop

from 0.030" predicted by the PEC model to 0.024". Therefore, incorporating diffusion into the model eliminated the upward bias in predicted thickness response discussed in the previous section.

Furthermore, the magnitude of the footprint response is centered under the sense element and only has a single peak. This corresponds to the lift-off response of the sensor, resolving the second shortcoming of the 2-D PEC model discussed in the previous section.

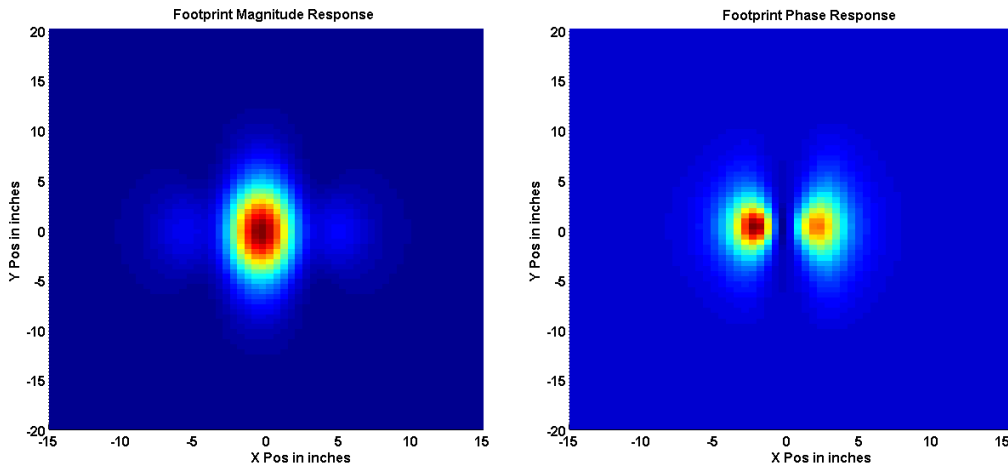


Figure 4.9: The magnitude and phase footprint of the sensor pictured in Figure 3.4 at 10 Hz for the flat plate configuration. The phase footprint (right) is very similar to the footprint calculated by the PEC model. The magnitude footprint only has a single peak that is centered around the sense element.

4.4 Sensor Design Optimization

As discussed in the introduction to this chapter, the main motivation for developing the footprint models was to gain intuition as to how changes in the sensor geometry affected the sensor's sensitivity to local defects. The desired ideal footprint would be a 2-D delta function: this would cause each measurement to be a perfect sample of the material directly under the sensor.

The MWM structure provides very little flexibility towards changing the footprint in the direction parallel to the drive conductors. However, the placement of the conductors allows for the manipulation of the footprint perpendicular to the drive conductors. After trying many different drive configurations, the design converged on a double rectangular drive structure with the sense elements centered in one of the rectangles. The width of the rectangle was chosen to be 3.5" in order to achieve a similar sensitivity to steel thickness as the single rectangular sensor used in previous measurements. Figure 4.10 shows the improvement of the sensor footprint. The main peak of the double rectangular footprint is over twice as tall as the taller peak of the single rectangular footprint, which indicates improved sensitivity to local perturbations.

It should be noted that while a large, narrow peak for the sensor footprint is desired, it should not be achieved at the cost of creating a differential sensor. In other words, the integral of the sensor footprint must not be close to zero. If this were the case, calibration in air would be impossible.

The double rectangular sensor has other desirable characteristics. First, there is only one side lobe on either side of the main lobe, and the lobes decay to zero quickly as compared to other designs. Another thing to notice is that the side lobes are anti-symmetric. That is, moving the sense elements into the other drive rectangle causes the side lobes to flip. By creating a sense element that is the combination of two sense elements, one in either rectangle, we are left with an even more ideal footprint. This is shown in Figure 4.11. The combined sense element sensor has the advantage of the large peak without the large side lobes.

The benefit of having the side lobes cancel is very significant. In addition to eliminating secondary peaks in the response as seen with the single rectangular sensor, the combined sense element sensor also greatly reduces unmodeled behavior. The model assumes that the MUT is a uniformly layered material: under this assumption

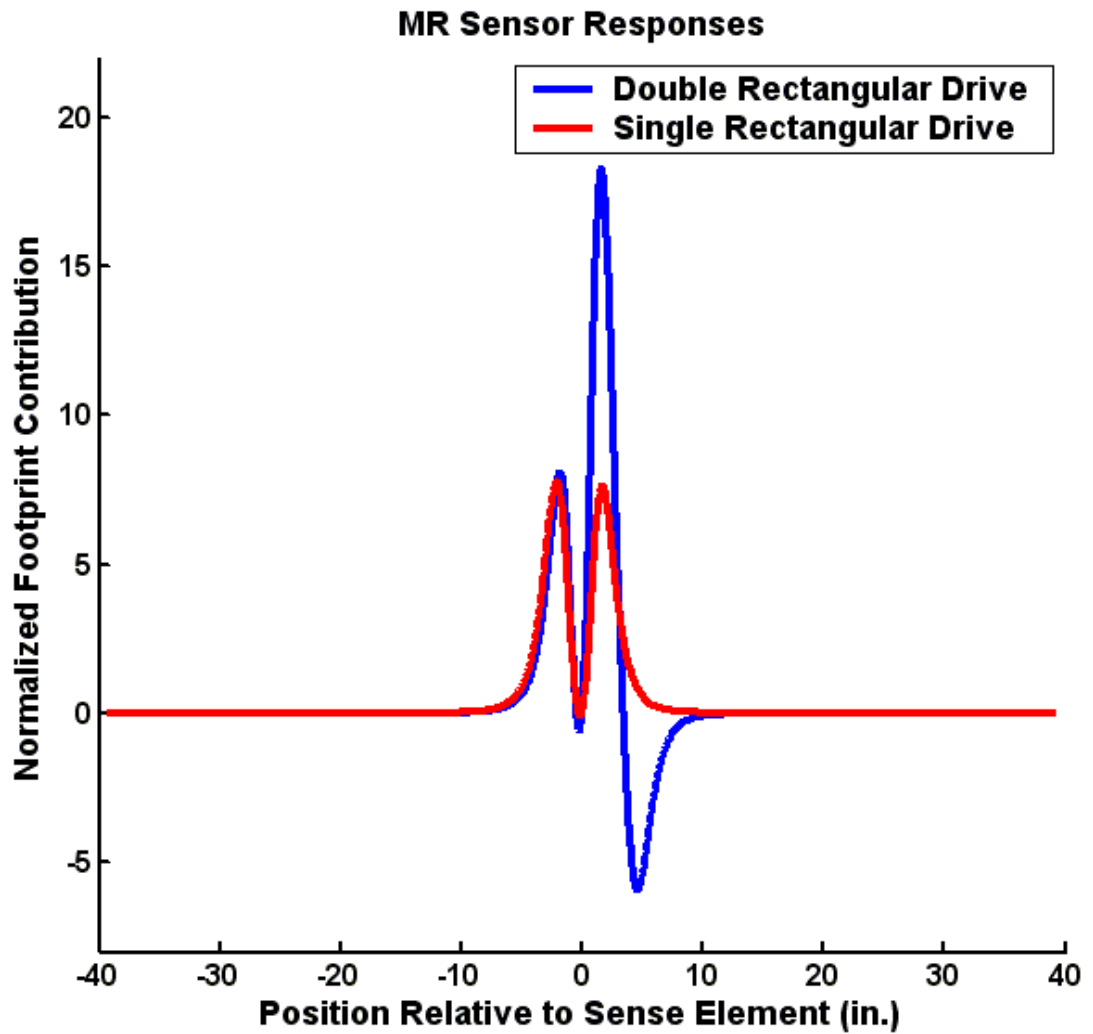


Figure 4.10: Comparison of the double rectangular sensor footprint to the single rectangular sensor footprint. The main peak of the double rectangular footprint is over twice as tall as the taller peak of the single rectangular footprint indicating improved sensitivity to local perturbations.

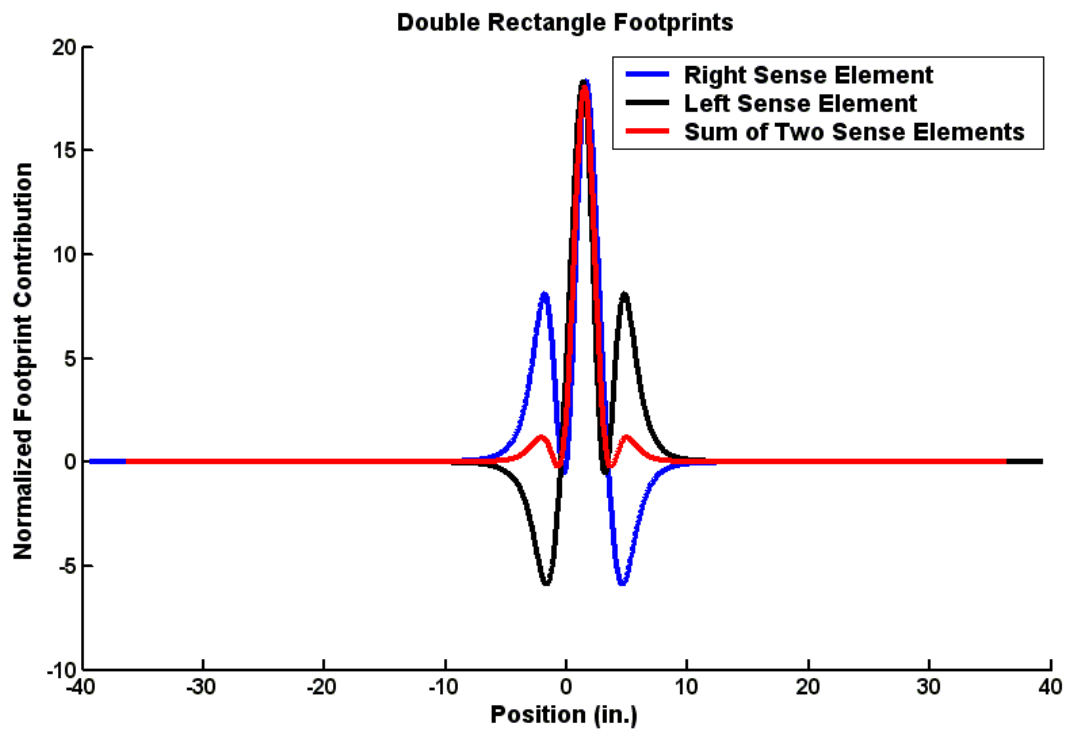


Figure 4.11: Sensor footprints for sense elements in either rectangle of the double rectangular sensor, and the footprint resulting from combining the sense elements.

the side lobes would cancel. Using a single sense element requires material on one side of the sensor to cancel with material on the other side of the sensor. If the material is varying, this does not happen, and the property estimates would be corrupted by the unmodeled behavior. However, combining the two sense elements cancels out the side lobes using the same material twice. Therefore, even if the material is varying from one side of the sensor to the other, the measurements will more closely adhere to the model.

Figure 4.12 shows the flexible double row, double rectangular MR-MWM-Array. The drive is not visible because it was potted in an opaque polyurethane. Figure 4.13 shows the improvement in response when scanning this sensor over the same 0.25" flat plate with a 0.150" deep, 3" diameter defect at 2" of lift-off scanned in Figure 4.1. The signal shape is much more representative and the response is 0.041" as compared to the previous response of 0.025". The improvement provides the required SNR to detect the target 2 inch diameter, 0.050" flaw.



Figure 4.12: The flexible, double row, double rectangle MR-MWM-Array.

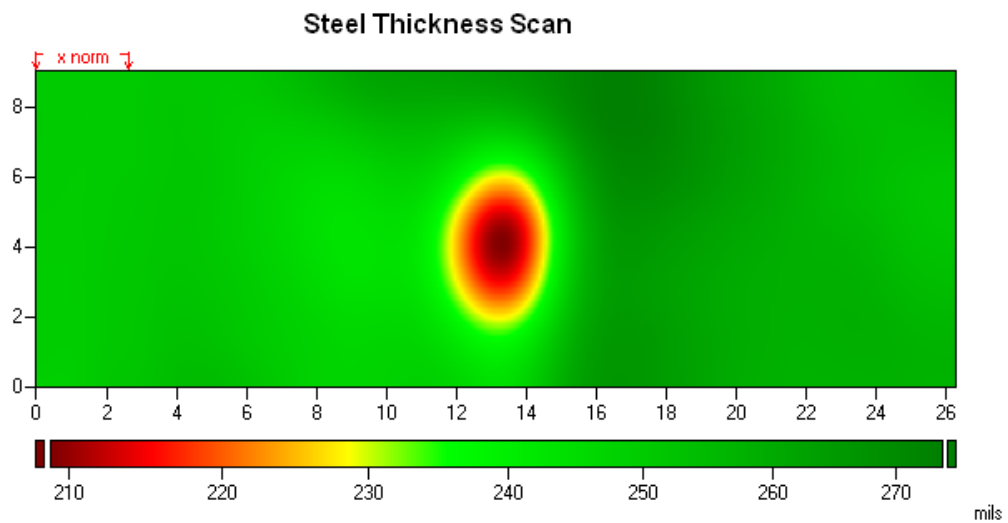


Figure 4.13: Scan over 0.25” flat plate with a 0.150” deep, 3” diameter defect at 2” of lift-off using the MR-MWM-Array pictured in Figure 4.12. With this sensor, the signal shape is much more representative and the response is 0.041” as compared to the previous response of 0.025”.

CHAPTER 5

FLAW SIZING

The previous chapter concluded with a sensor design that has sufficient sensitivity to resolve local defects of the target size. However, while the sensor design has been modified to provide a more representative flaw response with minimal impact from unmodeled effects, the resulting response is still a “blurred” image of the actual flaw. Hence, the MR-MWM-Array approach to CUI requires an algorithm to provide accurate sizing information for detected flaws. The following chapter develops a prototype algorithm and demonstrates its successful implementation.

5.1 Proposed Lattice Approach for Flaw Sizing

By taking the computed footprints generated in the previous chapter and convolving them with simulated defects of various sizes, we can create a multidimensional database that can be used along with JENTEK’s multivariate inverse methods, also known as grid methods, to produce flaw sizing estimates. As described in Section 1.5, JENTEK’s grid methods are typically used to convert multifrequency transimpedance measurements into absolute material properties: for each frequency measured, the real and imaginary components of the impedance response provide two equations. Given sufficient selectivity (independent equations are provided by the multifrequency impedance data), n frequencies allow for the estimation of $2n$ properties. The sensitivity and selectivity of a measurement can be analyzed using singular value decomposition of the Jacobian matrix [1].

It is necessary to find a set of observable measurement characteristics that can be used to correlate to the flaw characteristics of interest. Since flaws can come in all shapes and depth profiles, assumptions need to be made about observed flaws. If each flaw is assumed to be discrete and of uniform depth over a rectangular area, then the flaw characteristics to be measured are well defined: length, width and depth. Therefore, it is necessary to determine three observable measurement characteristics for each flaw.

Length is defined to be in the circumferential direction of the pipeline and width is defined to be in the axial direction of the pipeline. Length and width can also be characterized relative to the sensor; length is in the channel direction and width is in the scan direction.

The proposed measurement characteristics can be determined using the following procedure:

1. Apply a threshold to the thickness image to identify the location of discrete flaws.
2. Determine the location of each discrete flaw and an estimated length and width of the response that exceeds the threshold.
3. Within the area of the flaw, determine the maximum flaw response.

Using this procedure, the generated flaw sizing lattice has three inputs and three outputs. The inputs are flaw response length and width below a given threshold, and maximum flaw depth. The outputs are estimated flaw length, width and uniform depth.

5.2 Lattice Generation and Orthogonality

In order to prove the validity of this approach, it is necessary to first generate a test lattice with sufficient sensitivity and selectivity to generate reliable flaw characteristic estimates given measured observations. For the following discussion, the inputs to the lattice, dependent variables in the forward model (measured signal width, length and uniform depth), will be referred to as signal characteristics, and the outputs of the lattice, independent variables in the forward model (estimated flaw width, length and uniform depth), will be referred to as flaw characteristics.

Sensitivity measures the resulting change in flaw characteristics due to small changes in signal characteristics. Low sensitivity (i.e. very large changes in flaw characteristic due to a perturbation) can result in a very unreliable measurement. A lattice's selectivity reflects the independence of the lattice's output parameters. A low selectivity lattice results in the lattice being multivalued (a set of measurement characteristics corresponding to more than one possible set of flaw characteristics) which causes the multivariate inverse method search algorithm to fail.

The sensitivity and selectivity of the lattice can be evaluated by visualizing the three-dimensional lattice in multiple two-dimensional slices. This is shown in Figure 5.1 for a flaw sizing lattice generated with an 0.015" threshold using the footprint generated by the algorithm described in Section 4.3 for the sensor pictured in Figure 4.12. The nominal pipe diameter was 6.625" and the pipe wall was 0.280" (this is a standard 6" schedule 40 pipe size). The flaws were assumed to be internal flaws, although the lattice change is minimal when external flaws are considered.

The selectivity of the lattice can be evaluated by looking at the lines of constant flaw characteristic property and looking to see if they are close to orthogonal to the other lines of constant flaw characteristic property (for example, seeing if a line of constant flaw length and width while varying depth is orthogonal to lines of constant flaw length and depth while varying width). If the lines are close to being parallel,

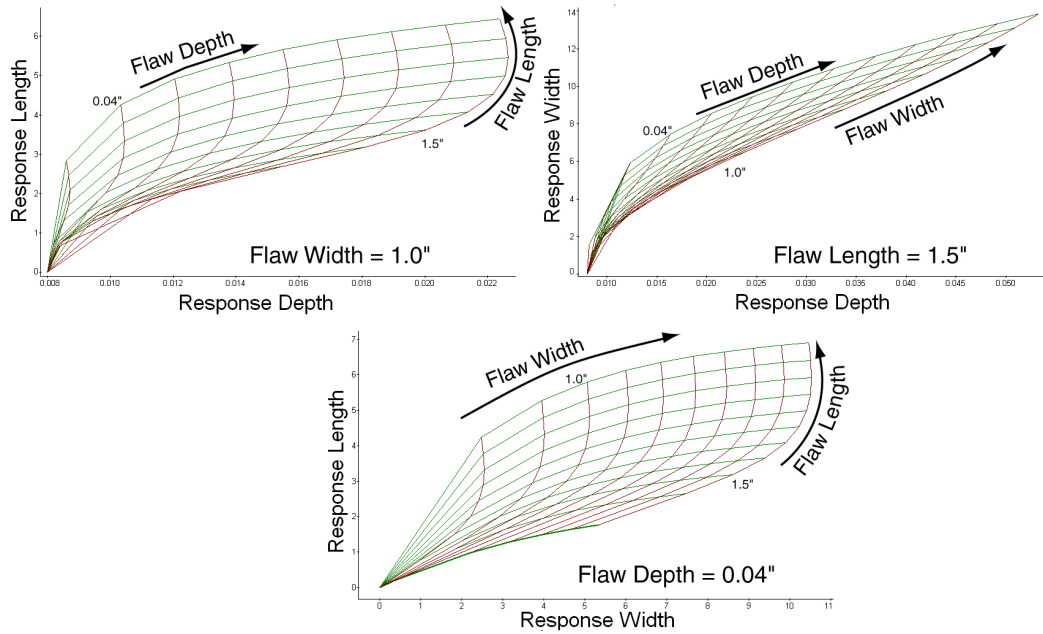


Figure 5.1: Visualization of the flaw sizing lattice for a 0.015" threshold using the footprint generated by the algorithm described in Section 4.3 for the sensor pictured in Figure 4.12. The upper left shows a lattice slice of length vs. depth for an assumed flaw width of 1.0". The upper right shows a lattice slice of width vs. depth for an assumed flaw length of 1.5". The bottom shows a lattice slice of length vs. width for an assumed flaw depth of 0.04".

then there is low selectivity and the nonlinear search algorithm will be unstable. In all three grid slices that are displayed in Figure 5.1, the selectivity above a flaw width of 1", length of 1.5" and flaw depth of 0.040" should be sufficient for successful implementation.

Sensitivity can be determined by the size of the grid cells seen in the three slices displayed in Figure 5.1. Again, the sensitivity seems acceptable above the same flaw sizes determined to be sufficient for selectivity.

Below these selectivity and sensitivity limits, it is unlikely that the flaw sizing algorithm will be reliable. However, these limits show feasibility for the algorithm to be able to size flaws that meet the application requirements. Given acceptable sensitivity and selectivity, since the lattice is not overconstrained (the number of inputs and outputs are equal), it follows that if the observed sensor response falls within the lattice, then there may be a unique solution. Furthermore, while sizing may not be reliable for flaws smaller than the limits defined in this section, detection still will be possible.

It is interesting that the selectivity and sensitivity are acceptable at a lower width threshold than length threshold. This makes sense, though, if we keep in mind that the footprint in the length direction is much bigger for this sensor than in the width direction. Therefore, in the width direction we have more sensitivity to local defects and can resolve them at smaller sizes.

Furthermore, it makes sense that there is enough independence in the length, width and depth of the flaws given the observed length, width and maximum depth of the flaw response. Based on the method of convolution, we can intuit the relationship between the input parameters of the lattice and the output parameters. As the flaw width changes, we would expect the width of the response and the depth of the response to change significantly and the length of the response to change minimally. Likewise, as the length of the flaw changes, we would expect the length of the response

and the depth of the response to change significantly while the width of the response changes minimally. And finally, if the depth of the flaw changes, we would expect all three response characteristics to change. These three relationships would appear to be independent.

While this visualization shows feasibility, the accuracy of the method is still in question. This is analyzed in the following section.

5.3 Finite Element Method (FEM) and Measurement Validation of Sizing Approach

We have validated that the models developed in Chapter 4 accurately predict a sensor-geometry's footprint. This was done by showing agreement between a flaw response's predicted and actual signature for two different sensor designs (single rectangular drive and double rectangular drive). The result of this was that we were able to use the footprint model to design a sensor-geometry that had much more sensitivity to local defects while simultaneously minimizing unmodeled effects.

While the general footprint shape is accurately predicted by the models developed in Chapter 4, using the footprint convolution method for sizing requires a more stringent validation. The width, length and depth of a sensor's response must match the result of convolving the sensor's footprint with a simulated flaw to an accuracy that allows the multivariate inverse methods to effectively use the generated lattice.

Since it is not practical (from both a cost and time perspective) to create a large number of sample flaws of varying sizes and depths, FEM simulation was used to predict the response of the sensor pictured in Figure 4.12 to an array of flaw sizes and depths in flat steel plates 0.25" thick with 2" of lift-off. These simulations used the commercial package Faraday, a three-dimensional eddy current solver from Integrated Engineering Software. The boundary element method was used with this package to

determine the magnetic field distributions since it does not require as much memory or processing time as finite element model packages. These simulations used a self-adaptive mesh with an accuracy setting 0.0003 to refine the mesh density for the computation in the areas where the fields were changing relatively rapidly and an accuracy/speed factor of 3. A smaller accuracy setting or a larger speed factor reduces the numerical error in the calculation at the expense of using more memory and a longer processing time; previous work had shown that settings that were used were reasonable for this geometry. Note that typically 2-8 GB of RAM were required for these simulations.

Because FEM simulations converge very slowly, simulating a scan over a single flaw would take nearly a month of computation time (15 minutes per measurement, 0.5 inch measurement spacing, 24 by 24 inch measurement grid, 8 flaw sizes, 10 flaw depths). A more practical use of FEM simulation for validating the footprint convolution sizing method is to simulate only the point of maximal response for each flaw. Since both the footprint model and initial measurements agree on the position for this maximal response (see Section 4.3) this is a reasonable approach. 20 Hz was the simulation frequency.

Figures 5.2 and 5.3 summarize these results. What we see is good agreement between the simulated measurements and the footprint model convolution for flaws of varying sizes and aspect ratios: there is a linear relationship between flaw depth and response maximum, and the slope is determined by the area of the flaw. However, the linearity of the FEM simulations starts to break down for the small aspect ratio flaws with large depth. This is likely due to a numerical noise issue in the FEM simulation: it was difficult to get convergence in these cases.

With demonstrated agreement between the models and the simulated measurements, and a lattice that has reasonable sensitivity and selectivity, the final verification step is to try to process actual measurements. A 4" long (circumferential), 6"

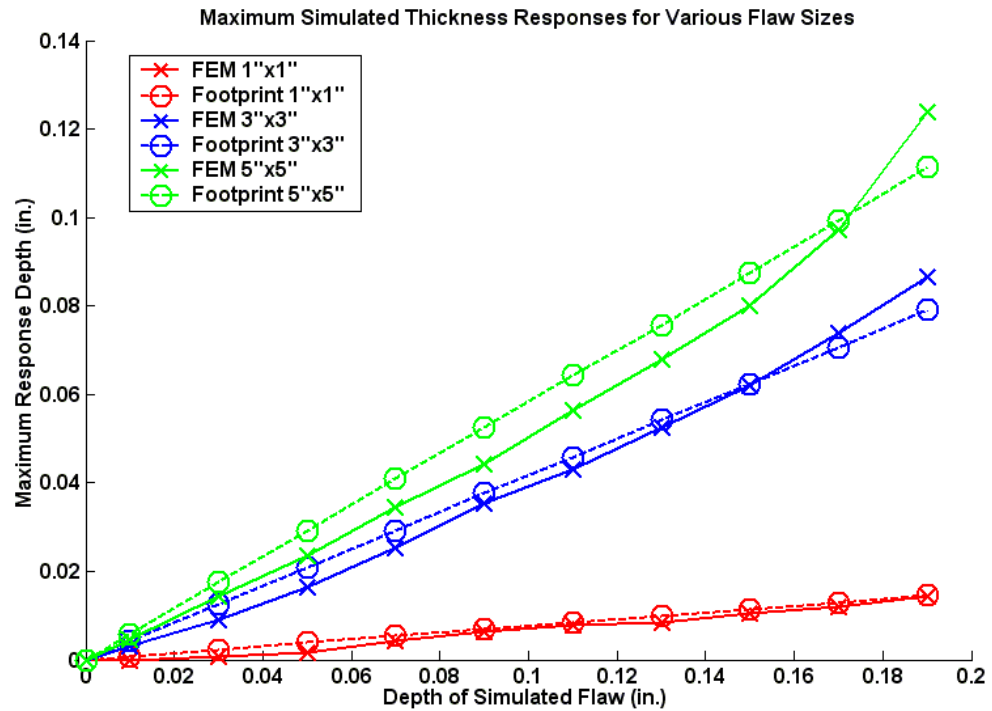


Figure 5.2: Comparison of FEM simulated maximum thickness response to footprint calculated maximum thickness response to a variety of flaw sizes and depths with equal aspect ratio. The sensor simulated is shown in Figure 4.12. The footprint model used is from Section 4.3. The flaws were simulated in 0.25" thick steel plate at 2" of liftoff.

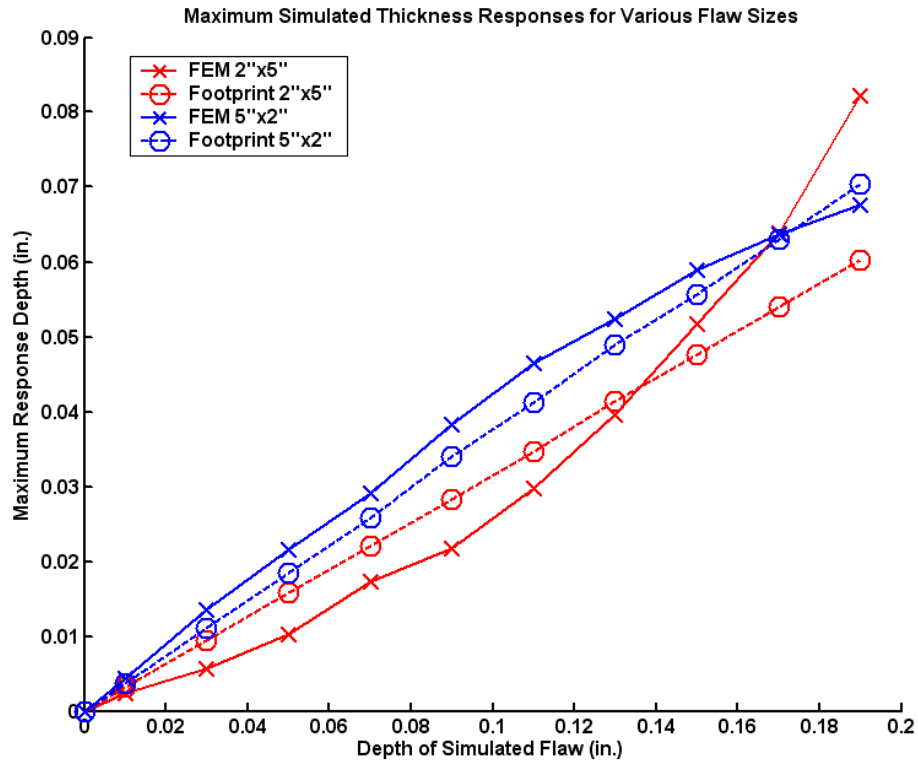


Figure 5.3: Comparison of FEM simulated maximum thickness response to footprint calculated maximum thickness response to a variety of flaw sizes and depths with large and small aspect ratios. The sensor simulated is shown in Figure 4.12. The footprint model used is from Section 4.3. The flaws were simulated in 0.25" thick steel plate at 2" of liftoff.

wide (axial), 0.100" deep flaw in a 6.625" diameter, 0.280" thick pipe was scanned with 2" of insulation and standard weatherjacketing. The flaw response, shown in Figure 5.4 (left) was thresholded with a 0.015" threshold, and the thresholded image is shown in Figure 5.4 (right). The flaw response had a measured length of 5.3", width of 5.9" and maximum depth of 0.0248". These numbers were processed through the footprint sizing lattice and the estimated flaw size was very reasonable. Perturbations were applied to the measurement responses to verify acceptable sensitivity and selectivity of the lattice. Small changes in response sizes resulted in acceptably small changes in flaw estimate size. These results are summarized in Table 5.1.

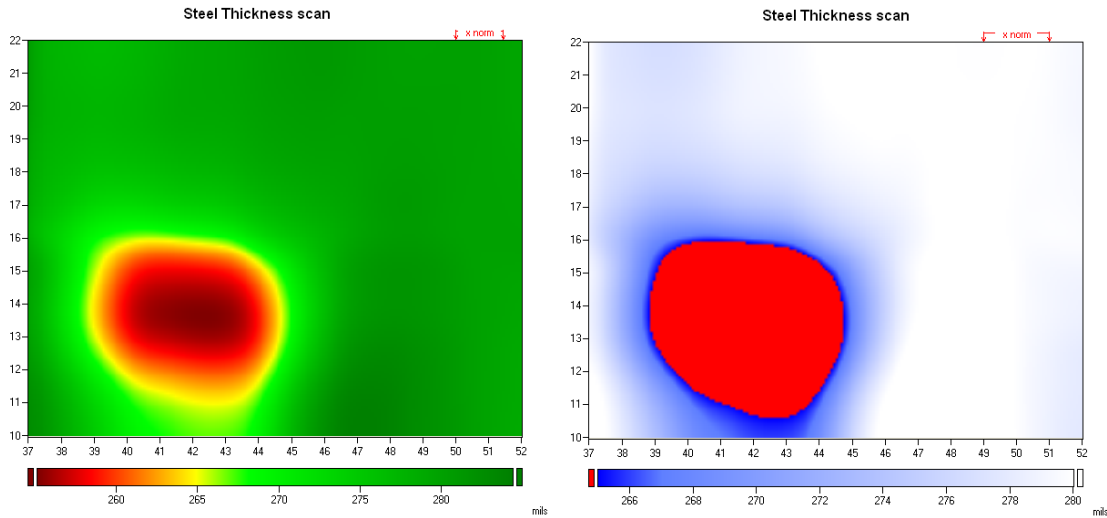


Figure 5.4: Flaw response (left) and thresholded image at a thickness drop of 0.015" (right) for a 4" long (circumferential), 6" wide (axial), 0.100" deep flaw in a 6.625" diameter, 0.280" thick pipe with 2" of insulation and standard weatherjacketing. The sensor used is pictured in Figure 4.12. In these images the circumferential direction is the y-axis and the axial direction is the x-axis.

Table 5.1: Summary of results for estimating the actual flaw size from the response pictured in Figure 5.4 by processing the response sizes through the footprint sizing lattice with a 0.015" threshold. The first line (in bold) shows good estimates for the 4" long (circumferential), 6" wide (axial), 0.100" deep flaw in a 6.625" diameter, 0.280" thick pipe. The subsequent lines show that small perturbations in the response sizes result in only small perturbations in the estimated flaw sizes. The perturbed dimensions are in bold.

Response Sizes			Estimated Flaw Sizes		
Length	Width	Depth	Length	Width	Depth
5.3"	5.9"	0.0248	4.2"	6.3"	0.095"
5.1"	5.9"	0.0248"	4.0"	6.3"	0.092"
5.5"	5.9"	0.0248"	4.4"	6.4"	0.099"
5.3"	5.7"	0.0248"	4.1"	6.2"	0.093"
5.3"	6.1"	0.0248"	4.2"	6.6"	0.096"
5.3"	5.9"	0.022"	4.0"	6.2"	0.088"
5.3"	5.9"	0.028"	4.4"	6.5"	0.105"

CHAPTER 6

SUMMARY, CONCLUSIONS AND SUGGESTED FUTURE WORK

6.1 Summary and Conclusions

The results presented in this dissertation demonstrate an MWM-Array-based corrosion-under-insulation (CUI) detection tool that satisfies the current industry requirement for an exterior pipe inspection instrument that does not require removal or replacement of a pipe's insulation and weatherjacket. Based on discussions with industry participants, the sensor is required to be capable of imaging through at least 0.5" of steel that is covered in 2" of insulation and a weatherjacket. A 0.05" deep flaw over a 2" diameter is the target detection threshold. Consistent with other MWM implementations, complicated calibration procedures must be avoided: only an air calibration should be required. Finally, the inspection must be performed scanning at 1-2" per second and must provide general pipeline wall thickness estimates accurate to within 0.005" away from local deviations.

These results have been presented at a number of venues over the past three years [54]-[59]. They have also been the basis for two patent applications to date [2],[6], with more anticipated in the near future.

The results obtained during this dissertation research produced a magnetoresistive sense element-based MWM sensor with the SNR required to rapidly image a steel thickness of at least 0.5" through thick coatings. The design was developed after theoretically evaluating multiple alternative sense element types, including inductive and other active elements. The sensor electronics needed to operate the MR element

were then designed and implemented. And, a sensor with the necessary SNR was experimentally demonstrated.

Furthermore, this work has extended the surface reluctance-based transfer function model used to model the MWM in the presence of a layered MUT into cylindrical coordinates. The case where the drive conductors are aligned circumferentially and the case where the drive conductors are aligned axially were both considered. The extended models were implemented and then validated, demonstrating the needed improvement in agreement between the model and measurements taken with magnetoresistive sensors wrapped around cylindrical specimens.

Next the sensor's interaction with local material deviations was examined. Specifically, the models developed thus far for magnetoquasistatic-field sensors assume uniformly layered media. Since this assumption breaks down in the presence of local defects such as corrosion pitting and weatherjacket overlaps, with resulting impact on measurement accuracy, it was necessary to develop a perturbation model, also referred to as a footprint model, to describe the MWM's interaction with local material deviations. Once demonstrated to be predictive of a sensor-geometry's behavior in the presence of local perturbations, the footprint model was used to intelligently design a drive construct that is more sensitive to local deviations in pipeline steel thickness, while simultaneously less sensitive to unmodeled effects such as the weatherjacket overlap region. This improvement allowed the MR-MWM-Array system to successfully demonstrate the required flaw detection capability.

Finally, given the required sensitivity, a defect sizing algorithm was required. So, as a last step in this dissertation research, the local perturbation model was used to design a flaw sizing algorithm. This was done by taking the computed footprint and convolving it with uniform flaws of various depths, lengths and widths to generate a three-dimensional lattice that could be used with JENTEK's multivariate inverse methods. With a given response's characteristic length, width and depth, the inverse

methods are able to successfully estimate the original flaw's length, width and depth.

This research culminates in the demonstration of a CUI inspection tool capable of imaging local defects to the required accuracy. Figure 6.1 shows the complete CUI system including sensor, scanner and instrumentation electronics in the field during performance trials. Figure 6.2 shows the result of a scan on a pipe with real corrosion. The flaw imaged was approximately 2" in diameter and 0.080" deep on a 20" diameter, 0.25" thick pipe, covered with 2" of insulation and weatherjacket. Even though the detected flaw is slightly deeper than the target detectable flaw, the achieved SNR clearly demonstrates the required sensitivity. After thresholding with a 0.010" threshold and processing the response dimensions through the flaw sizing lattice (2.8" long, 1.8" wide, 0.013" deep), the flaw was accurately sized to be 2.1" long, 1.9" wide and 0.075" deep.

6.2 Suggested Future Work

The research presented in this dissertation developed the MR-MWM-Array, the associated instrumentation electronics, and the electromagnetic models needed to solve the target CUI application. These developments open up many new potential areas of research, both improving on the CUI methodology and applying these advancements to new applications. The following sections provide an overview of three possible directions for future research.

6.2.1 Generalization of the Cylindrical Coordinate Models

The cylindrical models developed in this research make two large assumptions that can be relaxed in future research. First, in both of the models developed in Chapter 3, the orientation of the drive conductors with respect to the coordinate system was fixed: in the first model, the drive was oriented circumferentially, and



Figure 6.1: Full CUI system including MR-MWM-Array sensor, scanner and instrumentation electronics in the field during performance trials.

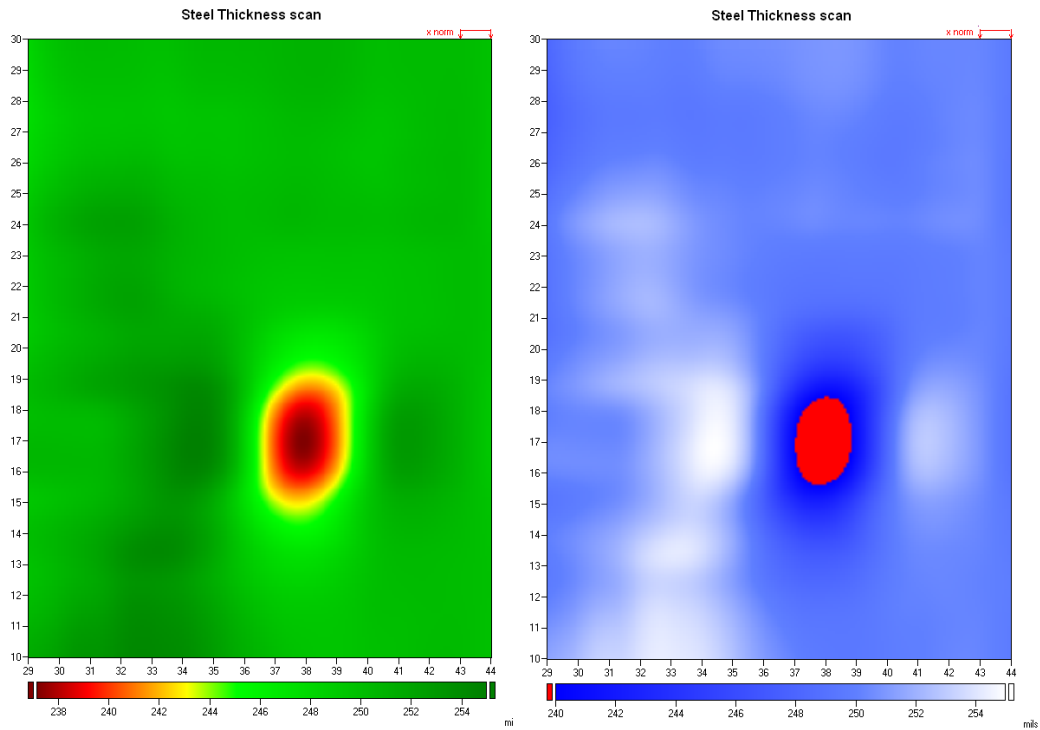


Figure 6.2: Result of a scan on a pipe with real corrosion. The flaw imaged was approximately 2" in diameter and 0.080" deep on a 20" diameter, 0.25" thick pipe, covered with 2" of insulation and weatherjacket. The basic sensor response is shown on the left and the thresholded image is shown on the right. Even though the detected flaw is slightly deeper than the target sensitivity level, the achieved SNR clearly demonstrates the required sensitivity.

in the second model, the drive was oriented axially. There are many applications in which it would be desirable to place the drive conductors at a specified angle between axial and circumferential - i.e, the drive would wrap around the pipe in a helical manner. This is definitely appropriate when trying to simultaneously detect cracks that may be propagating circumferentially and axially - scanning at 45° to the cracks' propagation would be necessary [20]-[24]. This freedom of drive orientation adds another layer of complexity to the mathematical derivation but should still present a tractable derivation.

Furthermore, as stated in the introduction to Chapter 3, the modeling of the MWM is simplified when the current density in each drive winding is assumed to be uniformly distributed. This assumption is valid for the CUI application because the dimension of each individual conductor is much smaller than the other important characteristic dimensions: the distance between the drive conductors and secondary conductors, the imposed spatial wavelength, and the distance between the conductors and the MUT. For other applications it will be necessary to relax this assumption. This can be achieved by using a collocation method as has been formulated in the Cartesian coordinate case [37].

6.2.2 Investigation into other Magnetoresistive Sensor Constructs

The development of the MR-MWM-Array created an MWM sensor construct sensitive to the thickness of steel. While the double-row, double rectangular sensor pictured in Figure 4.12 provided the necessary sensitivity to detect a 2" diameter, 0.05" deep flaw with a comfortable SNR, there may be sensor constructs that allow for greater sensitivity to local defects.

The main advantage of the periodic MWM sensor is the accuracy with which it can be modeled. When combined with the sensor electronics that allow for low-noise, low-frequency measurements, this provides a powerful tool for measuring absolute

steel thickness. However, there are potential applications where detecting very small, very local thickness variations may be more important than accurately measuring the absolute thickness. This can be the case where pitting is one of the main mechanisms for corrosion initiation.

For these applications it may be appropriate to take the magnetoresistive sense elements and place them in a drive construct that deviates from the MWM model, trading off modelability for increased local sensitivity. This may involve looking at different components of the magnetic field (this research focused mainly on the component of the magnetic field in the $\hat{\rho}$ direction), considering differential sensing modes where calibration in air is not possible, and studying the use of ferromagnetic yokes / sensor backing materials in order to shape the generated magnetic field. While some of these approaches have been investigated by competing sensing technologies, combining them with the extremely low-noise MR sensing technology developed in this research would be novel.

6.2.3 Improved Flaw Sizing Estimates

The sizing algorithm developed in Chapter 5 of this dissertation assumes that any detected defect is uniform in depth over a rectangular area. While this is an effective assumption under many measurement conditions and has provided a useful first order flaw depth estimation tool, an interesting research problem would be to develop an algorithm that relaxes this assumption in order to provide a more robust flaw sizing tool.

REFERENCES

- [1] N. J. Goldfine, "Magnetometers for Improved Materials Characterization in Aerospace Applications," *Materials Evaluation*, vol. 51, no. 3, pp. 396, March 1993.
- [2] N. J. Goldfine, S. Denenberg, T. Dunford, Y. Sheiretov, A. Washabaugh, S. Haque, L. Kristal, "Multiple Unknown Inspection With and Without Coatings/Insulation," Patent Provisional Docket Number 1884.2081-000, February 17, 2012.
- [3] C. P. Dillon, "Corrosion Control in Chemical Process Industries," Nickel Development Institute, MacGraw Hill, 1986.
- [4] Baker, M., "Pipeline Corrosion Final Report," U.S. Department of Transportation Pipeline and Hazardous Materials Safety Administration. November 2008.
- [5] "The State of the National Pipeline Infrastructure - A Preliminary Report," submitted by Interstate Natural Gas Association of America.
- [6] T. Dunford, S. Denenberg, N. J. Goldfine, Y. Sheiretov, "Inspection for Corrosion and Other Defects Through Insulation," Patent Provisional Docket Number 1884.2080-000, October 25, 2011.
- [7] F. Hardie, "Evaluation of the effectiveness of non-destructive testing screening methods for in-service inspection," Doosan Babcock Energy Limited, Health and Safety Executive 2009.
- [8] Incotest Specifications, <http://www.karkia-ind.com/INCOTEST.htm>, Karkia Industries, 2008.
- [9] S. Birth and F. Baker, "Long-Range Guided-Wave Ultrasonics: A New Age in Pipeline Inspection," American Welding Society, Fall 2007.
- [10] Wavemaker G3 Third Generation Pipe Screening System Specifications, http://www.silverwingme.com/guided_wave/guided_wave_wavemaker_G.html, Silverwing Middle East LLC, 2013.
- [11] Teletest Specifications, <http://www.teletestfocus.com/teletest-focus-plus/index.jsp>, Plant Integrity Limited, 2011.

- [12] The SCAR System Specification, <http://www.oceaneering.com/oceandocuments/brochures/inspection/INS%20-%20The%20SCAR%20System.pdf>, Oceaneering International, Inc., 2012.
- [13] V. K. Goyal, K. Gupta, N. Gupta, "On-line Real-Time Digital Radiography of Piping System," Omega International Technology, Inc., 1996.
- [14] J. R. Melcher, "Apparatus and Methods for Measuring Permeability and Conductivity in Materials Using Multiple Wavelength Interrogations," US patent number 5,015,951, May 14, 1991.
- [15] N. J. Goldfine, J. R. Melcher, "Magnetometer Having Periodic Winding Structure and Material Property Estimator," US patent number 5,453,689, September 26, 1995.
- [16] N. J. Goldfine, D. Clark, H. Eckhardt, "Apparatus and Methods for Measuring Bulk Materials and Surface Condition for Flat and Curved Parts," US patent pending, ser. no. 60/002,804.
- [17] N. J. Goldfine, D. Clark, T. Lovett, "Materials Characterization Using Model-based MWET," EPRI Topical Workshop: Electromagnetic NDE Applications in the Electric Power Industry, Charlotte, NC, 1995.
- [18] N. J. Goldfine, D. E. Schlicker, W. M. Chepolis, "Robust, Absolute Property Measurements for Aerospace System Health Monitoring and Manufacturing Quality Control," Proceedings of BiNDT Conference NDT 98, September 1998.
- [19] J. M. Fisher, N. J. Goldfine, V. Zilberstein, "Cold Work Quality Assessment and Fatigue Characterization Using Conformable MWMTM Eddy-Current Sensors," 49th Defense Working Group on NDT, Biloxi, Mississippi, November 2000.
- [20] V. Zilberstein, D. E. Schlicker, K. Walrath, V. Weiss, N. J. Goldfine, "MWMTM Eddy Current Sensors for Monitoring of Crack Initiation and Growth during Fatigue Tests and in Service," International Conference of Fatigue Damage in Structural Materials III, Hyannis, MA, September 2000.
- [21] V. Weiss, N. J. Goldfine, M. Natishan, "Early Stage Fatigue Damage Characterization in Aluminum Alloys and Stainless Steels with Meandering Winding Magnetometer Technology," ASTM 30th National Symposium on Fatigue and Fracture Mechanics at Washington University, St. Louis, MO, June 1998.
- [22] N. J. Goldfine, D. E. Schlicker, A. Washabaugh, "Surface-Mounted Eddy-Current Sensors for On-Line Monitoring of Fatigue Tests and for Aircraft Health Monitoring," Second Joint NASA/FAA/DoD Conference on Aging Aircraft, August 1998.
- [23] N. J. Goldfine, "Conformable Meandering Winding Magnetometer (MWM) for Flaw and Materials Characterization in Ferrous and Nonferrous Metals,"

- NDE Performance Demonstration, Planning and Research, American Society of Mechanical Engineers, Pressure Vessels and Piping Division, PVP, vol. 352 1997. ASM. New York, NY, 1997.
- [24] N. J. Goldfine, A. Washabaugh, V. Zilberstein, D. E. Schlicker, M. Fisher, T. Lovett, T. Yentzer, R. Pittman, "Scanning and Permanently Mounted Conformable MWM Eddy Current Arrays for Fatigue/Corrosion Imaging and Fatigue Monitoring," USAF ASIP CConference, San Antonio, TX, December 2000.
- [25] T. Yentzer, V. Zilberstein, N. Goldfine, D. Schlicker, D. Clark, "Anisotropic Conductivity Measurements for Quality Control of C-130/P-3 Propeller Blades Using MWMTM Sensors with Grid Methods," Fourth DoD/FAA/NASA Conference on Aging Aircraft, St. Louis, MO, May 2000.
- [26] N. J. Goldfine, Y. Sheiretov, A. Washabaugh, V. Zilberstein, "Materials Characterization and Flaw Detection for Metallic Coating Repairs," *Insight: Non-Destructive Testing and Condition Monitoring*, vol. 42, no. 12, December 2000.
- [27] N. J. Goldfine, D. E. Schlicker, Y. Sheiretov, A. Washabaugh, V. Zilberstein, "Conformable Eddy-Current Sensors and Arrays for Fleet-Wide Gas Turbine Component Quality Assessment," ASME Turbo Expo Land, Sea, and Air, New Orleans, LA, 2001.
- [28] V. Zilberstein, Y. Sheiretov, A. Washabaugh, Y. Chen, N. J. Goldfine, "Applications of Spatially Periodic Field Eddy Current Sensors for Surface Layer Characterization in Metallic Alloys," 27th Annual Review of Progress in QNDE, Iowa State University, Ames, Iowa, July 2000.
- [29] N. J. Goldfine, T. Lovett, Y. Sheiretov, P. J. Zombo, "Dielectrometers and Magnetometers, Suitable for In-situ Inspection of Ceramic and Metallic Coated Components," SPIE proceedings, vol. 2459, pp. 164174, 1995.
- [30] N. J. Goldfine, V. Zilberstein, "Recent Applications of Meandering Winding Magnetometers to Materials Characterization," *Insight: Non-Destructive Testing and Condition Monitoring*, vol. 42, no. 1, 2000.
- [31] N. J. Goldfine, J. T. Lovett, Y. J. Zhao, "A New Eddy-Current Based Technology for Repeatable Residual Stress and Age Degradation Monitoring," ASNT International Chemical and Petroleum Industry Inspection Technology, IV Topical Conference, Houston, TX, June 1995.
- [32] D. E. Schlicker, H. J. Goldfine, A. P. Washabaugh, K. E. Walrath, I. C. Shay, D. C. Grundy, M. Windoloski, "Test Circuit Having Parallel Drive Segments and a Plurality of Sense Elements," US Patent Number 7,049,811, May 23, 2006.
- [33] D. E. Schlicker, N. J. Goldfine, W. P. Washabaugh, K. W. Walrath, I. C. Shay, D. C. Grundy, M. Windoloski, "Eddy Current Sensor Arrays Having Drive Windings with Extended Portions," U.S. Patent Number 6,784,662, August 31, 2004.

- [34] Y. Sheiretov, N. J. Goldfine, Ap. P. Washabaugh, D. E. Schlicker, "Material Property Estimation Using Inverse Interpolation," U.S. Patent Number 8,050,883, November 1, 2011.
- [35] N. J. Goldfine, Y. Sheiretov, D. E. Schlicker, A. P. Washabaugh, "Rapid, Nonlinear System Identification for NDT, Using Sensor Response Databases," *Materials Evaluation*, vol. 66, no. 7, July 2008.
- [36] N. J. Goldfine, "Uncalibrated, Absolute Property Estimation and Measurement Optimization for Conducting and Magnetic Media Using Imposed ω -k Magnetometry," Doctoral Thesis, Cataloged into the Massachusetts Institute of Technology Libraries, October 1992.
- [37] Y. Sheiretov, "Deep Penetration Magnetoquasistatic Sensors," Doctoral Thesis, Cataloged into the Massachusetts Institute of Technology Libraries, June 2001.
- [38] D. Schlicker, "Imaging of Absolute Electrical Properties Using Electroquasistatic and Magnetoquasistatic Sensor Arrays," Doctoral Thesis, Cataloged into the Massachusetts Institute of Technology Libraries, October 2005.
- [39] LT1028/LT1128 datasheet, Ultralow Noise Precision High Speed Op Amps, Linear Technology Corporation, 1992.
- [40] Ribbon Cable Current Rating, <http://www.mosaic-industries.com/embedded-systems/electronic-instrument-design-new-product-development/cables/ribbon-cable-current-rating>, Mosaic Industries, Inc.
- [41] "Free BH Curves," MagWeb: Your Source for Magnetic Material Data, <http://magweb.us/free-bh-curves/>, Low Carbon Steel - SAE1020.
- [42] J. Lenz, "A Review of Magnetic Sensors," *Proceedings of the IEEE*, vol. 78, no. 6, June 1990.
- [43] N. Ramasamy and M. Janawadkar, "SQUID Based Nondestructive Evaluation," Chapter 2: Nondestructive Testing Methods and New Applications, Intech Europe, March 2012.
- [44] D. J. Staton, Y. P. Ma, N. G. Sepulveda, J. P. Wikswo Jr., "High-resolution magnetic mapping using a squid magnetometer array," *IEEE Transactions on Magnetics*, vol. 27, no. 2, March 1991.
- [45] R. J. P. Bain, G. B. Donaldson, S. Evanson, and G. Hayward, "SQUID gradiometric detection of defects in ferromagnetic structures," In *SQUID 85 - Superconducting Quantum Interference Devices and their Applications*, (eds.), pp. 841-846, ISBN 0899251447, Walter de Gruyter and Co., Berlin, New York, 1985.

- [46] S. S. Tinchev, J. H. Hinken, M. Stiller, A. Baranyak, D. Hartmann, "High-TC RF SQUID magnetometer system for high-resolution magnetic imaging," IEEE Transactions on Applied Superconductivity, vol. 3, no. 1, pt. 4, March 1993, pp. 246971.
- [47] R. Hood, L. M. Falicov, "Theory of the negative magnetoresistance in magnetic metallic multilayers," Materials Research Society Symposium Proceedings, vol. 313, San Francisco, California, April 1216, 1993.
- [48] AA and AB-Series Analog Sensors datasheet, Giant Magnetoresistive Sensors, NVE Corporation, 2007.
- [49] HMC1001/HMC1002/HMC1021/HMC1022 datasheet, 1- and 2-Axis Magnetic Sensors, Honeywell International, Inc., 2008.
- [50] H. Haus, J. Melcher, Electromagnetic Fields and Energy, Prentice-Hall Inc., New Jersey, 1989.
- [51] F. Bowman, Introduction to Bessel Functions, Courier Dover Publications, 1958.
- [52] F. Olver, L. Maximon, "Chapter 10: Bessel Functions," Digital Library of Mathematical Functions, <http://dlmf.nist.gov/10>, June 2013.
- [53] S. R. Rengarajan and Y. Rahmat-Samii, "The Field Equivalence Principle: Illustration of the Establishment of the Non-Intuitive Null fields," IEEE Antennas and Propagation Magazine, Vol. 43, No. 4, August 2000.
- [54] T. Dunford, N. J. Goldfine, S. Denenberg, A. P. Washabaugh, Y. Sheiretov, D. Straney, "MWM-Array In-Line Inspection Technology Status," 2014 Chevron NDE and Pipeline Forum Houston, TX, March 25 - 27, 2014.
- [55] S. F. Farea, R. G. Hammad, F. O. Dawoud, S. A. Dossary, S. Alzahrani, A. S. Binqorsain, and A. Minachi, [Saudi Aramco], N. J. Goldfine, S. Denenberg, B. Manning, J. Kott, T. Dunford, S. Haque, C. Martin, A. P. Washabaugh, Y. Sheiretov, [JENTEK Sensors, Inc.] and R. Al-Rushaid and F. Haught [Al-Rushaid Technologies], "Field Demonstrations of MR-MWM-Array Solution for Detection, Imaging and Sizing of Corrosion under Fireproofing (CUF) with Wire Mesh," 15th Middle East Corrosion Conference, Bahrain, Feb. 2-5, 2014.
- [56] S. Denenberg, D. Straney, T. Dunford, Y. Sheiretov, S. Haque, B. Manning, J. Kott, A. P. Washabaugh, N. J. Goldfine, "Advancements in Imaging Corrosion Under Insulation (CUI) for Piping and Vessels," ASNT Annual Conference, Las Vegas, Nevada, 4-7 November 2013.
- [57] N. J. Goldfine, S. Denenberg, Y. Sheiretov, S. Chaplan, D. Straney, M. Windoloski, Z. Thomas, "High Throughput Engine Component Inspection Using Massively Parallel Solutions," ASNT Annual Conference, Las Vegas, Nevada, 4-7 November 2013.

- [58] N. J. Goldfine, T. Dunford, S. Denenberg, Y. Sheiretov, A. Washabaugh, S. Haque, "Inspection of Refinery Piping and Vessels from the Outside for External and Internal Corrosion," API Beijing China, 9-13 September 2013.
- [59] N. J. Goldfine, A. Washabaugh, T. Dunford, S. Denenberg, S. Haque, "Rapid Corrosion Imaging through Insulation and Weather Protection with MWM-Arrays," Chevron Pipeline and NDE Forum, Houston, Texas, March 5-9, 2012.